UNIVERSITY OF CALIFORNIA

Los Angeles

Novel Thin Film Solar Cells: Film Formation/Properties and Device Physics

A dissertation submitted in partial satisfaction of the

requirements for the degree Doctor of Philosophy

in Materials Science and Engineering

by

Tze-Bin Song

2015

ABSTRACT OF THE DISSERTATION

Novel Thin Film Solar Cells: Film Formation/Properties and Device Physics

by

Tze-Bin Song

Doctor of Philosophy in Materials Science and Engineering

University of California, Los Angeles, 2015

Professor Yang Yang, Chair

Thin film solar cells have attracted considerable attentions due to their lightweight, low material consumption, ease of fabrication, and potentially high power-conversion efficiency. However, significant cost reductions as well as large-scale production are necessary to compete with the conventional utility power. To reduce cost, vacuum-free manufacture process for each solar cell component is needed. This dissertation focus on novel and cost-effective methods on solution processes of thin film solar cells, ranged from top transparent electrode, the various absorbing layers, and eventually achieving high performance devices. For the transparent electrode, our focus is on the silver nano-wires, and the nano-junction within the network. For the absorbing layer, our targets are: $Cu_2ZnSn(S,Se)_4$ (CZTS), and $CH_3NH_3PbX_3$ (MAX, X= I, Cl, Br) perovskite materials,

respectively. In **Chapter 2**, a formation of Ag-NW contacts was proven to be an efficient method to reduce the contact resistance using the Joule heating, current crowding, and electromigration effect. Transparent electrodes have been applied to optoelectronic devices. **Chapter 3**, a metal nanowire composite layer was demonstrated to achieve fully solution-processed as a component of $CuIn(S,Se)_4$ (CISS) solar cells. The high performance of the nanowire composite and the role of such electrodes in high performance solar devices were elucidated. Further improvement of the nanowire network to achieve better stability was also demonstrated. **Chapter 4** presented a doping control method to investigate the effect of sodium dopant to the CZTS solar cells in terms of device performance, properties, and film formation. A novel synthesis method of CZTS:Na nanocrystal was demonstrated. Sodium incorporation method successfully improved the efficiency by around 50%. In addition, the role of sodium incorporation was investigated. In **Chapter 5**, the transformation of solution-processed MAX_3 perovskite solar cells was investigated and possible reaction pathways were proposed. Secondary phases from this process were identified and the corresponding physical properties during the transformation were further studied.

The dissertation of Tze-Bin Song is approved.

Bruce S. Dunn

Chi On Chui

Yang Yang, Committee Chair

University of California, Los Angeles

2015

This dissertation is dedicated to my family.

Table of Contents

List of Tables

ACKNOWLEDGMENTS

First of all, I would like to give my most sincere thanks to my advisor Prof. Yang Yang. His great perspective and guidance always inspires me to pursue higher expectations for myself. He educated me not only in the area of materials science and physics, but also on valuable lessons on how to be a great scientist. I also thank him for his trust and for giving me a lot of opportunities to work on various fields. I have had a great and fruitful journey in these five years with his guidance. I am also very grateful for having an extraordinary doctoral committee and wish to thank Professor Bruce S. Dunn, Professor Paul S. Weiss, Professor Harold R. Fetterman, and Professor Chi On Chui for their valuable discussions and suggestions during my studies at UCLA. Furthermore, I appreciated Professor King-Ning Tu and Professor Yu Huang for valuable discussions and help during collaborations. I learned a lot from them during our work in extending the thin film diffusion mechanism into nanomaterials.

I am very grateful to all the graduate students, post-docs, and research fellows that I have had the pleasure to work with: Dr. Choong-Heui Chung and Dr. Zhu Rui for their guidance on the transparent electrode project and in developing a high-performance composite in my first year in the group; Dr. Brion Bob for his help and collaboration when working on the TEL project together and further development of nanowire inks; Yao-Tsung Hsieh,

Chia-Jun Hsu, Shenglin Ye, Dr. Wenbing Yang, Dr. Wan-Ching Hsu, Dr. Hsin-Sheng Duan, and Dr. Chengyang Jiang for all the collaboration and efforts in making significant progress on the CZTS project; Luo Song for the collaboration on CZTS and perovskite solar cells; Dr. You Seung Rim and Huajun Chen for help with transistor fabrication, processing and analyses; Dr. Jingbi You, Dr. Yongsheng Liu, Dr. Qi Chen, Yihao Fang, Hsin-Hua Wang, Yang (Micheal) Yang, Lei Meng, Zack St Louis, and Nicholas De Marco for collaboration on the perovskite solar cells project; Dr. Huanping Zhou for all the collaboration on CISS, CZTS, perovskite solar cells projects; Chun-Chiang Kuo for teaching me graphene growth and processing; Dr. Zheng Xu for teaching me XPS/UPS characterization; Dr. Gang Li, Dr. Ziruo, Dr. Eric Richard, Dr. Kitty Cha, Dr. Youjun He, Dr. Shirong Lu, Dr. Cai Min, Dr. Jing Gao, Dr. Letian Dou, Chun-Chao Chen, Wei-Hsuan Chang, Hongxiang Zhao, Eric Young, Steve Hawks, Penyu Sun, Sanghoon Bae, Shiqi Dong, Ariella Machness, and Sheng-Yung Chang for all the exciting and stimulating discussions. Additionally, Dr. Jeehwan Kim, Dr. Ning Li, and Dr. Devendra K. Sadana for guidance during my internship in IBM T. J. Watson Center.

Finally, I would like to thank my beloved family, especially my parents and my brother for their great support.

VITA

2007 B.S. Materials Science and Engineering, National Tsing Hua University, Taiwan

2010 M.S. Materials Science and Engineering, University of Florida, FL, USA

2010-2015 Graduate Student Researcher, Materials Science and Engineering, University of California, Los Angeles, CA, USA

PUBLICAITIONS

1. T.-B. Song, Y. S. Rim, F. Liu, B. Bob, S. Ye, Y. Yang "Robust Silver Nanowire Network for Transparent Electrode" Submitted

2. T.-B. Song, Q. Chen, H. Zhou, C. Jiang, H.-H. Wang, Y. Yang, Y. Liu, J. You, Y. Yang "Perovskite Solar Cells: Film Formation and Properties" J. Mater. Chem. A, Under Revision (2015)

3. J. Kim, Z. Hong, G. Li, T.-B. Song, J. Chey, Y. S. Lee, J. You, C.-C. Chen, D. Sadana, Y. Yang "10.5% Polymer/Amorphous Silicon Tandem Photovoltaic Cell" Nat. Com., Accepted (2015)

4. T.-B. Song, Q. Chen, H. Zhou, S. Luo, Y. Yang, J. You, Y. Yang "Unraveling Film Transformations and Device Performance of Planar Perovskite Solar Cells" Nano Energy DOI:10.1016/j.nanoen.2015.01.025 (2015)

5. J. You, Y. Yang, Z. Hong, T.-B. Song, L. Meng, Y. Liu, C. Jiang, H. Zhou, W.-H. Chang, G. Li, Y. Yang “Moisture Assisted Perovskite Film Growth for High Performance Solar Cells” Appl. Phys. Lett. 105 (18), 183902 (2014)

6. W.-C. Hsu, H. Zhou, S. Luo, T.-B. Song, Y.-T. Hsieh, H.-S. Duan, S. Ye, W. Yang, C.-J. Hsu, C. Jiang, B. Bob, Y. Yang “Spatial Element Distribution Control in Fully Solution-

Processed Nanocrystals Based 8.6% $Cu_2ZnSn(S, Se)_4$ Device" ACS Nano 8 (9), 9164-9172 (2014)

7. H. Zhou, Q. Chen, G. Li, S. Luo, T.-B. Song, H.-S. Duan, Z. Hong, J. You, Y. Liu, Y. Yang "Interface Engineering of Highly Efficient Perovskite Solar Cells" Science 345 (6196), 542-546 (2014)

8. Q. Chen, H. Zhou, T.-B. Song, S. Luo, Z. Hong, H.-S. Duan, L. Dou, Y. Liu, Y. Yang "Controllable Self-induced Passivation of Hybrid Lead Iodide Perovskites Toward High Performance Solar Cells" Nano Lett. 14 (7), 4158-4163 (2014)

9. T.-B. Song, Y. Chen, C.-H. Chung, Y. Yang, B. Bob, H.-S. Duan, G. Li, K.-N. Tu, Y. Huang, Y. Yang "Nanoscale Joule Heating and Electromigration Enhanced Ripening of Silver Nanowire Contacts" ACS Nano 8 (3), 2804-2811(2014)

10. B. Bob, T.-B. Song, C.-C. Chen, Z. Xu, Y. Yang "Nanoscale Dispersions of Gelled SnO_2: Material Properties and Device Applications" Chem. Mater. 25 (23), 4725-4730 (2013)

11. H. Zhou*, T.-B. Song*, W.-C. Hsu, S. Luo, S. Ye, H.-S. Duan, C.-J. Hsu, W. Yang, Y. Yang "Rational Defect Passivation of $Cu_2ZnSn(S,Se)_4$ Photovoltaics with Solution-Processed Cu_2ZnSnS_4:Na Nanocrystals" (*These authors contributed equally) J. Am. Chem. Soc. 135 (43), 15998-16001 (2013)

12. C.-H. Chung, T.-B. Song, B. Bob, R. Zhu, Y. Yang "Solution-Processed Flexible Transparent Conductors Composed of Silver Nanowire Networks Embedded in Indium Tin Oxide Nanoparticle Matrices" Nano Research 5 (11), 805-814 (2012)

13. H. Zhou, T.-B. Song, C.-H. Chung, B. Lei, B. Bob, R. Zhu, H.-S. Duan, C.-J. Hsu, Y. Yang "Solution-Processed TiO_2 Nanoparticles as the Window Layer for $CuIn(S,Se)_2$ Devices" Adv. Energy Mater. 2 (11), 1368-1374 (2012)

14. C.-H. Chung, T.-B. Song, B. Bob, R. Zhu, H.-S. Duan, Y. Yang "Silver Nanowire Composite Window Layers for Fully Solution-Deposited Thin-Film Photovoltaic Devices" Adv. Mater. 24 (40), 5499-5504 (2012)

Chapter 1 Introduction

Currently, world energy consumption relies mainly on fossil fuels. The limited resource of fossil fuels on Earth makes them challenging as a long-term energy source. Moreover, consuming fossil fuels produces a significant amount of carbon dioxide, which could accelerate the greenhouse effect and induce climate change worldwide. How to divert our economy from one based on fossil fuels as the dominant energy resource is an urgent issue. Among the various types of renewable energy sources, solar energy is one of the most promising candidates owing to its ubiquitous availability. The Sun provides Earth with as much energy every hour as human civilization uses every year. Therefore, photovoltaic (PV) technologies that directly convert sunlight energy to electricity is one of the most promising long-term clean energy solutions.

The most mature and well adopted PV cell is based on crystalline silicon technology, which occupied approximately 85% of the PV market in 2010.[1] However, this technology is still more expensive than energy production from fossil fuels due to the costly silicon wafers and high-temperature processes. Therefore, thin film PV devices, incorporating a wide range of materials from polymer heterojunction, halide perovskite, chalcogenides, amorphous silicon and cadmium telluride, have been extensively researched to reduce the

production costs to below that of traditional energy sources. Additionally, the thin absorber layers enable the fabrication of lightweight, flexible solar modules. To achieve such cost-effective solar cells, it will be necessary to develop new material systems and processing approaches continuously.

The introduction starts with general solar cell structures and working mechanisms (Sec. 1.1). Then, current and emerging technologies for transparent electrodes for optoelectronics are reviewed. A brief introduction and key challenges are described (Sec 1.2). This is followed by discussions on the two major solar absorber materials' properties (Sec. 1.3). The understanding and development of transparent electrodes, improving and understanding the absorber materials are the main focuses of this thesis; thus, general concepts and challenges of these directions are also discussed in this chapter.

1.1 Basic Principles of Photovoltaic Systems

Two types of solar cell structures are currently well adopted in different material systems. The first type of structure consists of back electrode/p-type/n-type/top electrode as shown in Figure 1.1a. This structure was developed in the early stages of the solar cells research on Si-based devices. Currently, $Cu(In,Ga)(S,Se)_2$ (CIGS), $Cu_2ZnSn(S,Se)_4$ (CZTS), CdTe, hybrid Si/CNT solar cells, organic photovoltaic (OPV) and GaAs systems are adopting this

structure. Among them, CIGS is one of the promising materials to achieve lightweight and low cost devices because of its ease of processing for polycrystalline thin films to achieve high performance. A typical structure is based on a lightly doped p-type semiconductor material combined with a heavily doped n-type semiconductor material. Due to the poor carrier mobility of holes, the wider depletion region should occur in the p-type material and assist the charge separation and transport. Most photogenerated carriers can be extracted efficiently with proper controls of the film thickness and doping concentrations.

Another type of solar cell structure consists of back electrode/p-type/i-type/n-type/top electrode as shown in Figure 1.1b. This structure comes from improving the p-n junction structure of Si solar cells. To control and to introduce a specific amount of dopants over an entire Si wafer requires long time processing and high-temperature post-annealing. Moreover, the extrinsic doping would induce more defects in the materials resulting in more recombination. The p-i-n solar cell structure overcomes these technical and fundamental issues and further improves device performance. Currently, amorphous Si (a-Si), crystalline Si solar cells, heterojunction with intrinsic thin layer (HIT) and halide perovskite solar cells adopt this structure. Generally, the thin and highly doped p-type and n-type layers are used at both sides of the intrinsic layer for charge separation and collection and the intrinsic layer is the main photon absorber. Though Si and HIT solar cells have

achieved high efficiencies compared to other materials, their cost-effectiveness and preparation process are still under investigation. The halide perovskite materials emerge as potential candidates for thin-film solar cell applications. In this dissertation, we will focus on two next-generation materials, CZTS (to replace CIGS) and halide pervoskite materials, and the details of these materials' properties are discussed in the section 1.3.

The schematic diagram for the working principle of photogeneration and carrier transport is shown in Figure 1.1c and d. When the light shines through the transparent electrode, a photon exited an electron from the valence band to the conduction band and generated a bonded electron-hole pair (exciton). The exciton will be separated by the built-in potential through the p-n junction into free electron and hole. The free electron and hole will be transported to the electrodes and then to the external circuit. The built-in potential from the p-n junction is established as shown in Figure 1.1d. The conduction band bending and valence band bending in the depletion region is the main driving force for charge separation and collection. In the other case, the p-i-n structure device has two interfaces, p-i and i-n. These two interfaces will form built-in potentials and these built-in potentials can span across the entire i-type layer by tuning the thickness of i-type layer or carrier concentrations of the semiconductor layers. Controlling the building potential and the depletion width are critical for efficient separation of excitons and achieving good charge transport and

collection.

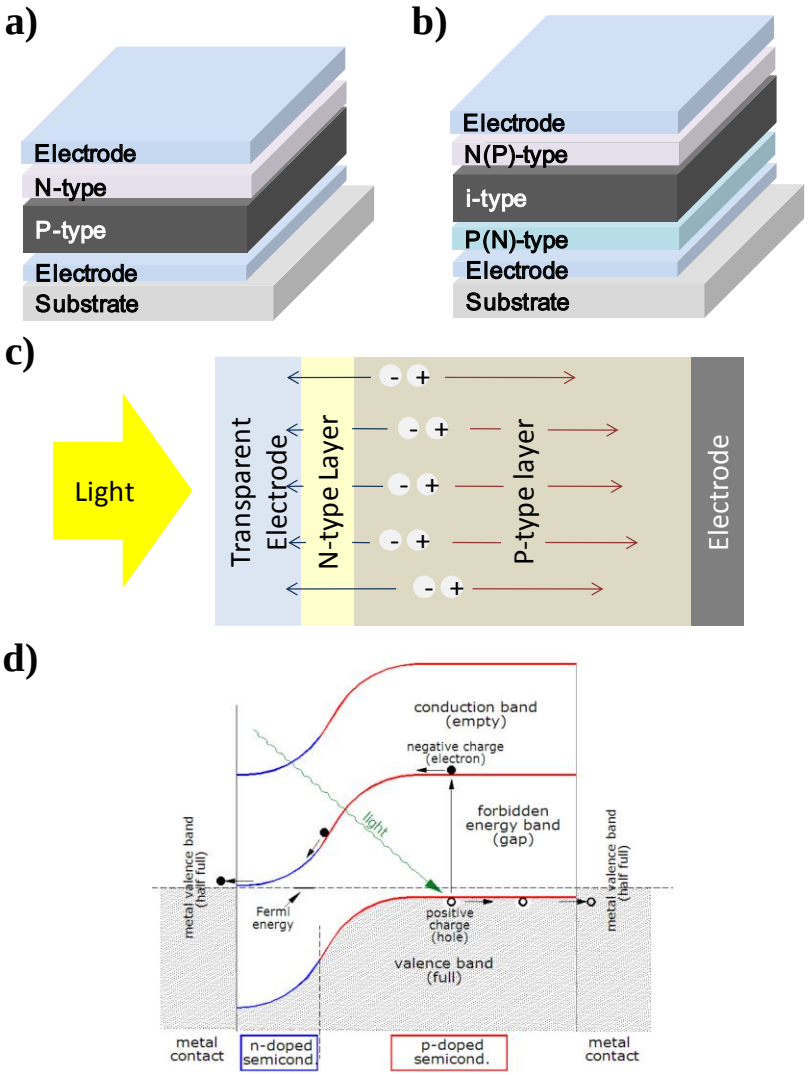

Figure 1.1 (a) Schematic diagram of p-n junction solar cells; (b) schematic diagram of p-i-n junction solar cells; (c) schematic diagram of charge transport in p-n junction solar cells; (d) schematic diagram of energy band diagram and charge separation in p-n junction solar cells.[2]

Evaluating solar cell performance is based on their ability to produce electrical power under illumination. The power conversion efficiency of a solar cell is determined by its

simultaneously produced voltage and current, which make up its power output. The typical characterization of a solar cell is extracted by applying an external voltage and measuring its current output at various bias levels under illumination. The solar cell performance is evaluated by power conversion efficiency (PCE):

$$\mathrm{PCE} = \left(\frac{(\mathrm{V}\times\mathrm{J})at\ \max power\ point}{input\ light\ power\ per\ unit\ area}\right) = \left(\frac{Voc\times Jsc\times FF}{input\ light\ power\ per\ unit\ area}\right).$$

The open-circuit voltage (V_{OC}) is the voltage at the open-circuit point; the short-circuit current density (J_{SC}) is the current density at the short-circuit point and the maximum power point is the maximum value of current times voltage. All these parameters are indicated in a sample current-voltage (I-V) curve shown in Figure 1.2. The fill factor (FF) is the ratio between V*J at maximum power point and V_{OC}*J_{SC} that could also be represented as the area ratio between the dark doted line and red doted line in the 4th quadrant. The cell's J-V characteristics depend on the various material properties and interactions that take place within the cell and thus is a far more complex matter, which has been and will continue to be the topic of intensive research. The various observations and trends presented in this dissertation represent a single piece of an increasing entity and hopefully offer insight that will be useful in future developments.

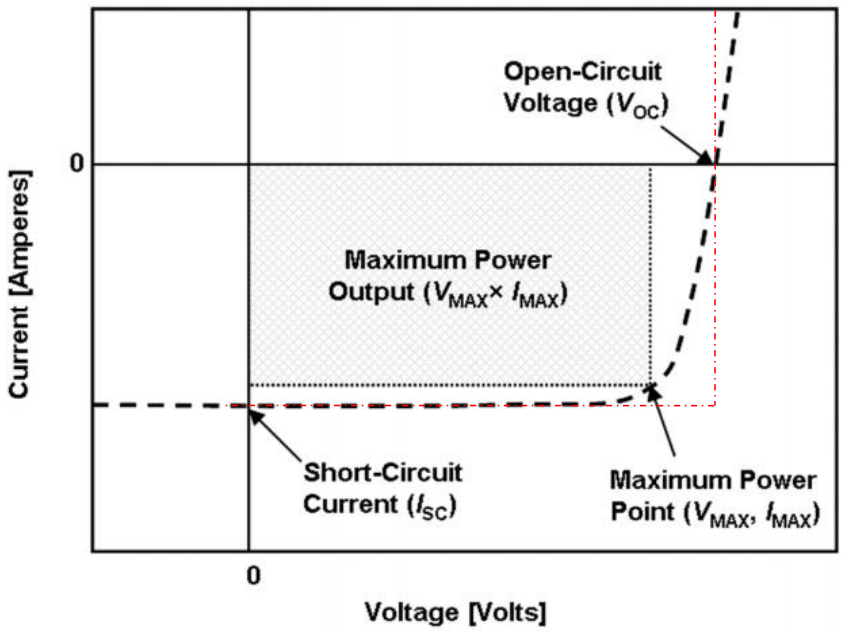

Figure 1.2 An example of current-voltage (I-V) curve. I_{SC} = J_{SC} x device area.

1.2 Current Status of Transparent Electrodes

Transparent conducting electrodes are crucial parts in all kinds of optical electronics. Using solar cells as an example, charge carriers are generated uniformly across the entire cell area and must be collected from a large region with minimal power loss. Meanwhile, the ability of photons to transmit through the window layer determines the efficiency of the photocurrent generation. Based on these two considerations, the sheet resistance and transparency are the key parameters to determine the quality of a transparent electrode.

Currently, the majority of transparent conductors used in the solar cells devices are doped metal oxide films. Among all the metal oxide materials, tin-doped indium oxide (ITO),

aluminum-doped zinc oxide (AZO) and fluorine-doped tin oxide (FTO) are commonly used in practical applications due to their relatively low sheet resistance and high transparency in the visible region.[3] Among these three, ITO is the most common transparent electrode in solar cells, light-emitting diode, and touch panel technologies. However, the increasing demand for the raw material, especially indium, with the rapid development of flexible electronics, makes it critical to search for alternatives to replace ITO.[4] Moreover, the sputtering deposition of high quality ITO is a low-throughput process and requires elevated temperatures. Solution-processed ITO also requires high temperature annealing to achieve good conductivity.[5] It is vital therefore to only use substrates that are stable at high temperatures, which means increased substrate cost and reduced performance on plastic substrates.

Considering all these factors, emerging techniques are proposed to fulfill both the standard requirements on the sheet resistance and transmission, and that can be formed by low-cost processes, such as spin-coating, spray coating and roll-to-roll processes.[6] Carbon nanotubes (CNTs), conductive polymers, graphene as well as metal nanowires have been investigated for use as transparent electrodes.

CNTs have the unique electrical property that they can be either metallic or semiconducting.[7] The high stability, flexibility, and mobility of CNTs make the CNT

network a potential candidate to replace the rigid ITO substrate. The current challenge of using CNTs as a transparent electrode is high wire-wire contact resistance, which results in the relative higher sheet resistances than other materials at similar transmittance.[4]

Among various types of conductive polymers, PEDOT:PSS and polyaniline (PANI) are currently the most popular materials of choice to replace the conventional ITO electrode. These two materials are well-studied conjugated polymers with excellent mechanical stability, flexibility and, more importantly, they can achieve relatively high conductivity and transparency. Currently, however, these polymers still exhibit lower conductivity and transmission than other candidates.[4]

Graphene is another promising candidate as a TCE in optoelectronics. A flexible two-dimensional sheet of sp^2-hybridized carbon atoms, it exhibits high conductivity and is nearly transparent. A single layer of graphene showed a sheet resistance of 125 ohm/sq and 97.4% transmission at a wavelength of 550 nm, which is superior to the ITO substrate and other reported TCEs.[8] The upcoming challenge for grapheme electrodes is to improve the electrical and optical properties while scaling-up the process, and to make the fabrication process faster, easier, and more cost effective.[4]

Last but not least, recent studies on the metallic nanowire's application in optical electronics have attracted a lot of attention. Similar to CNTs, high conductivity from the

metal material and high transmittance from the open space between nanowires make the metallic nanowire a potential candidate as TCE. Compared with CNTs, the metallic nanowire network shows better sheet resistance and transmission values, because the wire-to-wire contact resistance can be reduced by thermal treatment.[9] These materials can be easily processed to achieve high-performance devices. In terms of the sheet resistance and transmission as shown in Figure 1.3, the silver nanowire networks have been demonstrated to be comparable and even superior to ITO. However, based on the standard parameters is not enough to evaluate their potential for practical applications. Herein, to apply silver nanowire network to solar cells effectively, I have focused on the fundamental understanding of silver nanowire networks and developing novel processes to integrate silver nanowire networks for electronics in Chapters 2 and 3.[4]

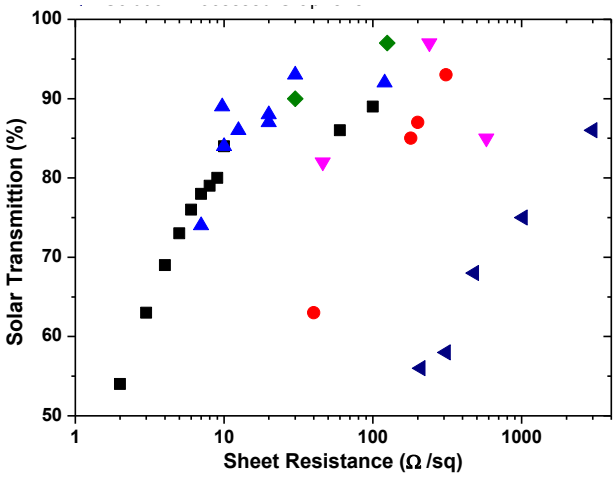

Figure 1.3 Sheet resistance and transmission chart for various types of transparent conducting electrode materials including CNTs, silver nanowires, conductive polymers, and graphene. Adapted with permission from ref. (4). Copyright 2014 MDPI.

1.3 Emerging Thin Film Photovoltaics

As mentioned in Sec. 1.1, there are different emerging absorber materials in solar cell research. Among thin film solar cells, CIGS solar cells have been demonstrated to have PCEs over 20%.[10] The limited availability of indium for large-scale implementation led to growing interest in solar materials that contain only earth-abundant elements. In addition, the capability of solution processing for high-performance solar materials is ideal for future applications. Therefore, CZTS and halide perovskite solar cells become two of the most promising alternatives.

1.3.1 $Cu_2ZnSn(S,Se)_4$ Solar Cells

Kesterite CZTS has a similar structure to chalcogenide CIGS, with the zinc and tin alternating on the lattice sites that are occupied by indium or gallium in CIGS, as shown in the Figure 1.4.[11] Consisting solely of earth-abundant, non-toxic, and inexpensive elements, kesterite CZTS offers a high absorption coefficient of $>10^4\ cm^{-1}$, which corresponds to less than 2 μm of absorption length for visible light, with an adjustable band gap that can range from 1.0 to 1.5 eV to match the solar spectrum.[12-14] Kesterite CZTS thus opens the door for both economic and environmental friendly thin film device production without limitations of raw materials.

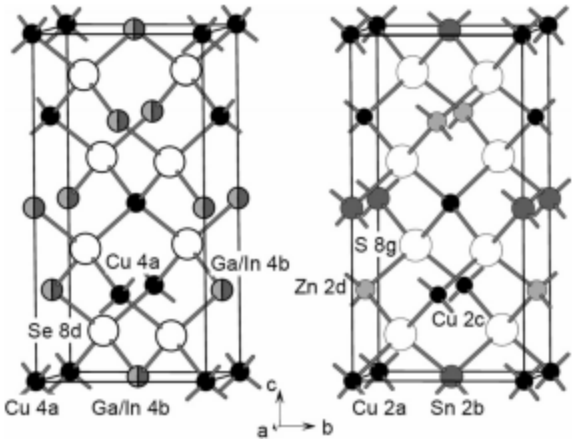

Figure 1.4 Comparison of the crystal structure of chalcopyrite and kesterite. Adapted with permission from ref. (4) Copyright 2012 Wiley

The device structure used in high performance kesterite CZTS devices is identical to that used in chalcogenide CIGS, as shown in Figure 1.5.[15] Molybdenum (Mo) bottom electrodes provide stability against high-temperature post-annealing process in CIGS and CZTS and resistivity against their constituent elements. Kesterite CZTS materials were deposited onto A Mo back contact and annealed at high temperature in selenium vapor to enhance grain growth and phase formation. An n-type cadmium sulfide (CdS) layer, which is widely used in the high efficiency CIGS devices, is also adopted in CZTS devices. CdS layers were deposited by a chemical bath deposition (CBD) process and they are reported to passivate defects effectively and produce a generally benign interface. Following the n-type CdS layer, a thin intrinsic ZnO layer is commonly used to reduce the localized shunting pathways through CIGS or CZTS/CdS junctions. Transparent electrode ITO is

then sputtered onto the ZnO layer and serves as the window layer for light harvesting. The ZnO and ITO layers are vacuum deposited.[16] Researchers including our group have been working on developing a novel process to replace the traditional methods.

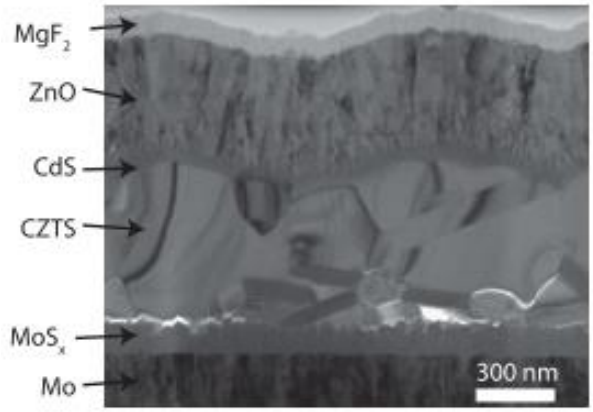

Figure 1.5 CZTS solar cell structure: cross-sectional transmission electron microscopy bright field image. Adapted with permission from ref. (15) Copyright 2011 American Institute of Physics

Rapid progress in kesterite CZTS material development has advanced its conversion efficiency to beyond 12% in the last few years.[17, 18] Kesterite CZTS materials were prepared via various methods and their best device performances were concluded in Table 1.1.

Table 1.1 A summary of the best CZTS device efficiencies prepared using different methods. For the definitions of efficiency, V_{OC}, J_{SC}, and FF, see Sec 1.2.

Methods	Efficiency (%)	V_{OC} (mV)	J_{SC} (mA/cm^2)	FF (%)	Ref

Hydrazine-based	12.7	466	38.9	69.8	[18]
Nanocrystal-based	9.85	457	32.6	66.1	[19]
Sol-gel-based	8.3	443	31.2	60.2	[20]
Co-evaporation	11.6	423	40.6	67.3	[21]

Currently, the highest performance is achieved by a hydrazine-based solution processing with 12.7% PCEs in IBM T. J. Watson.[18] However, hydrazine is not an ideal solvent for industrial applications. Therefore, researchers have been working on nanocrystal-based and sol-gel solution processes using relatively non-toxic solvents.

The nanocrystal approach starts with the synthesis of metal chalcogenide nanocrystals, followed by the deposition of nanocrystal films, and ends with the post-thermal treatment of films. Currently, cell efficiencies up to 9% have been achieved and the record is only slightly lower than hydrazine-processed kesterite solar cells, and similar to that achieved with co-evaporated kesterite solar cells.[19] Moreover, the nanocrystals can be dispersed with polar or non-polar solvents by changing the surface ligand during the synthesis, making it compatible with a number of deposition techniques including spin-coating, spray coating, blade coating, and dip coating.[12]

Although sol-gel processed CZTS has relatively low device performance, the sol-gel process is more environmentally-friendly than other methods. The commonly used solvents

in sol-gel processes are either alcohol-based solvent or water-based.[22] In addition, the precursor is easily prepared by directly dissolving components into the solvent without further synthesis step. Sol-gel processing is still under development and it is believed to be a competitive method with further studies.

1.3.2 Halide Perovskite Solar Cells

Perovskite materials follow the general formula ABX_3 and adopt the same crystal structure as calcium titanate. In this arrangement, the 'A' and 'B' cations coordinate with 12 and 6 'X' anions, forming cuboctahedral and octahedral geometries, respectively (shown in Figure 1.6.).[23] A compound's tendency of forming perovskite can be estimated using the Goldschmidt tolerance factor,[24] although determining the chemical and thermal stability of the resulting structure invariably requires more detailed analysis. The perovskite materials family exhibits a wide range of electronic behavior including piezoelectric, thermoelectric, semiconducting, and superconducting properties depending on the specifics of the material.[25-27] In the early 1990s, Mitzi and coworkers made an extensive investigation into the optoelectronic properties of organometallic halide perovskites, where the 'A' sites are occupied by organic cations, the 'B' sites are occupied by group IV cations (Sn, Pb), and the 'X' sites are occupied by group VII anions (Cl, Br, I).[28-30]

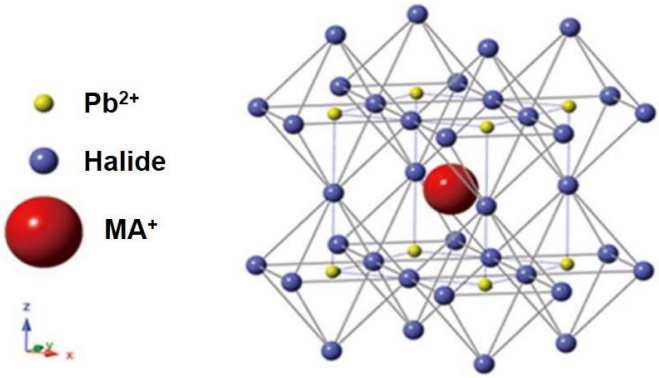

Figure 1.6 Crystal lattice of the methylammonium lead halide ($CH_3NH_3PbX_3$) perovskite structure. Adapted with permission from ref. (23). Copyright 2013 Nature Publishing Group.

Lead halide perovskite solar cells are rapidly approaching PCEs of 20% after only 5 years of concerted development, an achievement that required decades of effort for conventional materials.[31-33] The most successful perovskite materials thus far are variations on the compound $CH_3NH_3PbX_3$ (X=Cl, Br, I), which exhibits the most attractive properties of ideal PV absorbers: 1) Strong optical absorption due to *s-p* anti-bonding coupling; 2) High electron and hole mobilities and diffusion lengths; 3) Superior structural defect tolerance and shallow point defects; and 4) Low surface recombination velocity and benign grain boundary effects.[34-37] Additionally, the ambipolar transport properties make these materials feasible to various device designs.[38]

Table 1.2 sums up the $CH_3NH_3PbX_3$ material properties and compared them to that of other kinds of absorber materials.

Table 1.2 A summary of the perovskite, Si, CIGS and GaAs materials' properties.

	$CH_3NH_3PbI_3$	**Si**	**CIGS**	**GaAs**	Ref
Band gap (eV)	1.5	1.1	1.12	1.43	[31]
Absorption coefficient	$10^{4\text{-}5}$	10^{3}	$10^{4\text{-}5}$	$10^{4\text{-}5}$	[34]
Carrier mobility $cm^2/(V \cdot s)$	Up to 2000	1500	< 10	8500	[39]
Carrier concentration	$10^{16\text{-}17}$	10^{16}	$10^{15\text{-}16}$	10^{17}	[40]
Carrier lifetime	>100 ns	~ms	50-200 ns	<100 ns	[41]

Comparing to the current commercially available solar materials, the halide perovskite $CH_3NH_3PbI_3$ has a high absorption coefficient due to its direct band gap and exhibits even higher absorption above its band gap than CIGS and GaAs.[34] Furthermore, the long carrier lifetime and high carrier mobility indicated less recombination and efficient charge transport. Its diffusion length can be more than 1 μm, which is comparable to indirect band gap materials, such as Si.[41] It also shows a relatively high carrier density, which implies a small resistance for bulk material, and the low material resistance can result in a small series resistance for the solar cell devices. Due to all these superior properties, $CH_3NH_3PbI_3$ device shows a high performance as listed in Table 1.3 together with that of other solar materials.

Table 1.3 Summary of $CH_3NH_3PbX_3$ device parameters as compared to other kinds of absorber materials.

Table 1.3 A summary of solar cell performance of the perovskite, Si, CIGS and GaAs materials.

	$CH_3NH_3PbI_3$	**Si**	**CIGS**	**GaAs**	Ref
V_{OC} (V)	1.1	0.706	0.68	1.12	[31]
V_{OC} deficit	0.3 - 0.45 V	0.3-0.4V	> 0.4 V	~0.3 V	[31]
J_{SC} (mA/cm^2)	~ 22	42.7	36	29.5	[10]
FF	~80%	~ 80%	~80%	>85%	[10]
Film thickness	~350 nm	100-200 um	1-2 um	2 um	[10]
Efficiency (%)	20.1	25.0	21.7	28.8	[10]

$CH_3NH_3PbI_3$ perovskite materials can achieve a PCE higher than 20% with less than half a micrometer thickness, showing outstanding FFs and minimal V_{OC} loss, thus attract huge attention and research efforts around the world.

Currently, preparation of halide perovskite solar materials is catalogued into one step and sequential deposition (either in solution or vacuum) techniques. One-step processing is based on the co-deposition of both the organic and inorganic components either through solution processing or thermal evaporation. In solution processing, a mixture of MX_2 (M =

Pb, Sn; X = Cl, Br, I) and AX (A = MA^+, FA^+) is dissolved in an organic solvent and deposited directly to form a film, followed by thermal annealing to produce the final perovskite phase.[42] Meanwhile, thermal evaporation employs dual sources for MX_2 and AX with different heating temperatures to form the perovskite film.[38] Sequential deposition means depositing an MX_2 (M = Pb, Sn; X = Cl, Br, I) layer such as PbI_2 and an AX (A = MA^+, FA^+) such as methylammonium iodide sequentially followed by heat treatment to form the completed perovskite film.[43-45] Typically, the deposition of MX_2 is achieved using spin-coating, while AX can be introduced by (1) spin-coating the AX solution on top of the MX_2 layer, (2) immersing the MX_2 layer in the AX solution to induce a solid-liquid reaction, or (3) exposing the MX_2 layer to AX vapor at elevated temperatures.[46-48] Also, two-step sequential deposition can be carried out in thermal evaporation, by sequentially depositing the inorganic and organic components. The schematic diagrams of different deposition methods are shown in the Figure 1.7.

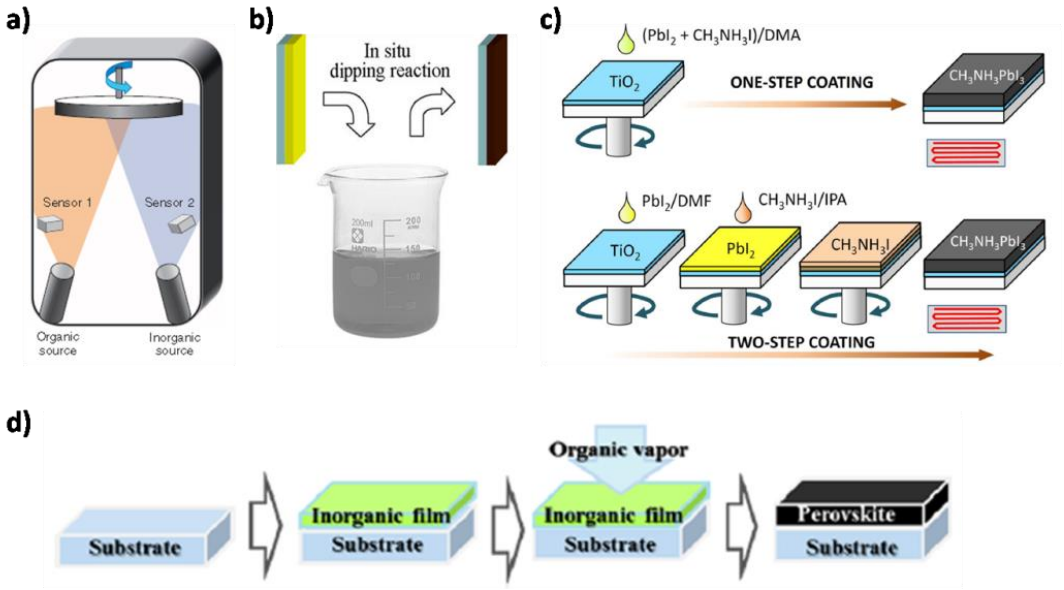

Figure 1.7 The preparation of CH3NH3PbI3-xClx film from different deposition methods: (a) Dual source coevaporation using $PbCl_2$ and MAI source; (b) Sequential deposition by dipping the PbI_2 film into MAI solution; (c) One-step solution process based on the mixture of PbI_2 and MAI, and sequential coating of PbI_2 and MAI; (d) Vapor-assisted solution process using the MAI organic vapor to react with PbI_2 film. Adapted with permission from ref. (38, 46, 47, 48). Copyright 2013 Nature Publishing Group, 2014 American Institution of Physics, 2014 American Chemical Society

The power conversion efficiency has been pushed from 3.8% to 20.1% based on interface design and controlled perovskite film growth. Here, several of the main milestone findings in perovskite research are summarized. In 2008 and 2009, Kojima *et al*. used $CH_3NH_3PbI_3$ and $CH_3NH_3PbBr_3$ as the light-harvesting dyes in mesoporous dye-sensitize solar cells (DSSC) and achieved a PCE of about 3.8%.[49] Later, Im *et al*. optimized the fabrication conditions, delivering a 6.5% PCE.[50] However, $CH_3NH_3PbX_3$ (X = Br, I) was found to dissolve in polar solvents, rendering the perovskite solar cells incorporating a liquid

electrolyte layer unstable. This instability was eventually resolved by adapting solid hole conductors in place of the liquid redox electrolyte and a PCE as high as 9.7% was achieved.[51] Subsequently, an insulating Al_2O_3 network was used to replace conducting nanoporous TiO_2 template. Using a mixed $CH_3NH_3PbI_{3-x}Cl_x$ as the sensitizer, an improved open-circuit voltage (V_{OC}) was demonstrated, and the reported efficiency was boosted to 10.9%.[52]

In 2013, a two-step procedure of CH_3NH_3I intercalation following layered PbI_2 deposition resulted in a PCE of 15% and a certified PCE of 14.1%.[53] Similar results using a planar cell configuration to eliminate the mesoporous structure in DSSC and a $CH_3NH_3PbI_{3-x}Cl_x$ absorber deposited by a two-source thermal evaporation produced a reported efficiency of 15.4%.[38] This result indicates that a mesoporous structure such as TiO_2 is no longer required, further confirming the ambipolar transport of perovskite materials.

The highest PCE obtained by a significant margin was reported from the Korean Research Institute of Chemical Technology (KRICT) at 17.9%.[54] There are additional reports of equally high or higher efficiency values, although difficulties regarding packaging and encapsulation have reduced the number of these reports that result in certified efficiency values. As a recent example, our group has produced cells with a PCE of 19.3% through careful interface design and film formation control.[55] The latest result was reported by

KRICT with a PCE of 20.1% but no detail was released.[54] The PCE trend of each of these reported values is shown in Figure 1.8. Researchers are striving to explore the potential of these materials and to solve the stability issues for future applications.

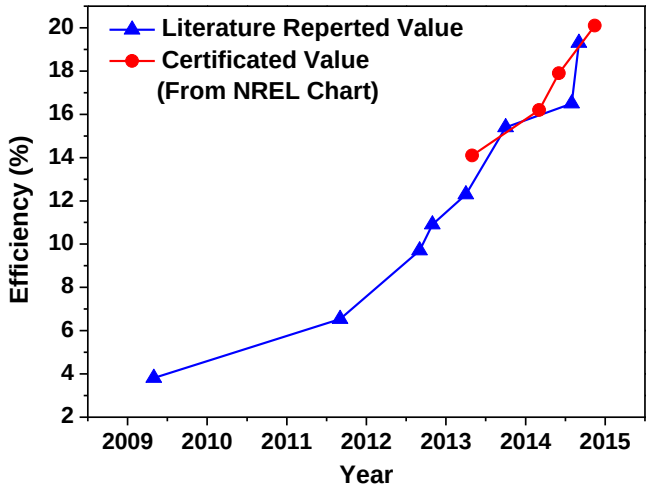

Figure 1.8 Efficiency trend of $CH_3NH_3PbX_3$-based perovskite solar cells collected from literature reported value and NREL report chart.

Chapter 2 Nanoscale Joule Heating and Electromigration Enhanced Ripening of Silver Nanowire Contacts

2.1 Introduction

As mentioned in Chapter 1, with the recent demand for thin, transparent, conducting films and flexible devices, nanomaterials such as carbon nanotubes,[56, 57], graphene,[8, 58] and metallic nanowires[59-61] have emerged as promising alternatives to replace the brittle ITO. In particular, silver nanowire networks provide excellent transmittance and conductance and thus have been brought forward as a potential candidate for transparent conductors (TCs) in thin film optoelectronic devices,[62] such as touch panels, light-emitting diodes, and solar cells, due to their potential high-throughput, low-cost fabrication, flexibility, and solution processability. However, the high contact resistance between silver nanowires coming from the insulating surfactant coating of polyvinylpyrrolidone (PVP) and loose contact between individual silver nanowires remains a critical issue, making extra processing steps necessary in order to achieve low sheet resistance values desirable for practical applications.[63]

Many processing techniques have been reported to address this issue, including heat treatment (featuring either a high processing temperature or long treatment time),[59]

mechanical pressing,[64, 65] electrochemical ion exchange,[66] vacuum filtration,[67] metal-oxide nanoparticles fusing,[68, 69] plasmonic welding process,[70] etc. Some of these methods require the use of high input powers or long treatment durations, while others suffer from obvious scalability issues, shadow effects, or may damage chemically sensitive substrates. Recent reports demonstrated that Joule heating can weld platinum wires and carbon nanotubes by precisely controlling the contact geometry and current flow between the two wires.[71, 72] With forming point contacts, hot spots can be generated at the contact point because of the high local current density. In this work, passing current through the small contact points between the wires with residual insulating surface ligands from the chemical synthesis process successfully generated enough power to weld all the contacts of the wires across the entire large-area devices. During this process, electromigration occurred at the high current density regions in the nanowire network in and near the contact regions, which plays a critical role in determining the electrical properties of the metallic nanowires network and therefore is crucial for the future applications of the metallic nanowires.[73] This method is easily transferable to large-scale silver nanowire networks where substantial improvement in the conductivity of these silver nanowire network electrodes can be achieved at low temperatures and by using only a small amount of input energy over the treatment duration of a few seconds. This process enables

us to obtain low resistance silver nanowire networks and employ them as electrodes in devices that require relatively gentle processing conditions, such as polymer solar cells in which an efficiency enhancement of a factor of 20 is demonstrated in this work.

2.2 Experimental Details

2.2.1 Preparation of Silver Nanowire Network Films

Silver nanowires were obtained from Blue Nano Inc. (Charlotte, NC, USA). A schematic diagram of the experimental set-up is shown in Figure 2.1a, with the red dots indicating hot spots for the electro-welding process. The silver nanowires were either synthesized according to previous reports[66] or commercially available silver nanowires. Silver nanowires were spin cast on a glass substrate (1.5 x 1.2 cm^2) patterned with evaporated metal electrodes to form the nanowire network. Different silver nanowire area densities as transparent conductors are prepared by mulitple times of spin casting with silver nanowire dispersion.

2.2.2 Fabrication of Single Contact Devices

Silver nanowires are dispersed onto SiO_2 substrates and then spin coated with methyl methacryllate (MMA) and poly(methyl methacryllate) (PMMA) as photoresists (PR). In order to avoid thermal effect to the Ag wires contact, PR are not baked after spin coating.

Silver films with 100 nm were patterned by e-beam lithography and then deposited to serve as electrodes.

2.2.3 Characterizations of Silver Nanowire Network Films

Scanning electron microscopy images were taken on a Nova Nano 230 electron microscope and cross-section SEM images were taken by a FEI Nova 600 Nanolab Dualbeam^{TM} SEM/FIB for structural properties of the nanowire contact. The transmittance spectra were taken using a Hitachi ultraviolet–visible spectrophotometer (U-4100). Thermally evaporated Cr/Au (2 nm/50 nm) through the shadow mask was used as the metal pads on glass substrate to define the 0.6 cm in length (L) and 1.2 cm in width (W) channel. The two-point probe method was used to estimate the sheet resistance of the film defined by R_{sh}= R(W/L). After the annealing process, the sheet resistance was also tested using a four-point probe method with a sheet resistivity meter (Guardian Manufacturing, Model: SRM-232-100, range: 0 to 100 ohm/sq) to varify the value. A HP E3631A Triple output direct current power supply with 25 V compliance voltage was used to apply current to the silver nanowire network and the resistance was converted by the voltage and current recorded in the process and then transfered to the sheet resistance for comparison. For single- contact devices, silver nanowire contact resistance measurements were performed on an Agilent

semiconductor parameter analyser using 0.1 V and connecting to a 500 ohm resistor.

2.3 Results and Discussion

2.3.1 Electrical Properties and Morphologies

Morphologies of the silver nanowire contacts before the electrical current treatment was shown in Figure 2.1b and the sharp interface between the two nanowires in contact is observed. After a current treatment at 0.2 A limit with 25 V compliance voltage for 30 seconds, different morphologies of contacts were formed and characterized using the tilt-angle SEM (Figure 2.1c and d). In the case shown in Figure 2.1c, the contact was welded and the top wire had deformed towards the bottom wire. Figure 2.1d showed a contact in which only the one side of the contact welded significantly forming an asymmetric contact morphology, which is not seen from those welded contacts produced by other treatment methods such as heating and plasmonic welding, which invariably produce a symmetric contact shape at the wire-wire contact. A low-magnification, tilted SEM image was also taken after the treatment (Figure 2.1e), showing contact morphologies distinct from those produced by other processes.[70] The difference in the symmetry of the contact morphology indicates that a different joining mechanism is at work in our point contact treatment.

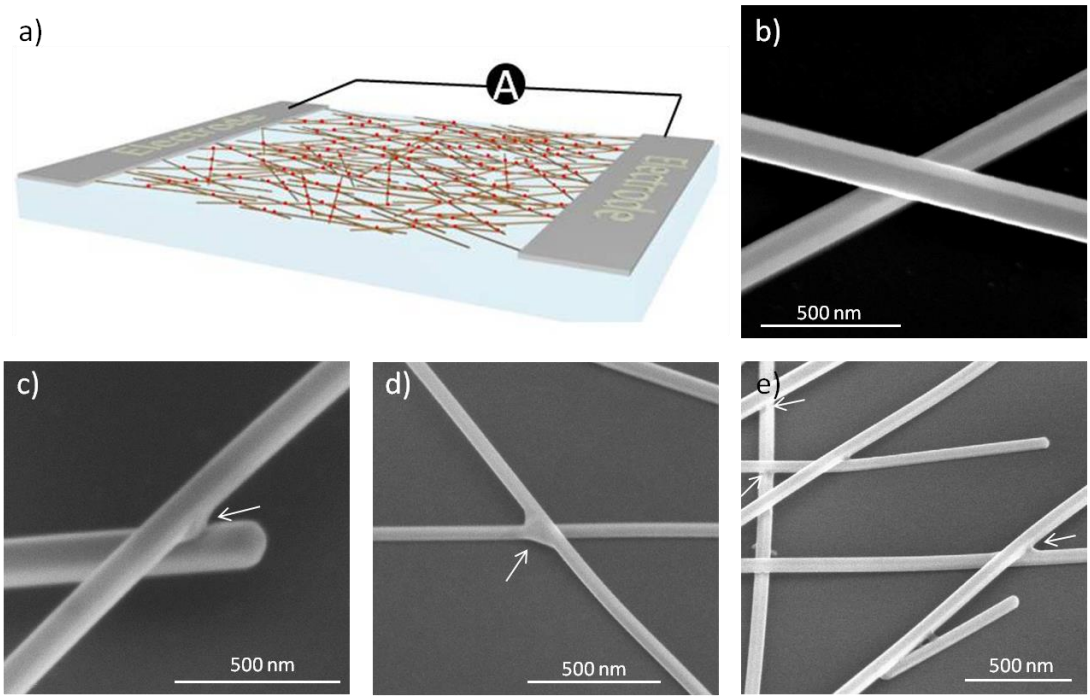

Figure 2.1 Experimental set-up and SEM images before and after electrowelding treatment; (a) Schematic diagram of the experimental set-up, with a continuous network of nanowires allowing for the passage of current between two metal electrodes; (b) Tilted (45°) SEM images of the initial silver nanowire contact; (c,d) nanowire contacts after the electrowelding treatment, different morphologies of the silver nanowire contacts are observed under tilted SEM; (e) A wider view of several nanowire contacts after the passage of current. The arrows indicated the deformation of the nanowire contacts.

In order to understand the reaction taking place at the contacts, an isolated two-wire contact system was fabricated, as shown in Figure 2.2a. The direction of the applied current is indicated by red arrows. A 500 ohm resistor was connected to introduce a current limit under 0.1 V bias for the structure. Before current treatment, the resistance of the two-wire device was larger than 10^{10} ohm due to the large point contact resistance. After the current treatment with a maximum current density of around 1.5×10^7 A/cm^2, calculated from the

maximum current value to the cross section area of the small nanowire, the resistance was dramatically reduced to 185 ohm, as shown in the I-V curves depicted in Figure 2.2d. The ratio between the power generated at the contact and within the nanowire can be expressed as $P_c/P_w = R_c/R_w$, in which R_c and R_w are the two-wire contact resistance and nanowire resistance, respectively. From experimental results, $R_c + R_w$ is larger than 10^{10} ohm, and we can estimate the average R_w from the silver nanowires dimensions to be ~180 ohm. This results in the conclusion that $R_c >> R_w$, indicating that nearly 100% of the heat generation will be localized at the contact with little heating effect in the bulk of the silver nanowires. The contact morphology of the two-wire device was characterized from different viewing angles, left (L) and right (R), as shown in the Figure 2.2a, after applying the electrical current (Figure 2.2b and c) and the same asymmetric shape of the contact, similar to those in the larger film, was observed. The cross-section of the contact was made using focused ion beam (FIB) and characterized with SEM to gain more insight into the contact formation. As shown in the inset of Figure 2.2c, the top nanowire deforms around the bottom nanowire, and the final contact shape formed to favor a good electrical connection between the two. It is observed that, in general, the nanowire with the smaller diameter of the two tends to take on the majority of the morphological changes and the most extreme changes take place at the corner of the contact.

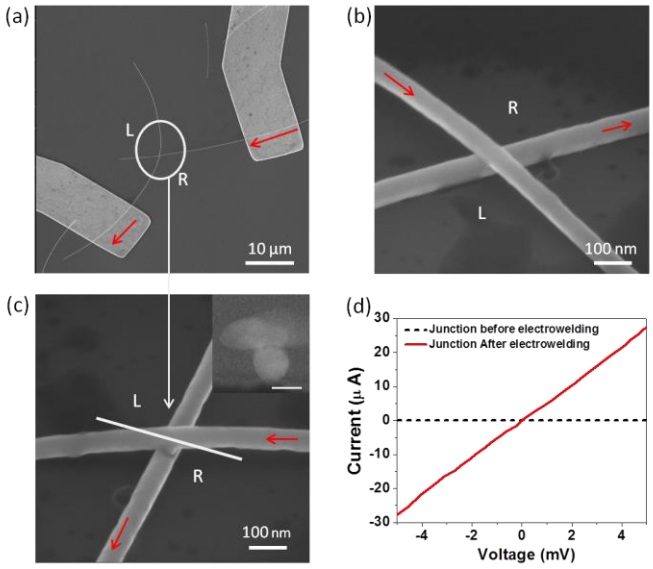

Figure 2.2 Two-wire contact measurement and characterization. (a) An SEM image of a two-wire device, with the red arrows indicating the direction of current flow. (b, c) Tilted (52^{o}) SEM image of the silver nanowire contact from the different directions. The diameters of top and bottom nanowires are around 49 nm and 58 nm, respectively. The reacted contact was found at the R (right) corner of the silver nanowires. The cross-sectional SEM image of the two silver nanowires contact is shown in the inset of (c), with the majority of deformation clearly concentrated in the upper nanowire. The scale bar of the inset is 50 nm. (d) Current-voltage measurements before and after current passing, the current of pristine device is in the pA region and the post-treatment device is in the μA, as shown in the figure.

2.3.2 Mechanism of the Eletromigration in Nano-Contact

This process can be simulated using a finite element method, showing three stages of reaction taking place, corresponding to our previous observation from cross-sectional SEM images (Figure 2.3). The images in Figure 2.3 only show a quarter of the simulated structure to highlight the current distribution near the contact. In Figure 2.3a, the point contact between two pristine nanowires leads to current concentrating into a relatively

small volume, and the presence of surfactants such as PVP will result in even larger heat generation due to the high current density and high contact resistance. Under these conditions, strong Joule heating will occur at the contact. Once enough heat is generated at the contact, increased surface and bulk diffusion of silver atoms will allow for the welding of the point contact to achieve a larger contact area. Furthermore, the tendency for the smaller nanowire to deform preferentially (as in Figure 2.1c) can be explained by the dependence of the free energy on the diameter of the nanowire. According to Gibbs-Thomson theory, the Gibbs free energy increases sharply with smaller particle dimensions due to an increased contribution from the Gibbs-Thomson potential, $\Delta G = 2\gamma\Omega_m/r$, where γ is the surface energy, Ω_m is the volume per atom of investigated material, and r is the radius of the nanowires. The silver nanowire with the smaller diameter is subject to a higher potential energy, and is therefore comparatively unstable compared to the larger wire. With the localized temperature increase produced by Joule heating, the silver atoms in the smaller wire will obtain enough thermal energy to diffuse rapidly onto and around the other wire. Similar electrical sintering reactions in silver nanoparticles had been studied both experimentally and through simulation previously.[74-76] The reaction can happen at a time scale of milliseconds with reaction temperatures exceeding 100 °C.[75] It was established that the surface diffusion activation energy of noble metal atoms is typically

less than 1 eV[77, 78] and the process can happen even at room temperature. With the Joule heating and the reduction of the surface diffusion activation energy from the high Gibbs-Thomson potential, the process can occur in a short time. Eventually, a reacted contact is formed, generally adopting a shape similar to that shown in Figure 2.3b, which is reflected in the result in Figure 2.1c.

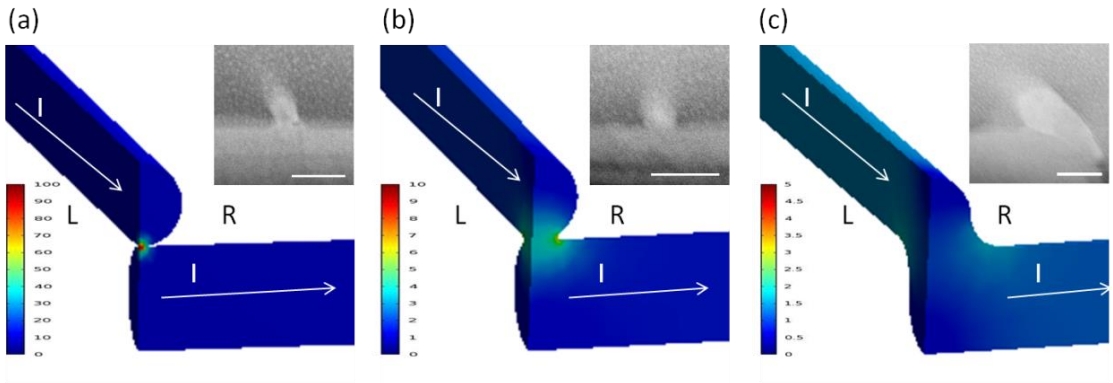

Figure 2.3 Finite element simulation of the current density distribution at different contact morphologies. (a) Simulation and cross-sectional SEM of a pristine point contact between two silver nanowires. Extremely high current density occurs at the point contact. (b) Reacted contact morphology, showing the hot spot at the corner of the current flow direction. Localized high current densities can still occur under this morphology as larger amounts of current are forced through the contact. Electromigration can enhance the contact reaction and reshapes the contact into the a ripened contact geometry. (c) Ripened contact morphology, producing greatly reduced current crowding, and exhibiting a nearly uniform current density distribution through the contact. This morphology is more stable than the other two geometries, and provides the best contact conductance due to its large contact area. The scale bars in each figure indicate the magnitude of the current density. The arrows indicated the current flow dirction. Insets in each simulated current density figures are FIB-cut cross-sectional SEM images of the different contact morphologies. The scale bar in each inset is 100 nm.

After the formation of the reacted contact, reduced contact resistance will allow for increased current flow. However, the current density will not be homogeneous across the entire contacted region because the contact area is still smaller than the bulk of the nanowires. Additionally, in order to minimize the distance electrons travelled as they travel from one nanowire to the other, current crowding occurred and the current density was substantially higher at the inner corner of the contact. As shown in Figure 2.3b, the highest current density region was at the corner of the contact instead of the center of the contact. This current crowding can introduce an enhancement to the local current density up to one order of magnitude from the simulation and previous report.[73] In a two-wire contact system, average current density was on the order of 10^7 A/cm^2, which indicated a current density of around 10^8 A/cm^2 at the corner of the contact. Comparing with the data from copper interconnect technology, surface-diffusion induced electromigration occurs at the Si device operation temperature of 100 °C with a current density of 10^6 A/cm^2. The melting temperatures of silver and copper are similar, therefore the high current density induced by the current crowding in our two-wire contact system ensures that electromigration can occur. The high current density region will cause the formation of a hot spot at the corner of the contact between the two nanowires and facilitate continued atomic movement via sustained Joule heating. Due to the fact that the directional current flow produces

asymmetric heating on the L and R sides of the contact, the R corner of the reacted contacts will produce a stronger force driving atomic vacancies to the lower current density region from what is known as the collision effect, typical of current crowding situations. Eventually, the net motion of atoms toward the high current density region forms a ripened contact, with a typical geometry similar to that shown in Figure 2.3c. The current density distribution in the ripened contact is more uniform than the previous two conditions (Figure 2.3a and b). Thus, the presence of the current crowding effects is likely the main reason behind the asymmetric shapes as those observed in the two-wire contact and nanowire network.

2.3.3 Transparent Electrode Performance and Device Application

To demonstrate the feasibility and effectiveness of this process in device fabrication, electro-welded silver nanowire network's performance as a transparent conductor is tested. The sheet resistance change as a function of treatment time was recorded under various current limits as shown in Figure 2.4a. Three different density of silver nanowire films were made with different initial sheet resistance values. The sheet resistance of all three films was significantly reduced by one to three orders of magnitude in the first 10 seconds of treatment, namely, $4x10^4$ ohm/sq to 91 ohm/sq at 0.2 A current treatment and $4x10^3$

ohm/sq to 157 ohm/sq at 0.1 A current treatment. After 30 seconds, the sheet resistance values saturated. Compared with those processed through thermal treatment on a hot plate, which requires temperatures of around 200 °C and treatment times of 10 to 20 minutes, this process is extremely fast and requires minimal power input into the nanowire network. Furthermore, this process can bring the sheet resistance down to a value comparable with reports from silver nanowire networks with similar transmittance treated at 200 °C. In this case, the high initial contact resistance generated sufficient power at the contacts to enhance atomic diffusion and eventually induce current crowding effects to bring the contact resistance to a greatly reduced value similar to that observed in the two wires contact system. Under constant current conditions, the required voltage from the power supply dropped dramatically as the contribution of contact resistance within the network diminished, and the power consumption dropped off sharply after the first seconds. The maximum power input to the network at the 0.2 A current treatment in Figure 4a was determined to be around 6.9 W/cm^2, and the total energy input of the entire treatment was roughly 94 J/cm^2 during the 30 seconds treatment period. The power consumption in this process is much lower than those reported for other treatment processes including pressure treatment and plasmonic welding and its short processing time could make this process more suitable for mass production.[65, 70] Additionally, when the current limit is increased

to higher levels, the sheet resistance is further reduced, as shown in Figure 2.4b. The reduction in sheet resistance as the welding current is increased takes only a few seconds, similar to the duration of the initial process. The dependence of sheet resistance on welding current, even after the initial treatment, enables us to produce a continuously controllable resistance in silver nanowires networks, while opening up new avenues for the formation of well controlled nanowire contact properties by electrical methods.

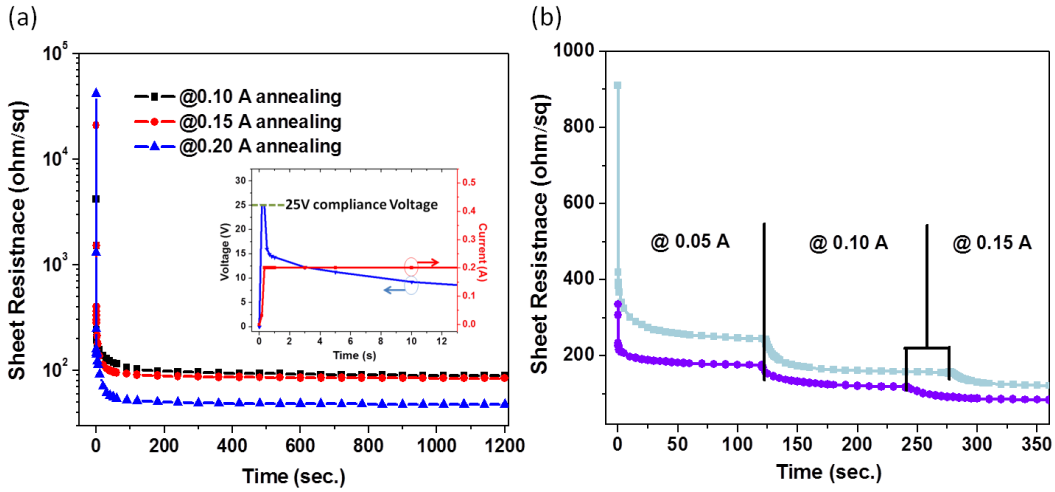

Figure 2.4 Controlling sheet resistance with time and current conditions. (a) Sheet resistance changes with time under different constant current conditions. Different films were treated with 0.1, 0.15, and 0.2 A, and stablized after around 30 seconds, with no significant changes after more than 20 minutes of continuous treatment. The voltage and current curves with 0.2 A limit are shown in the inset. (b) Current limit controlled sheet resistance of two silver nanowire networks with different nanowire area densities. The current value was increased at the inidicated times.

The optimized transmittance and sheet resistance (Figure 2.5a) values obtained from electro-welded nanowire networks were comparable to those calculated from percolation

theory[79-81] with a transmittance of 86.7% at 550 nm and a sheet resistance of 19.7 ohm/sq, indicating that this method is able to reduce the inter-nanowire contact resistance in the nanowire networks to negligible levels.[81] To demonstrate the effectiveness of localized contact welding in practical applications, silver nanowire networks were incorporated into an OPV device as the top electrode. The silver nanowire network was spun cast on top of fabricated polymer solar cell layers (ITO/ZnO/P3HT:$PC_{60}BM$/PEDOT:PSS) as the electrode, and the current density-voltage curve (J-V curve) was measured both before and after the electro-welding. As shown in Figure 2.5b, the as-coated device shows an extremely low FF and J_{sc}. High inter-nanowire contact resistance of the silver nanowire network appears to introduce a high series resistance into the device, which produced poor FF and J_{SC}. After the current treatment process, however, the FF and J_{SC} are significantly increased with the FF increasing from 25.03% to 37.59% and J_{SC} from 0.428 mA/cm^2 to 5.345 mA/cm^2. From the J-V curve, the series resistance was calculated to reduce from 1369 ohm/cm^2 to 7 ohm/cm^2. The power conversion efficiency was increased 20 times from 0.06 % to 1.18% by the welding treatment. The lower sheet resistance of the silver nanowire network results in more efficient transport of carriers and reduction of the power loss within the silver nanowire electrodes, which, in turn, leads to a higher fill factor, short circuit current, and ultimately

an enhanced solar cell efficiency. The fact that a stable V_{OC} value is attained after the treatment indicates that this current treatment process does not bring thermal damage to the layers underneath which can easily occur in relatively temperature sensitive OPV devices.

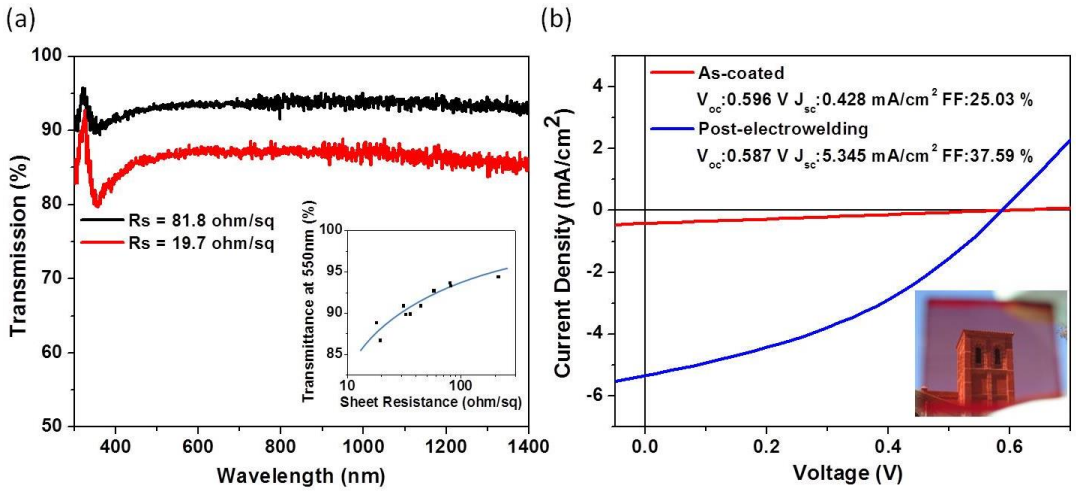

Figure 2.5 Optical properties and the application of electro-welding on temperature-sensitive materials and devices. (a) Transmission of treated silver nanowire films with different nanowire area densities. The inset shows the relationship between the transmission at 550 nm and electrowelded sheet resistance values with average nanowire dimensions of 90 nm in diameter and 40 μm in length. (b) Current density-voltage characterization of a semitransparent polymer solar cell made with an electrowelded silver nanowire film as the top electrode. The device using an untreated silver nanowire film (red curve) showed extremely high series resistance, and after the electrowelding treatment (blue curve) the series resistance was reduced significantly, indicating dramatically reduced sheet resistance in the silver nanowire film. The photovoltaic performance improves by a factor of 20 after the treatment. The inset is a picture of a semitransparent polymer solar cell.

2.4 Conclusions

In this chapter, we have demonstrated the use of localized reactions induced by electrical

current flow to improve the contact properties of metallic nanowire contacts dramatically. This process can be precisely controlled using a constant current power supply to achieve different sheet resistance levels within seconds. Joule heating will initially be generated at the high resistance contacts at the high current density region near the center of the wire/wire contact. The smaller diameter silver nanowire with a higher free energy will become unstable and diffuse onto the other wire to form reacted and eventually ripened contacts. Contact resistance was found to be reduced more than seven orders of magnitude after the treatment. More importantly, the presence of anisotropic electromigration effect was observed and resulted in further improvement of the morphology of the contact in bringing the contact resistance to lower values. This process demonstrated the capability of electrically controlling nanoscale interactions and introduced a new way to investigate nanowire contact reactions.

From a practical point of view, solution-based deposition and extremely fast post-treatments can facilitate the mass production of metallic nanowire network. As demonstrated on polymer solar cells, power loss in the top electrode can be significantly reduced and the power conversion efficiency improved by 20 times after the treatment. Unlike heat treatment on a hot plate, this process makes it possible to develop metallic nanowires as electrodes on temperature sensitive substrates with low energy consumption

and less damage. Additionally, this process will not suffer from shadowing effects, which can reduce process homogeneity over large areas in light or laser treatments. This development brings us one step closer to fast and cost effective solution-processed electrodes, devices, and circuits fabricated on a wide variety of substrates through electrically derived contact reaction of nanomaterials and heterojunction nanostructures fabrication.

Chapter 3 Transparent Conductors of Silver Nanowires Networks Composite

3.1 Introduction

Except for the great optical and electrical properties of silver nanowire networks, effective charge transport for solar cell devices needs to be improved. Furthermore, flexible transparent conductors processable under thermally and chemically benign conditions in vacuum environments are urgently needed to replace sputtered ITO thin films effectively for low-cost production and for emerging flexible electronics. Calculations predict that metal nanowire networks have the potential to demonstrate substantially higher transmittance than sputtered ITO thin films at equivalent sheet resistance values.[59] In this approach, the high optical transmittance of the networks that can be achieved is not from their intrinsic optical properties but from the relatively low surface coverage of the nanowires. Therefore, in order to achieve comparable sheet resistance to that of sputtered ITO thin films at equivalent transmittance, nanowire materials have to have much higher intrinsic electrical conductivity than that of conductive metal oxides. Lee *et al*. first demonstrated solution-processed randomly dispersed silver nanowire mesh as a promising candidate to replace sputtered ITO thin films by providing both low sheet resistance and

high transmittance.[59] In order for silver nanowire networks to be effectively incorporated into a wide range of modern optoelectronic devices, the following challenges must be simultaneously resolved: (1) wire-to-wire junction resistance; (2) surface roughness; (3) gaps between silver nanowires causing parasitic lateral current flow; (4) appropriate work function; (5) mechanical robustness including adhesion and flexibility; and (6) process compatibility.[9]

In addition, poor thermal and chemical stabilities of these metallic nanowires were observed, however, restricting the capability of post-processing and potential applications. The instabilities of the metallic nanowire network mainly come from the chemical reaction (including oxidation, sulfurization) and surface diffusion of metal atoms resulting in contact ripening or Rayleigh effect.[82-84] In particular, ripening at the contacts of the nanowire network causes a discontinuous network, which results in a decreased lifetime and limits post-processing. Some approaches on improving the thermal and chemical stabilities of the nanowire network were proposed using functional protection layers deposited by vacuum techniques such as atomic layer deposition and sputtering,[85-87] which, although effective, led to increased manufacturing cost.

In this work, we attempt to resolve nearly all of the current issues imposed on silver nanowire networks by two different strategies: a) employing solution-deposited conductive

metal oxide nanoparticles onto pre-existing silver nanowire network. The embedding the silver nanowire network in the conductive metal oxide nanoparticle matrix offers many advantages including improved wire-to-wire junction conductance, improved surface morphology, excellent mechanical adhesion, and flexibility. As the first demonstration of this method, indium tin oxide nanoparticles (ITO-NP) were selected as a conductive metal oxide nanoparticle because of their relatively maturity and industrial availability. Although our present electrode design contains indium, which is of concern in terms of supply and price, we expect that indium-free conductive metal oxide nanoparticles such as aluminum doped zinc oxide and antimony-doped tin oxide nanoparticles may play equivalent roles to ITO-NP in the future electrode architecture; b) employing a sol-gel method using titanium oxide (TiO_X) as a highly efficient protecting layer over the silver nanowire networks. The sol-gel TiO_X film has found widespread application in areas such as antireflection coating,[88] wear resistance,[89] and chemically resistant coatings.[90] The sol-gel solution process is inexpensive and easily adaptable for industrial mass production. The process can be done in atmospheric conditions and the properties of the coatings can be precisely controlled by tuning the temperature, chemical contents, and molar ratios of the precursors. Moreover, a variety of methods are available for depositing these coatings, such as spin-coating, dipping coating, spray coating, and blade coating. In this work, it is found

that by applying sol-gel TiO_X onto the silver nanowire network, the composite electrode showed improved electrical and optical properties, superior perforamnce in thermal accelerated life tests, bending test, chemical corrosion test, and exhibited better adhesion with the substrates. It is believe that these electrode designs will allow silver nanowire films to be practically employed a wide range of optoelectronic device applications.

3.2 Experimental Details

3.2.1 Preparation of Silver Nanowire-Nanoparticle Composite

Silver nanowire dispersions were spun at spin speed of 1000 rpm for 60 s onto Polyethylene terephthalate (PET) substrates to form randomly dispersed silver nanowire network, and ITO-NP films solution sequentially spun at spin speed of 2000 rpm for 30 s onto the silver nanowire network. The silver nanowire solutions were purchased from Seashell Technologies and diluted to 1 mg/mL concentration. The diameter and length of the silver nanowire approximately have 120 nm of diameter and 30 um of length, respectively. Silver nanowire network with different sheet resistance and optical transmittance values were obtained by repeated spin-coating process. The employed ITO-NP solutions are prepared by mixing 30 wt% of ITO-NPs dispersed in isopropyl alcohol (Sigma Aldrich) with Polyvinyl Alcohol dissolved in deionized water. The PVA solution was added to into the

ITO-NP solution to further improve mechanical adhesion of the resulting silver nanowire/ITO-NP films.[68]

3.2.2 Preparation of Silver Nanowire-Sol-Gel TiO_x Composite

Silver nanowires were obtained from Blue Nano Inc with an averaged diameter of around 90 nm and an averaged length of around 30 μm. Titanium isopropoxide ($Ti\{OCH(CH_3)_2\}_4$, TTIP) and ethanolamine were purchased from Sigma Aldrich Inc. Diluted silver nanowire (2.5 mg/mL) dispersed in ethanol was spun onto the pre-cleaned rigid glass substrates as well as PET flexible substrates (3M Transparency Film, 3M). Diluted silver nanowire dispersion was spun onto the targeting substrate with a 2000 rpm spin speed. Different silver nanowire densities are prepared by multiple spin coating cycles. Diluted TTIP solution with ethanol and ethanolamine (volume ratio 1:10:0.1, no aging is required.) was spun onto the silver nanowire network with 2000 rpm for 40 seconds. The films were baked at 80 °C for 5 mins to remove the residual solvent. The ITO films were deposited by sputtering with a 150 nm thickness under $2x10^{-5}$ torr.

3.2.3 Characterization of Thin Film Composites

Optical specular transmittance of the films was measured using a Hitachi Ultraviolet–Visible Spectrophotometer (U-4100) without an integrating sphere. The measured

transmittance values exclude scattered light and Fresnel reflection. A glass substrate was used as a reference in the transmittance measurement. The surface resistance (<100 ohm/sq) was measured using a four-point probe method with a surface resistivity meter (Guardian Guardian Manufacturing, Model: SRM-232-100, range: 0~100 ohm/sq). Two-point probe method was used to estimate the surface resistance of the film with surface resistance >100 ohm/sq. Thin film transistors were measured by a semiconductor parameter analyzer (Agilent 4155C, Agilent Technologies) connected to a probe station. Cross-section and plane view SEM images were taken on a JEOL JSM-6700F electron microscope.

3.3 Results and Discussion

3.3.1 Silver Nanowire-Nanoparticle Composite

Microstructure. The surface morphology of a metal nanowire network is critically important to its successful incorporation into optoelectronic devices. The nature of randomly dispersed metal nanowire network lead to protrusions produced by overlapping wires which were as approximately three times high as the diameter (~110 nm) of the employed nanowires (Figure 3.1a and c). This surface morphology would not be suitable to modern thin film optoelectronic devices fabrication wherein the thickness of each layer is frequently less than 100 nm. This rough surface could frequently cause the device short

failure.[66] The subsequent deposition of ITO-NP film significantly improved the resulting surface roughness. The pre-deposited nanowire mesh was completely covered by ITO nanoparticles without leaving any gaps or space. As a result, the nanowires cannot be seen in the plane view SEM image (Figure 3.1b). The localized height variation of the resulting film was the same order of magnitude as the size (10–30 nm) of the employed nanoparticles, as shown in the AFM scan (Figure 3.2). The root mean square roughness and roughness average were 12.7 nm and 15.7 nm, respectively. These values are approximately one tenth of the local height variation of bare silver nanowire films which can be 200–300 nm due to stacked wires in their junctions. It is expected that the surface roughness can be further improved by employing smaller sized nanoparticles.

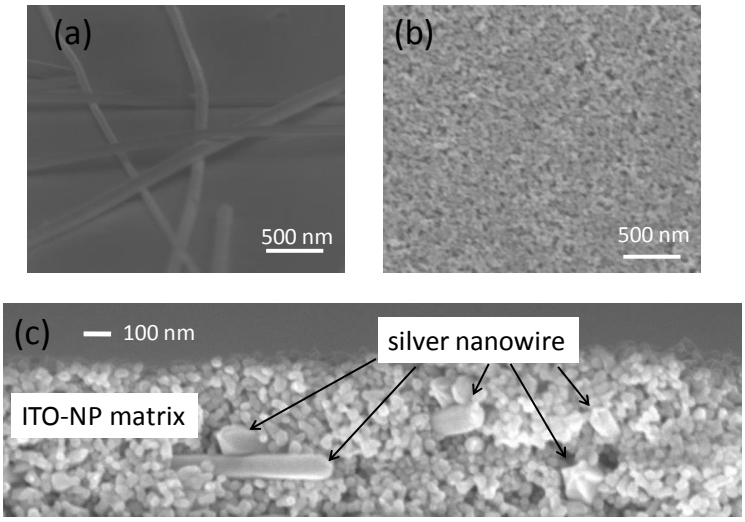

Figure 3.1 (a) Tilted (75°) view SEM images of a bare silver nanowire network. (b) Plain view SEM images of an indium tin oxide nanoparticle film deposited on pre-existing silver nanowire network. (c) Cross sectional SEM image of silver nanowire network embedded in an indium tin oxide nanoparticle matrix.

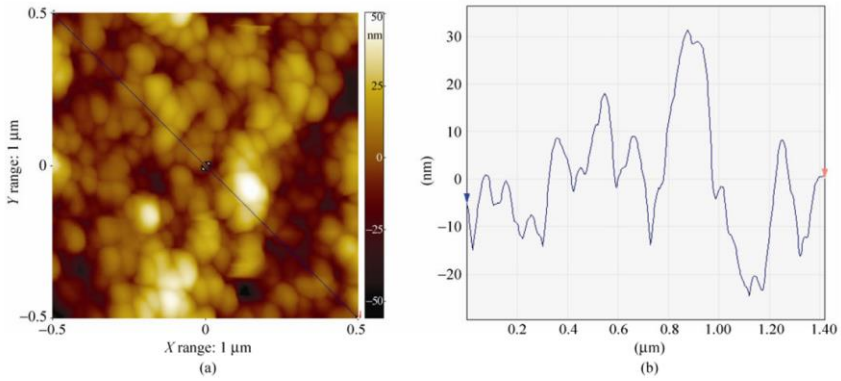

Figure 3.2 (a) AFM image of the silver nanowire/ITO-NP surface and (b) AFM height line profile of the surface.

The large lateral holes between silver nanowires are also seriously problematic in the lateral carrier collection of devices in which carrier diffusion length is not much larger than the gap size. This charge collection issue can be also solved owing to completely

filling the holes present in the nanowire networks by transparent conductive material in optoelectronic devices.[61] Furthermore, the resulting surface of silver nanowire/ITO-NP will be favorable for building opto-electronic devices because most conventional thin film optoelectronic materials are optimized to be compatible with the electronic properties of the ITO surface.

Optoelectrical properties. The sheet resistance of silver nanowire networks depends on the dimension (length and diameter) of the wires, wire areal density, each wire resistance, and wire-to-wire contact resistance. At the given dimension of the wires and wire areal density, wire-to-wire junction resistance rather limits overall the sheet resistance due to its

extremely high value, typically larger than 10^9 ohm, in as-prepared silver nanowire networks.[66] It is thus critically important to ensure low wire-to-wire junction resistance. The possible existence of small vertical gaps between silver nanowires and insulating ligands used for synthesis and solution dispersion is likely to hinder carrier transport across the wire-to-wire junction. Although fused wire-to-wire junction can be readily achieved by thermal annealing around 180 ^oC or mechanical pressing, these methods may not be applicable on heat sensitive and/or readily deformable materials and devices.

The deposition of an ITO-NP matrix onto a bare silver nanowire network dramatically decreased the sheet resistance of the films (Figure 3.3a). The sheet resistances of silver nanowire/ITO-NP films ranged from 0.01% to 18.9% of those of bare silver nanowire films, depending on the wire number density with a range of 0.3–1.6 μm^{-1} in the films (Figure 3.3b). The meshes with smaller number density showed more significant decrease in sheet resistance. The decrease in sheet resistance cannot be explained by conduction taking place predominantly in the ITO nanoparticles because the sheet resistance of the plain ITO-NP film was as high as ~20 kohm/sq. Based on the observation that there was no obvious change of shape in the pre-deposited nanowire network after deposition of the ITO-NP matrix, these results thus verify the reduced wire-to-wire junction resistance after deposition of the conductive nanoparticle matrix

The bare silver nanowire meshes with smaller wire number density have been shown to have larger average wire-to-wire junction resistance which implies that the junction resistance is a more dominant component in the sheet resistance of the films with smaller wire number density.[59] Thus, a more dramatic decrease in the sheet resistance of the films with smaller wire number density was observed because low wire-to-wire junction resistance was achieved in the all prepared networks by sequential deposition of the ITO-NP matrix.

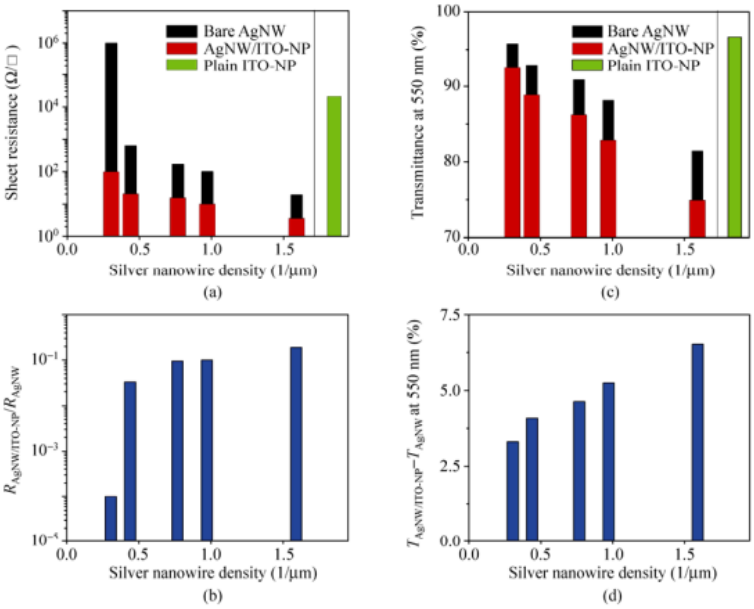

Figure 3.3 (a) Sheet resistance values of a plain indium tin oxide nanoparticle film and a number of silver nanowire networks before and after nanoparticle matrix deposition. (b) Ratios between the sheet resistance value of silver nanowire networks before and after the deposition of the indium tin oxide nanoparticle matrix. (c) Optical transmittance at 550 nm of a plain indium tin oxide nanoparticle film and a number of silver nanowire networks before and after the deposition of the indium tin oxide nanoparticle matrix. (d) Difference in the transmittance at 550 nm of the silver nanowire networks before and after deposition of the indium tin oxide nanoparticle matrix

The microstructure of the deposited silver nanowire/ITO-NP films supports the argument for improved wire-to-wire junction conductance. A cross-sectional SEM image shows that each silver nanowire is surrounded by densely packed ITO nanoparticles (Figure 3.1c). The smaller size of the individual ITO nanoparticles relative to the dimensions of the silver nanowires likely allows them to readily pack into the gaps left in the as-deposited mesh. The reduction of wire-to-wire contact resistance can thus be attributed to the conductive ITO nanoparticles filling the vertical gaps which allows the wires to become connected together via a conductive medium. Free electrons are then able to flow across wire-to-wire junction without undergoing significant electrical resistance.

High optical transmittance is as important as low sheet resistance in transparent conductors. The transmittance of the silver nanowire films was only slightly decreased by 3.3% to 6.5% after ITO-NP matrix deposition, depending on wire number density in the range 0.3–1.6 μm^{-1} (Figure 3.3c and d) while a significant decrease was simultaneously observed in the sheet resistance of the films. The films with higher wire number density showed more transmittance loss after deposition of the ITO-NP matrix. Considering ITO-NP films showed a transmittance of 96.7% at 550 nm, and the measured specular transmittance excluded scattered light, it is likely that the optical transmittance losses of more than 3.3% after deposition of the ITO-NP film onto existing silver nanowire films is associated with

the enhanced light scattering in the silver nanowire/ITO-NP. The enhanced scattered light could be advantageous for thin film photovoltaic devices by providing better absorption of light in absorber layers and better photogenerated carrier collection. The enhanced light scattering by silver nanowire based electrodes has been reported to improve the short circuit current density in organic and inorganic thin film solar cells.[59, 61] Organic solar cells would perhaps be expected to benefit most from this effect. These organic devices are often unable to completely absorb light because their absorber layer thickness is typically limited by short carrier diffusion lengths. Enhanced light scattering could be also useful to reduce the thickness of absorber layers in chalcogenides and polycrystalline or amorphous silicon solar cells.

The transmittance values of silver nanowire/ITO-NP films with several different sheet resistance values are shown in Figure 3.4a. The transmittance at 550 nm reached 90.5% when the sheet resistance was 44 ohm/sq; 88.6% at 23 ohm/sq, and 85.3% at 11 ohm/sq. The transmittance of the films was essentially constant across all measured wave- length regions because optical transmittance in metal nanowire films is controlled almost entirely by the sparseness of the metal wire network. Our low temperature solution-deposited silver nanowire networks embedded in ITO-NP matrices showed sheet resistance and transmittance values comparable to commercially available sputtered-deposited ITO

electrodes as well as the reported values for silver nanowire networks and silver nanowire composites.[65-67, 69, 80, 91-93] (Figure 3.4b)

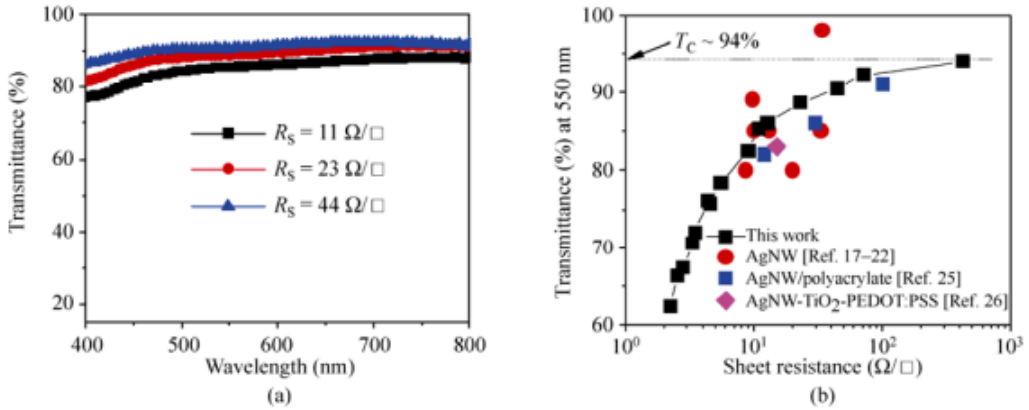

Figure 3.4 (a) Variation in transmittance of the silver nanowire/ITO-NP films with wavelength for three different sheet resistance values. (b) Plot of transmittance versus sheet resistance, the maximum achievable transmittance of conductive silver nanowire/ITO-NP films, and the literature values for silver nanowire and silver nanowire composites

Percolation in Silver Nanowire/ITO-NP films. Predicting the relationship between transmittance and sheet resistance will be useful because these two parameters are perhaps the most important properties in the selection of effective transparent conductors. Percolation theory for randomly dispersed one-dimensional objects predicts the relationship between the sheet resistance and the wire areal number density as below:[57]

$$\frac{1}{R_S} \propto (N - N_c)^{\alpha} \; and \; N_c = 17.94/\pi L^2 \quad (1)$$

Where R_S is the sheet resistance of the networks, N is the wire areal number density dispersed on the surface, N_C is wire areal number density at the threshold point,

L is the wire length, and α is an exponent depending on the dimension of the resulting meshes.

To relate the sheet resistance to the transmittance from the above percolation theory, we need the relationship between the transmittance and the wire areal number density. The surface coverage (SC) will be the average projected area of wires (LD) multiplied by the wire areal number density (N) as below:

$$SC_C = N \times LD \quad (2)$$

Where D is the diameter of the metal wires. The transmittance loss in metal nanowire networks is mainly due to the reflective scattering of light by the metal nanowires. The loss of optical transmittance of the bare silver nanowire will be thus approximately equal to the surface coverage of the metal nanowires, and the transmittance can be described as below:

$$T = 100 \times (1 - SC)\% = 100 \times (1 - LDN) \quad (3)$$

At the percolation point

$$SC_C = N_C \times LD = \frac{17.94LD}{\pi L^2} = 5.71D/L \quad (4)$$

$$T_c = 100 \times (1 - 5.71D/L)\% \quad (4)$$

Thus, the transmittance at the percolation point, T_C, equivalent to achievable maximum transmittance of a conductive network, is solely determined by the aspect ratio of the wires while the critical wire areal number density is solely determined by the length of wires.

The nanowires employed in this work have approximate diameters of 115 nm and lengths of around 30 μm. The T_C value is thus estimated to be approximately 97.8%.

To validate our assumption that the loss of optical transmittance of silver nanowrie networks is approximately equal to the surface coverage of the metal nanowires, we plotted the variation in transmittance loss (100–T) (%) for the silver nanowrie networks as a function of the surface coverage of silver nanowires both before and after ITO-NP deposition. Figure 3.5a–e show plane view SEM images of bare silver nanowrie films with different number densities of silver nanowires with values ranging from 0.305 to 1.59 μm^{-1}. The surface coverage is estimated by multiplying the diameter (115 nm) of the wires and the wire number density measured from the SEM images of the silver nanowrie networks before the ITO-NP deposition. The surface coverage is nearly equal to the transmittance loss of the bare silver nanowrie, which validates our assumption (Figure 3.5f). The maximum transmittance of the transparent silver nanowrie/ITO-NP was determined to be 94% from the plot of the sheet resistance versus the transmittance (Figure 3.4b) which is 3.8% lower than the calculated value of 97.8%. This difference results from additional transmittance loss by large angle light scattering and light absorption by the ITO-NP matrix.

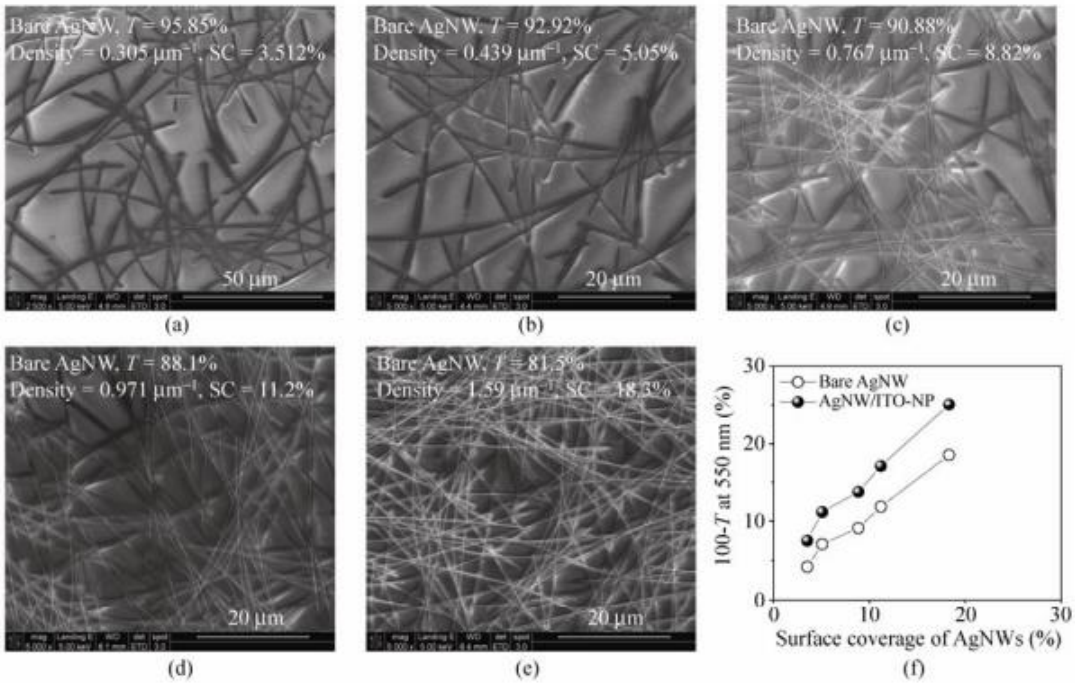

Figure 3.5 Plane view SEM images of bare silver nanowrie networks with a nanowire density of (a) 0.305 μm^{-1}, (b) 0.439 μm^{-1}, (c) 0.767 μm^{-1}, (d) 0.972 μm^{-1}, (e) 1.59 μm^{-1}. (f) Optical transmission loss (100–T) of bare silver nanowrie and silver nanowrie/ITO-NP films as a function of the surface coverage of silver nanowires

By combining equations (1)–(4), the variation in sheet resistance, R_S as a function of optical transmittance, T, can be described by the equation

$$1/R_s \propto (T_c - T)^{\alpha} \quad (5)$$

The linear plot of log (R_S) vs. log (T_C–T) allows us to extract α values of 1.46 and 1.27 at 550 nm and 600 nm, respectively (Figure 3.6). These values are similar to the theoretical value of α = 1.33 for the relationship between nanowire number density and surface conductance in two-dimensional networks,[57] and also similar to the reported values of

1.42 experimentally determined from the relationship between amount of nanowire deposited on the substrate surface and the surface conductance of nanowire films.[67]

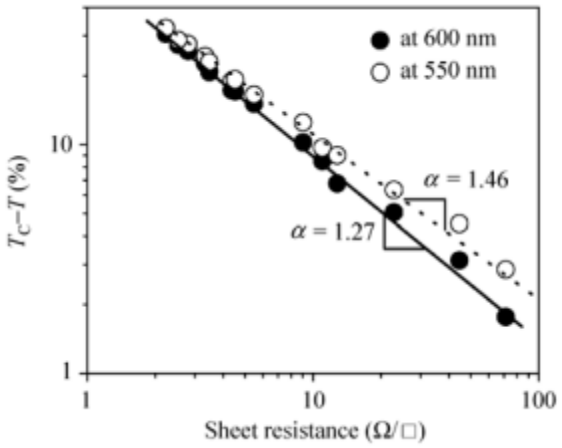

Figure 3.6 The linear plot of log (R_S) vs log (T_C–T) allows us to extract α values of 1.46 and 1.27 at 550 nm and 600 nm, respectively, from the equation: $1/R_s \propto (T_c - T)^{\alpha}$

Mechanical properties of Silver nanowire/ITO-NP films. In order for a potential electrode material to be used in flexible devices and to be compatible with roll to roll processing, the electrode must meet certain mechanical requirements including adhesion and flexibility. Tape tests were executed in the regions shown by the dotted lines in Figure 3.7 to test the adhesion of the silver nanowire film to the substrate. 3M tape (Scotch® Magic™ Tape) was pressed with a pressure of an approximately 2 MPa for 30 s. As described in the experimental section, we mixed a PVA solution with the as-purchased ITO-NP solution to prepare the final ITO-NP solution in order to achieve improved film adhesion. The addition of the PVA dramatically improved the film adhesion without

sacrificing transmission or sheet resistance. While bare silver nanowire films were completely peeled off during the tape test, the nanocomposite remained on the substrate without any change in transmittance or sheet resistance, demonstrating the excellent mechanical adhesion of the silver nanowire/ITO-NP film. In addition to mechanical adhesion, the silver nanowire/ITO-NP offers excellent mechanical flexibility even under severe concave and convex bending (Figure 3.8a). The surface resistance of the silver nanowire/ITO-NP film was observed to change by approximately 30% of its initial value when the film was bent to a 0.5 cm radius of curvature. For convex (concave) bending, the surface resistance of the film decreased (increased) with decreasing radius of curvature. It is likely that convex bending of the substrate induces compressive forces at the wire-to-wire junction, which in turn may improve the wire-to-wire junction conductance. This indicates that silver nanowire networks embedded in ITO-NP matrices have further room for improvement. More importantly, the resistance completely recovered its original value when the substrate was relaxed to back to a planar shape even after as many as one hundred bending cycles to a radius of curvature of 0.5 cm (Figure 3.8b). This recovery is attributed to the flexible nanoparticle matrix firmly holding nanowire network in place, which prevents the permanent deformation of the networks.

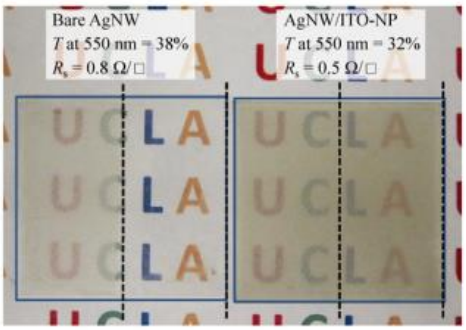

Figure 3.7 Photos of bare silver nanowire and silver nanowire/ITO-NP films after tape tests. The tape test was executed for the regions shown by the dotted lines in the photos to test the adhesion of the silver nanowire film to the substrate.

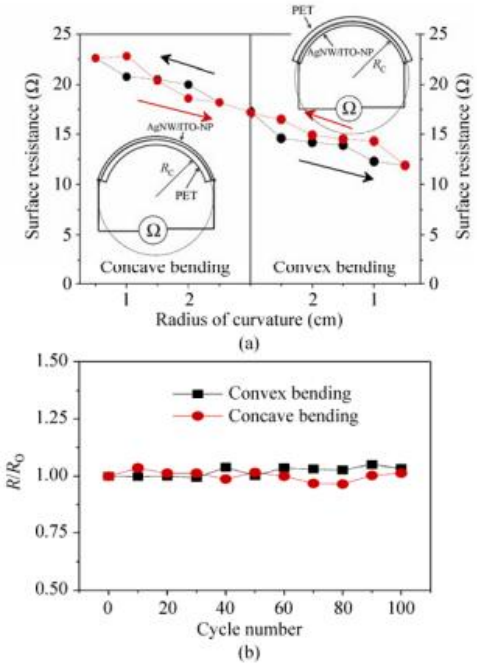

Figure 3.8 (a) Variation in the surface resistance of the silver nanowire/ITO-NP film deposited on a PET substrate as a function of radius of curvatures (R_C) in concave and convex bending. (b) Variations in the final surface resistance of a silver nanowire film as a function of number of cycles of bending to a 0.5 cm radius of curvature in concave and convex bending. The resistance values were measured after the substrate was relaxed to back to planar shape.

3.3.2 Silver Nanowire-Sol-Gel TiO_X Composite

Diluted silver nanowire dispersion was spun onto the target substrate and the result is shown in the SEM image in Figure 3.9a. The titanium isopropoxide ($Ti\{OCH(CH_3)_2\}_4$, TTIP) was diluted with ethanol and a small amount of ethanolamine, and then spun onto the silver nanowire network. The ethanolamine was added to stablize the sol preventing it from forming crystalline precipitations. The silver nanowire-sol-gel TiO_X composite film was shown with tilted angle SEM in Figure 3.9b. The details of the experiment were described in the experimental section. The sol-gel TiO_X layer exhibited a conformal coverage over the entire silver nanowire network and showed an amorphous phase due to the room temperature process.[94] The transmittance and sheet resistance of silver nanowire-sol-gel TiO_X film are 85.6% at a wavelength of 550 nm and 13.2 ohm/sq, which are superior to the previous report with a 84% trasmittance and a 19 ohm/sq sheet resistance using similar aspect ratio silver nanowires (averaged diameter of 90 nm and averaged length 30 μm) , as shown in Figure 3.9c and d. [69, 80, 84] Although the transmittance was slightly affected by the sol-gel TiO_X layer, which has a 99.3% trasmission at the wavelength of 550 nm with glass as reference, it is found that the sheet resistance was reduced significantly after the sol-gel TiO_X layer deposition even without heat treatment (Figure 3.9e). The reduction of the sheet resistance in silver nanowire-sol-gel TiO_X could be

originated from the improved contacts between adjancent silver nanowires during the evaporation of the solvent and the transformation between TTIP and TiO_X network during the drying process.[95] The shrinking force from the gelation process was presumed to be the main reason for the sheet resistance reduction, because the sol-gel TiO_X layer has a near insulator property hardly contributing to the conductive pathways within silver nanowire network.

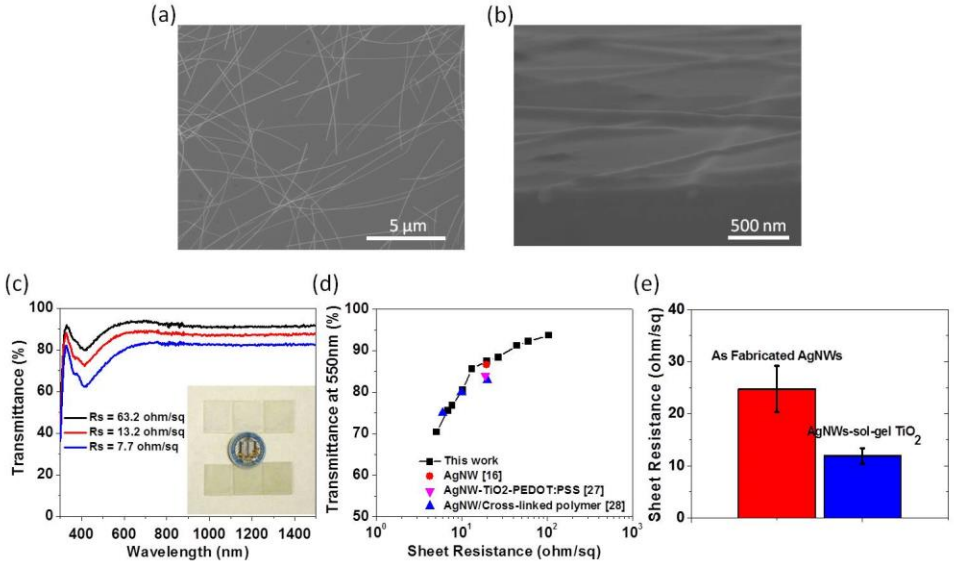

Figure 3.9 (a) Plain view SEM image of the silver nanowire network and the averaged diameter and length are around 90 nm and 40 µm respectively. (b) Tilted angle SEM of silver nanowire network covered with sol-gel TiO_X which shows a uniform coverage. (c) The transmittance of the silver nanowire-sol-gel TiO_X films over three different sheet resistance values from different silver nanowire density. The inset shows the optical image of different transmittance films by tuning the silver nanowire density. (d) Transmittance versus the sheet resistance of silver nanowire-sol-gel TiO_X films and literature values of silver nanowire and silver nanowire composites from similar diameter and length of silver nanowires. (e) Sheet resistance change before and after sol-gel TiO_X coating. After sol-gel deposition, averaged sheet resistance of 24 ohm/sq for the as-fabricated silver nanowire network reduced to an averaged sheet resistance of 11 ohm/sq.

Thermal accelerated life test was done in air under different temperatures with one hour treatment time, as shown in Figure 3.10. Bare silver nanowire networks, silver nanowire networks incorporated with metal oxide nanoparticles as the functional protecting material were fabricated and tested in comparison with the sol-gel TiO_X process.[96-98] The sheet resistance of the as fabricated silver nanowire networks was fixed around 20 ohm/sq while extra coatings with nanoparticles and sol-gel TiO_X would reduce the sheet resistance to around 11 ohm/sq as shown in Figure 3.9e.[68] No significant changes in the electrical properties was observed for any one of the three cases during the thermal accelerated life test at 200 °C as shown in Figure 3.10a. However, when tested at 250 °C, the sheet resistance of the bare silver nanowire film increased rapidly up to values beyond our measurement capacity of 120 Mohm/sq. When the bare silver nanowire film was treated at 300 °C, the conductive pathways within the network was disconnected within 5 mins as shown in Figure 2b. Some of the nanowires within the bare silver nanowire network became small droplets due to contact ripening and Rayleigh instability.[99] Meanwhile, the silver nanowire-sol-gel TiO_2 composite film remained intact after 10 minutes of 300 °C treatment (Figure 3.10c). For the silver nanowire/ITO-NP composite, the ITO-NPs provided partial protection to the silver nanowire network as well as acting as the conductive matrix to the film. The sheet resistance of silver nanowire/ITO-NP composite

increased slower than the bare silver nanowire network, and saturated to around 10^4 ohm/sq due to the coductive marix of ITO-NPs under 300 °C treatment.[61] When the temperature was increased to 350 °C, the sheet resistance of the silver nanowire-sol-gel TiO_X composite rose gradually to over 120 Mohm/sq in around one hour. Results from higher temperatures (375 °C and 400 °C) are shown in Figure S3.1 and it is clearly shown that the silver nanowire-sol-gel TiO_X composite maintained its conductive path and sheet resistance value for more than 5 mins under 400 °C. These results demontrated that the thermal stability of the silver nanowire network was significantly improved with the incorporation of sol-gel TiO_X. Previously it has been reported that by adopting a core-shell silver nanowire/TiO_X structure, the single silver nanowire can be stable up to 750 °C in 10 mins under ultra high vaccuum.[86] In a nanowire network, however, low surface energy grooves are formed at the contacts between wires and these could facilite the movement of Ag atoms to the contact through surface and bulk diffusion, causing contact ripening and Rayleigh effect to happen at a lower temperature or shorter treatment time. Conformal coating using sol-gel TiO_X layer over the silver nanowire network can effectively suppress the surface diffusion and enhance the thermal stability of the network compared with bare silver nanowire and NP coated composite silver nanowire networks.

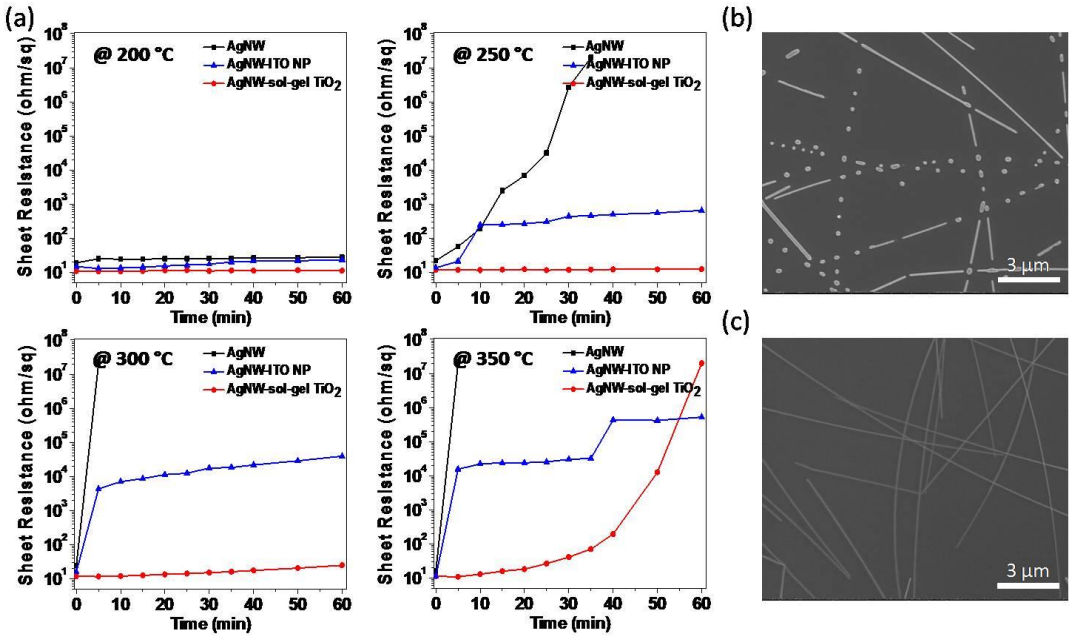

Figure 3.10 (a) The sheet resistance versus time was recorded under different temperature treatments for bare silver nanowire networks and two different silver nanowire composite films, representing unprotected (silver nanowire), partially protected (silver nanowire/ITO-NP) and fully protected (silver nanowire-sol-gel TiO_X) silver nanowire networks. (b) Plane view SEM images of the bare silver nanowire network treated at 300 °C for 5 mins and (c) silver nanowire-sol-gel TiO_X film treated at 300 °C for 10 mins.

Chemical stability of the silver nanowire-sol-gel TiO_X composite electrode was examined through corrosion test comparing these silver nanowire composite films and bare silver nanowire network. Silver is stable in most chemical environments but it can easily react with sulfur to form Ag_2S which is black in color. In this case, sulfur was provided dissolved in the solvent dimethylformamide (DMF) and applied to silver nanowire networks with and without functional protecting layers. The silver nanowire films were soaked into 60 ml of DMF solvent containing 0.008 g of sulfur powders for 30 mins. Higher chemical

stability was observed for the silver nanowire-sol-gel TiO_X composite electrode compared with the bare silver nanowire network and NP coated silver nanowire network, as shown in Figure 3.11. As shown in Figure 3a, the resistance of the bare silver nanowire network rose more than six orders of magnitude of its initial resistance value after the 30 min treatment. The resistance rose around three orders of magnitude for the silver nanowire/NP composite film and the resistance change in both cases could be attributed to the reaction of Ag with sulfur ion decreasing the amount of the silver nanowires present for creating conductive pathways within the silver nanowire network. The silver nanowire-sol-gel TiO_X composite film was slightly affected and the resistance rose to twice its original value. For the bare silver nanowire case, although the silver nanowires kept their original shapes but Energy Dispersive X-ray Spectroscopy (EDS) showed a Ag to S atomic ratio of 2:1. This is a clear indication that most of the silver nanowires were corroded by the sulfur ions. Meanwhile, the sol-gel TiO_X covered silver nanowire network remained intact as observed by SEM and sulfur was not detected by EDS analysis, as shown in Figure 3.11b and c. The three types of silver nanowire networks investigated behaved differently when placed in a chemical environment containing sulfur and a schematic diagram was shown in Figure 3.11d. The exposed surface area of the silver nanowires determine the reaction rate between silver atoms and sulfur ions, making bare silver nanowires most prone to chemical

corrosion. The NPs in the silver nanowire/NP composite electrode could provide partial protection for the silver nanowires, however sulfur ions could still penetrate the nanoporous structure and react with the Ag atoms, although at a slower rate compared to the bare silver nanowire case. The sol-gel layer offered the best corrosion resistance due to its full coverage of the silver nanowire network and choosing TiO_X as opposed to other metal oxides such as zinc oxide can provide the additional benefit of being resistant to most base and acid solutions, thereby providing a more chemically stable protection.

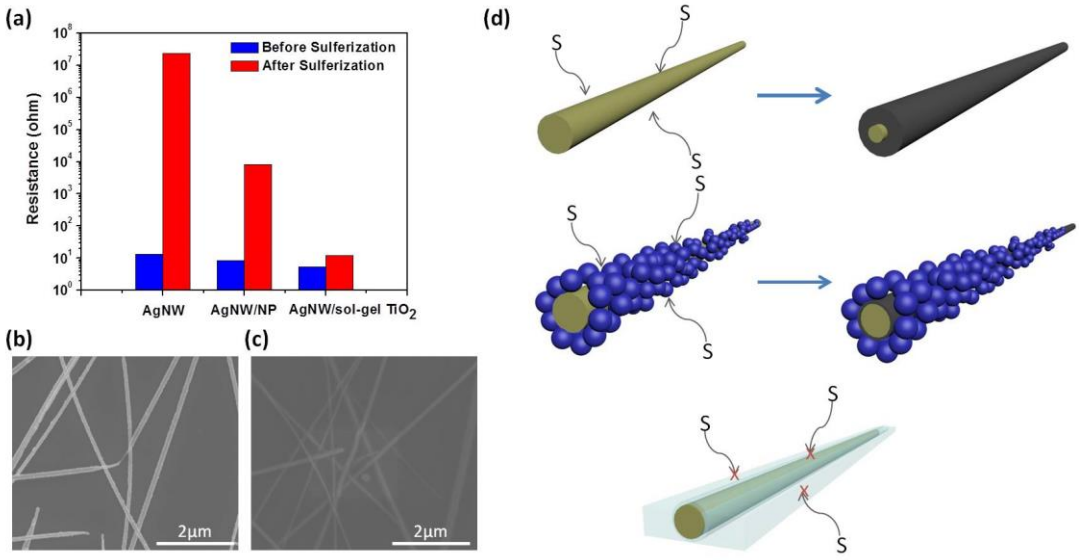

Figure 3.11 Corrosion test to silver nanowire and silver nanowire composite films soaked in the DMF-Sulfur power for 30 mins. (a) the resistances changed before and after the sulfurization. (b,c) SEM images of the bare silver nanowire network and silver nanowire-sol-gel TiO_X composite film after sulfurization. (d) the schematic diagrams of the protection mechanism for different cases.

Mechanical properties including the adhesion to substrates and flexibility are probed to test

this method's compatibility with electronic device fabrication and roll-to-roll processing. The adhesion property was tested by peeling with scotch tape and the resistance of the silver nanowire films were recorded before and after the taping process (Fig. 3.12a and b). The samples shown on the top of Figure 3.12a were bare silver nanowire network film, with a sheet resistance of 4.6 ohm/sq and trasmittance of 52.1% at the wavelength of 550 nm.The silver nanowire-sol-gel TiO_X composite had a sheet resistance and trasnsmittance of 3.6 ohm/sq and 49.3% repectively. After peel-off test using the scotch tape, the sheet resistance of silver nanowire-sol-gel TiO_X did not change. The sheet resistance of the bare silver nanowire network, however, increased to a value that is beyond our measurement capacity (120 Mohm/sq) due to the weak adhesion between the glass substrate and the silver nanowire network as shown in Figure 3.12b. Furthermore, the flexibility of the silver nanowire-sol-gel TiO_X composite was evaluated through a bending test as shown in the Figure 3.12c. To compare the silver nanowire-sol-gel TiO_X composite film with the standard sputtered ITO electrode, both films were prepared on PET substrates. Five hundred bending cycles with a 1 cm diameter bending curvature was applied on both films and the sheet resistance changes were recorded. The sheet resistance of the sputtered ITO rapidly increased for even below 100 cycles due to crack formation within the ITO film.[100] The sheet resistance of the silver nanowire-sol-gel TiO_X composite film, on the

other hand, was maintained after 500 cycles.

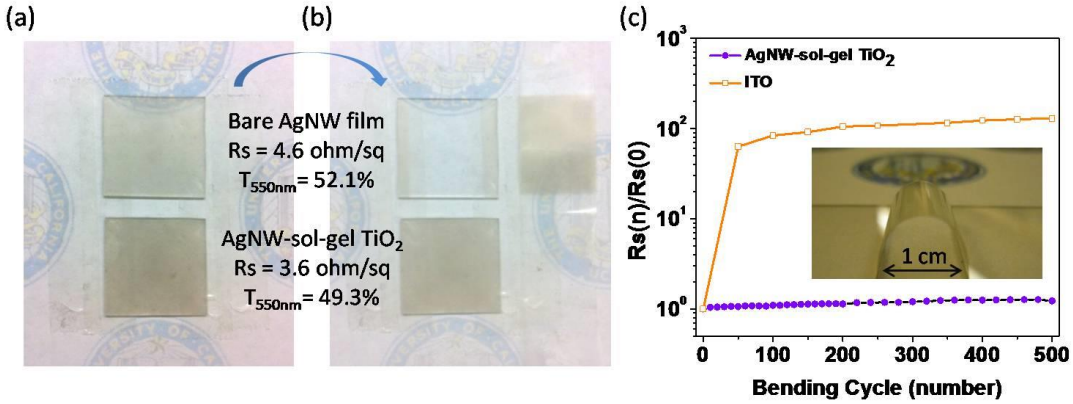

Figure 3.12 Photos of bare silver nanowire (top) films and silver nanowire-sol-gel TiO_X (bottom) before (a) and after tape test (b). The sheet resistance of the bare silver nanowire films is 4.6 ohm/sq and the silver nanowire-sol-gel TiO_X is 3.6 ohm/sq. After adhesion test, the silver nanowire sol-gel TiO_2 remains conductive and the bare silver nanowire doesn't. The scotch tape was placed on the right hand side of the samples in (b). (c) Variations in the sheet resistance of silver nanowire-sol-gel TiO_X and sputtered ITO film on PET substrates as a function of number of cycles of bending to a 0.5 cm radius curvature. The sheet resistance values were measured after the substrate was relaxed back to planar shape.

Silver nanowire-sol-gel TiO_X composite was incorporated into TFT devices as the S/D electrodes to explore its feasibility as a practical electrode. The 50 nm-thick ZnO channel material was sputtered onto the p+ doped Si wafer with a thermally grown SiO_2 (300 nm), and S/D electrodes were deposited by spray-coating diluted silver nanowires and TTIP precursor solutions through shadow masks on top of the ZnO layer. A schematic structure of the device is shown in Figure 3.13a. A photo of the TFTs was shown in Figure 3.13b with the inset showing an optical image of one of the device and the channel length and

width were measured to be 90 μm and 820 μm, respectively. Typical output curves of drain current (I_{DS}) as a function of drain voltage (V_{DS}) under various applied gate voltage (V_{GS}) before and after thermal treatment were plotted in Figure 3.13c, and d. In Figure 3.13c, a nonlinear rise of drain current at low drain voltage indicated that the source-drain contact resistance was limiting the drain current,[101] which was not observed with sputtered ITO electrodes. The silver nanowire-sol-gel TiO_X electrodes did not form a good electrical contact with the ZnO channel layer initially, however after post-annealing under 300 °C for 10 mins in air, the contact of the silver nanowire-sol-gel TiO_X with the ZnO channel layer was improved and the current−voltage curve showed typical transistor behavior with a linear I_D-V_D dependence at low bias and saturated as the channel layer was pinched off, as shown in Figure 3.13d. Meanwhile, the post-annealing could enhance the TFT performance by increasing the crystallinity of ZnO layer and the reduction of specific contact resistance.[102] A transfer curve of ZnO TFTs with silver nanowire-sol-gel TiO_X S/D was shown in Figure 3.13e, with an on-off ratio of 5 x 10^6. The field-effect mobility (μ_{Fe}) of the TFT was 0.77 cm^2/V-s. Thus silver nanowire-sol-gel TiO_X electrodes showed a better compatibility to TFT application compared with bare silver nanowire film by improving the thermal stability and electrode lifetime of the devices.

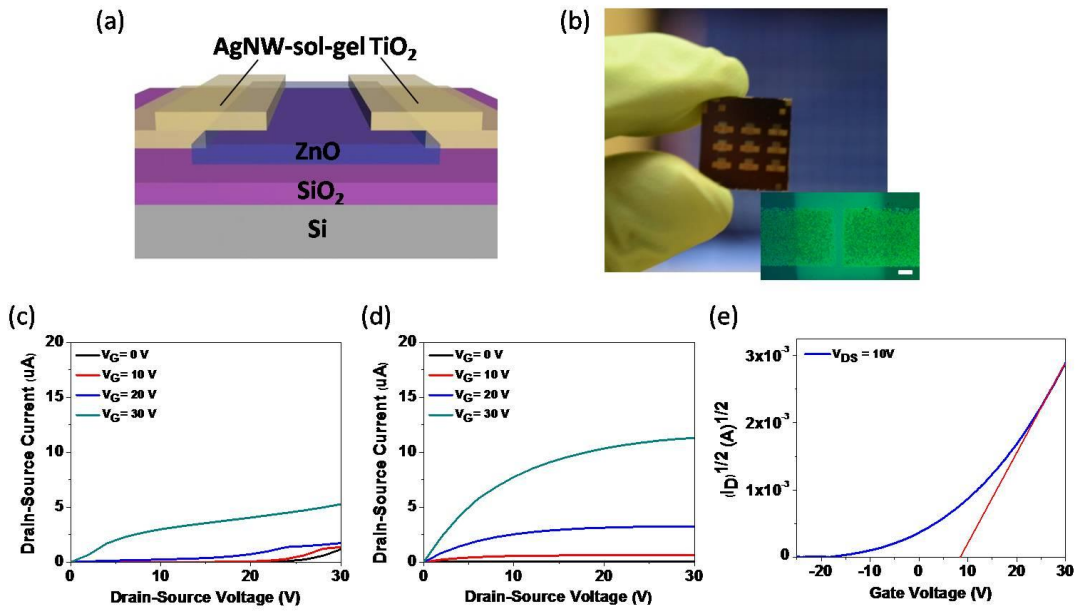

Figure 3.13 (a) Schematic diagram of the silver nanowire-sol-gel TiO_X electrode TFT structure and (b) optical images of the TFT devices. The scale bar is 100 μm. (c) The I_D-V_D curve of the TFT device with as-fabricated silver nanowire-sol-gel TiO_X electrodes and (d) after baking at 300 °C for 10 mins under different gate voltage. (e) The I_D-V_G curve for the device after baking at 300 °C for 10 mins and the saturation threshold voltage is extracted to be around 8.6 V.

3.4 Conclusions

Room temperature solution-deposited silver nanowire networks embedded in ITO-NP matrices demonstrate significant improvement in surface morphology, mechanical adhesion, and flexibility while maintaining the sheet resistance and transmittance values necessary to replace conventional sputtered ITO thin films. Surrounding the silver nanowire network by ITO has been observed to dramatically improve wire-to-wire conductance. The improved surface morphology is achieved by completely filling the gaps

left between nanowires and fully covering the nanowires with nanoparticles. Anchoring the nanowire network in place using nanoparticle matrix also offers excellent substrate adhesion and mechanical flexibility. We expect that electrode structures of metal nanowire networks embedded in conductive metal oxide nanoparticle matrices can be successfully incorporated into a variety of device structures suitable for a diverse set of applications.

Solution-processed silver nanowire-sol-gel TiO_X composite electrode was demonstrated to reduce the sheet resistance of the silver nanowire network while improving the thermal stability under various temperatures and treatment times over bare silver nanowire electrodes by suppressing the surface diffusion of silver atoms during the thermal treatment. Sol-gel TiO_X are also shown to provide excellent chemical corrosion resistance for the silver nanowire network preventing the sulfurization of silver atoms. Both the thermal stability and chemical stability enhancement highlight the superior performance of a full coverage layer, compared to bare silver nanowire networks and silver nanowire/NP composite electrode with the NPs forming a nanoporous protection layer. Better thermal and chemical stabilities open up new possibilities for post-fabrications with high temperatures or harsh chemical conditions. This is demonstrated by applying silver nanowire-sol-gel TiO_X composite electrode as the electrode of TFT devices in which post fabrication annealing successfully improve the observed device performance. Moreover,

the sol-gel TiO_X layer can greatly improve silver nanowire's adhesion to the substrate and the composite electrodes show excellent flexibility, making it a promising candidate for flexible electronics.

Supplemental Information

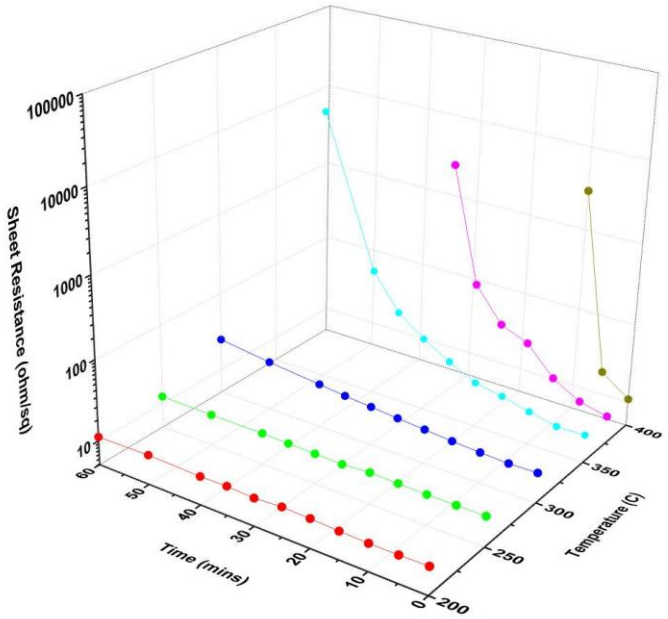

Figure S3.1 The sheet resistances of silver nanowire-sol-gel TiO_X films changed with time under different temperatures were recorded from 200 °C to 400 °C for up to 1 hour. The measurement limit is 120 Mohm/sq. The higher temperature would accelerate the reaction and the results indicate the thermal stability of the silver nanowire-sol-gel TiO_X electrode.

Chapter 4 The Role and Methods of Sodium Doping in $Cu_2ZnSn(S,Se)_4$ Solar Cells

4.1 Introduction

The fast progress of CZTS research benefits from previous understandings on related materials such as CIGS. In particular, the beneficial role of sodium in enhancing device performance and improving materials properties of both CIGS and CZTS has been reported in the literature.[103-107] Sodium incorporation was recognized to enhance the grain growth, passivate deep defects, increase carrier density and results in better device performance, mainly through increasing the V_{OC} and FF.[105, 108-111] Sodium incorporation is usually achieved by the diffusion from the soda-lime glass (SLG) through the Mo layer to the CIGS or CZTS layer.[112, 113] This approach, however, makes precise control of the sodium profile challenging, and it is seriously affected by the Mo layer conditions. Moreover, it is ineffective for lightweight and flexible CZTS thin film solar cells. Therefore, a well-controlled sodium incorporation method is needed not only to further improve the film quality and device performance, but also to enable fabrication on alternative substrates, such as PET. Highly efficient CIGS solar cells were demonstrated using post-treatment deposition of NaF vapor, which proved to be an effective way to

introduce sodium.[114] However, the effects of the sodium incorporation to CZTS absorber material are still not fully understood. To explore the effectiveness of Na incorporation in improving the performance of CZTS solar cells, introducing sodium via a chemical synthesis to achieve uniform doping in nanocrystal CZTS on borosilicate glasses (BSG) were investigated in this chapter.

4.2 Experimental Details

4.2.1 Synthesis of Cu_2ZnSnS_4 Nanocrystal Solution

Kesterite CZTS nanocrystals were synthesized as previous reported by mixing 1.33 mmol of copper acetylacetonate ($Cu(acac)_2$), 1.22 mmol of zinc acetylacetonate hydrate ($Zn(acac)_2$), and 0.75 mmol of tin(IV) bis(acetylacetonate) dichloride ($Sn(acac)_2Cl_2$) into10 mL of oleylamine at 130 °C for 30 min; then, the soluiton was heated to 225 °C under an Ar atmosphere, where 2 M of sulfur solution in 2 mL of oleylamine was injected at 225 °C, and the temperature was kept at 225 °C for 1 h.[115] The reaction was cooled down to room temperature quickly, and the precipitated products were obtained by adding ethanol as the precipitant. The dissolve/precipitation procedure was repeated one more time, and the nanocrystals were acquired and fully dispersed in a nonpolar solvent, such as toluene.

4.2.2 Synthesis of Cu_2ZnSnS_4:Na Nanocrystal Solution

In a typical synthesis of CZTS:Na, firstly, proportional amount of copper acetylacetonate ($Cu(acac)_2$), zinc acetylacetonate hydrate ($Zn(acac)_2$), tin(IV) bis(acetylacetonate) dichloride ($Sn(acac)_2Cl_2$) were mixed in oleylamine under vacuum from room temperature to 130 °C, and hold at 130 °C for 30 minutes; then, the reaction was heated to 225 °C under Ar atmosphere, where sulfur in oleylamine was injected at 225°C, and the temperature was kept at 225 °C for 30 min; after that, CF_3COONa in oleic acid was injected at this temperature into the above solution for another 30 minutes. The reaction was cooled down to room temperature quickly, and the precipitation was obtained by adding ethanol as precipitant. The dissolve/precipitation procedure was repeated one more time, and the nanocrystals were acquired and fully dispersed in to non-polar solvent. The synthesis of CZTS nanocrystals is similar as the synthesis of CZTS:Na nanocrystals, except without injection of CF_3COONa and the reaction time was kept at 225 °C for 1h. The metal precursor ratio has been adjusted based on the device performance, and the optimized ratio for the metal precursors, are 1.322, 1.223, 0.75 mmol, 0.04 mmol of $Cu(acac)_2$, $Zn(acac)_2$, $Sn(acac)_2Cl_2$, CF_3COONa respectively. Other control experiment has been carried out with different reaction time and temperature for the injection of CF_3COONa, e.g. 225 °C for 15

minutes, and 250 °C for 20 minutes, or the amount CF_3COONa was adjusted with 0.02 mmol, 0.08 mmol, and 0.16 mmol, respectively.[105]

4.2.3 Device Fabrication and Characterization

Device fabrication:

Kesterite CZTS absorber layers were prepared following the procedure described above. The CdS layer was deposited onto the CZTS layer by chemical bath deposition. Then, solution processed silver nanowire/ITO-NP composite films were spin-coated onto the devices as a transparent top electrode. The detailed experiment setup has been described elsewhere.[68] The total area of each cell is 0.12 cm^2 by mechanical scribing and the effective area is measured and calculated carefully under optical microscope.

Characterization:

The photovoltaic performance was characterized in air without any encapsulation under an AM1.5G filter at 100 mW/cm^2 using a Newport Oriel 92192 Solar Simulator, as calibrated using a silicon photodiode. The external quantum efficiency (EQE) was measured using a system designed by Enli Tech. The XRD patterns were collected on a PANalytical X'Pert Pro X-ray powder diffractometer using Cu Kα radiation (λ=1.54050Å). The TGA measurement is carried out with the Q600 TG/DTA equipment, with temperature range

varied from room temperature to 600 °C under Ar atmosphere. The XPS measurements were performed using an Omicron XPS/UPS system, with a base pressure lower than 10^{-9} mBar. A monochromatic Al Kα (1486.6 eV) X-ray source was used for excitation and the spectra were collected with a pass energy of 50 eV. The SEM images were taken on a JEOL JSM-6700F with an accelerating voltage of 5 kV. Transmission electron microscopy (TEM) images were taken on an FEI CM 120 microscope operated at 120 kV, and HRTEM images were taken on an FEI Titan scanning transmission electron microscopy (STEM) operated at 300 kV. The carrier lifetime is measured by time-resolved photoluminescence (TRPL) using Picoharp single counting system. A 635 nm semiconductor laser with a pulse width less than 0.2 ns and with repetition rate of 20 MHz is employed as excitation source. Photoluminescence signal from the samples is detected by a Hamamatsu H10330A photomultiplier tube cooled down to 60 ^{o}C during operation. The capacitance-voltage characteristics of the photovoltaic devices were measured using a Hewlett-Packard 4284A LCR Meter.

4.3 Characterization and Device Performance

The reactant molar stoichiometry of Na/(Cu+Zn+Sn) in CZTS:Na nanocrystals was adjusted from 0.5% to 10%, for further composition and structure characterizations and

device fabrication. Figure 4.2a and b show the typical TEM and high-resolution TEM images of the as-prepared CZTS:Na nanocrystals with 10% Na/(Cu+Zn+Sn).

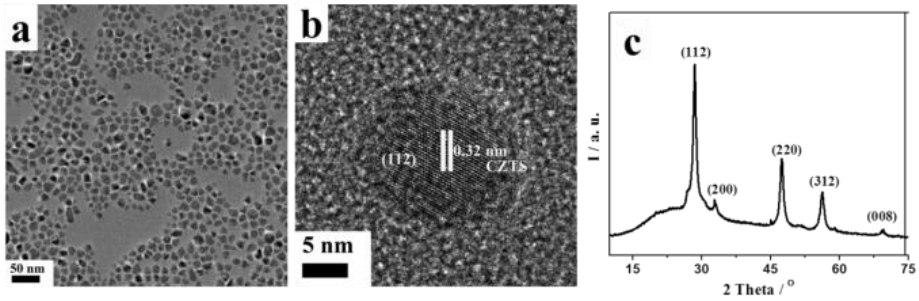

Figure 4.1 (a) TEM and (b) HRTEM image of the as-prepared CZTS:Na nanocrystals; (c) XRD pattern of the as-prepared CZTS:Na nanocrystals.

The nanocrystals, well dispersed in non-polar solvent, were highly crystallized with the particle size ranging from 15 to 20 nm. In the HRTEM image of a single CZTS:Na particle (Figure 4.2b), the center of the particle was highly crystallized with characteristic interplanar distance of 0.32 nm from a (112) plane of kesterite CZTS phase. In contrast, the surface of the nanoparticle was amorphous. Figure 4.2c shows the X-ray diffraction patterns for both CZTS:Na nanocrystals. It is clearly that CZTS:Na nanocrystals exhibited kesterite phase, with the peaks centered at 28.48°, 32.98°, 47.43°, 56.22°, and 69.49° corresponding to the (112), (200), (220), (312), and (008) planes of kesterite (26-0575), respectively. The absence of visible peaks originating from sodium species in the XRD for

CZTS:Na nanocrystals suggests that the introduction of amorphous Na on surface does not change the kesterite phase of CZTS.

Compared with the as-synthesized CZTS nanocrystals shown in Figure 4.3a and b, the slightly smaller size of CZTS:Na particles might be ascribed to both sodium interference to CZTS growth and partially dissolving of the as-formed CZTS nanocrystals. The XRD pattern is shown for comparison to CZTS:Na nanocrystals.

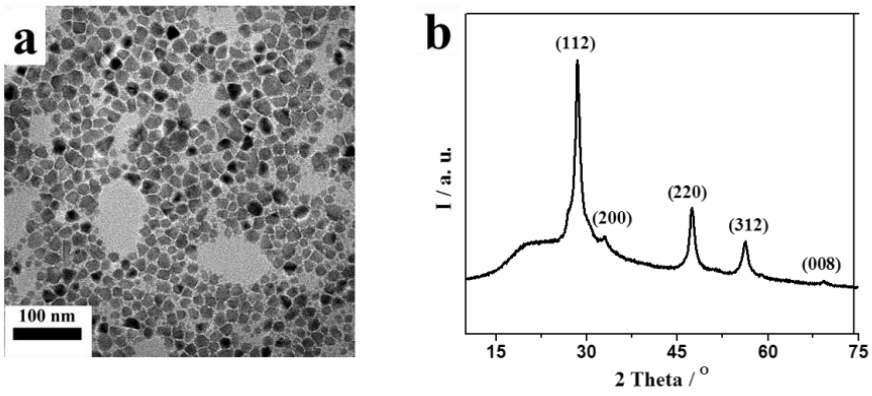

Figure 4.2 TEM image (a) and (b) XRD pattern of the as-synthesized CZTS nanocrystals.

The successful incorporation of Na in the CZTS:Na nanocrystals was further proved by the XPS characterization. The sample for XPS measurement was prepared by spin coating of the as-prepared CZTS:Na into a continuous film with fixed 10% Na/(Cu+Zn+Sn) stoichiometry. As shown in Figure 4.4a, one strong peak located at 1071 eV, indicative of Na 1s, suggested the existence of Na species in CZTS:Na nanocrystals. Other labeled peaks

included Cu (2p 3/2), Zn (2p 3/2), Sn (3d 5/2) and S (2p 3/2) in CZTS. The remaining unlabeled peaks associated with surfactant residues, such as C, O and N, coming from oleic acid, and oleylamine. High-resolution XPS scan measurement further revealed the stoichiometry of each metal element in the CZTS:Na nanocrysals. Much higher ratio of Na/(Cu+Zn+Sn) was determined by XPS measurement, suggesting surface exclusive distribution, rather than homogeneous distribution over the entire nanocrystals, for sodium species. This evidence is also in agreement with the rational design synthesis of CZTS:Na, with step wisely injection of CF_3COONa.

The STEM-EDS measurement was employed for further confirming Na distribution. Figure 4.4b and c showed a representative STEM image and line scan EDS result for two typical discrete CZTS:Na nanocrystals. The line scan measurement was carried out in the range of 75 nm, which covered two discrete nanocrystals. The plot of metal composition varied at scanning position was drawn for both Zn atom and Na atom. Notably, Zn has a large proportion in CZTS:Na nanocrystals, and no background signal needs to be taken into account. As shown in EDS results, the Na signal strongly localized on the surface of the nanocrystals, and significantly weakened across the center of nanocrystals; whereas, Zn signal kept almost constant along with the entire scan range. Different atomic distribution between Zn and Na further proved surface-exclusive nature of Na, which

coincided with the amorphous surface in HRTEM and the absence of sodium-phase in XRD pattern. The incorporation of Na species on nanocrystals surface through colloidal synthesis process is quite different from previously developed Na incorporation strategies, including pre-treatment of Mo substrate through vacuum evaporation of NaF layer with certain thickness,[116, 117] and post-treatment of nanocrystal films through soaking into NaCl solution for several minutes.[118] Both previously reported Na incorporation strategies require relatively complex procedures, and suffer a longer diffusion length for Na species within the film. It is expected that Na on the nanocrystal surface, with short diffusion length and evenly distribution, can be more favorably to passivate the defects, and against undesired residues in the CZTS film as well.

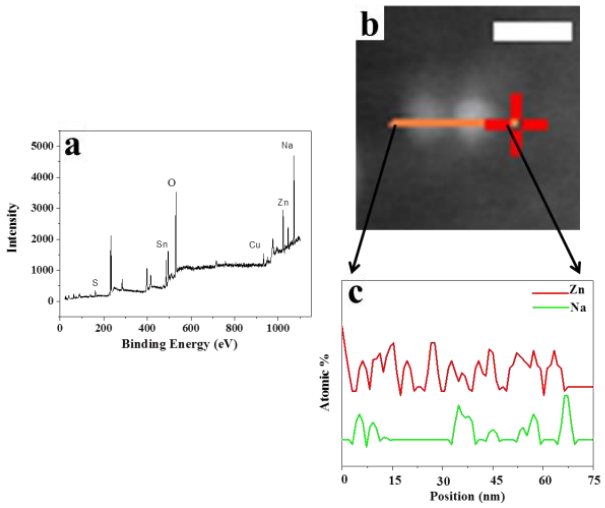

Figure 4.3 (a) X-ray photoelectron spectroscopy (XPS) analysis on solution deposited films from the as-prepared CZTS:Na nanocrystals; (b) STEM image of two typical CZTS:Na nanocrystals, scale bar stands for 50 nm; (c) line scan EDS of two CZTS:Na nanocrystals.

To study the Na effect on device performance, both CZTS:Na and CZTS nanocrystals, were used in the absorber layer of solar cells. The adopted device structure was Mo/CZTS/CdS/silver nanowires/ITO-NP, through fully solution processing.[61] Detailed device fabrication process is described in the experimental section in supporting information. Same metal stoichiometry, Cu/Sn = 1.75 and Zn/(Cu+Sn) = 0.6, were used for both CZTS and CZTS:Na nanocrystals. The Na/(Cu+Zn+Sn) ratio was adjusted to 1% for CZTS:Na nanocrystals. The BSG was adopted as the substrate to exclude the interference from Na in the substrate. Both CZTS:Na and CZTS nanocrystals were spin-coated to form a continuous film followed by a high temperature annealing in the presence of selenium.[119, 120] Figure 4.5a and Figure S4.1 showed the SEM images of the two devices. Both devices exhibited identical absorber layer structure with similar thickness of larger grain layer of CZTS, together with certain thickness of fine grain layer. This suggested that Na on the CZTS:Na nanocrystals didn't significantly affect the grain growth in the absorber layer. CZTS:Na-based and CZTS-based devices exhibited power conversion efficiency (PCE) values in the range of 5-6% and 3-4%, respectively, as shown in Figure S4.2. Two typical cell performance data are shown in Figure 4.5b and Table 4.1.

Table 4.1 Device performance of the typical CZTS:Na and CZTS based devices.

	V_{OC}	J_{SC}	FF	PCE
CZTS:Na	0.361	33.38	50.95	6.14
CZTS	0.316	30.96	39.75	3.89

The CZTS:Na-based device showed enhanced V_{OC}, J_{SC} and FF, with a much higher PCE (6.14%) than those in CZTS device with 3.89% PCE. Particularly, V_{OC} and FF, which closely related to the carrier recombination, differed significantly within both devices. When the absorber layer changed from CZTS to CZTS:Na, V_{OC} increased 14% from 0.316 to 0.361 V, and FF increased 28% from 39.75% to 50.95%. External quantum efficiencies (EQE) of the two devices are shown in Figure 4.5c. The superior performance in the CZTS:Na-based device indicates the Na spices have positive effect in CZTS photovoltaic devices. This enhancement of device performance, such as V_{OC} and FF, was consistent with the phenomena in previous vacuum based evaporated NaF method, demonstrating the effectiveness of current solution incorporation of sodium.[116] In addition, with Na inherent existing on the surface of nanocrystals, adhesion problem, coming from the evaporation of NaF film into absorber layer,[121] could be completely avoided. Furthermore, the enhanced device performances clearly demonstrated that the defect passivation in solution could benefit defect passivation in solid state.

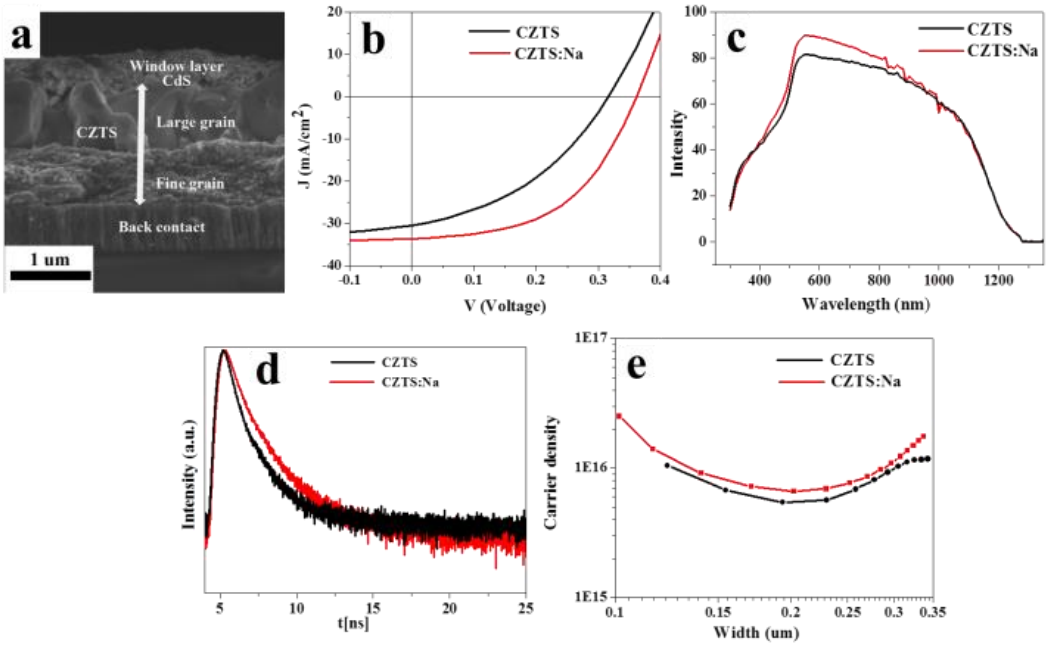

Figure 4.4 (a) SEM image of typical solar cell based on CZTS:Na nanocrystals. Electrical characterization of the CZTS:Na and CZTS devices: (b) J–V characteristics under Air Mass 1.5 illumination, 100 mW/cm^2; (c) External quantum efficiency (EQE) spectrum of the device without any applied bias; (d) TRPL of the device under low injection; (e) Capacitance-voltage measurement, with the measurement frequency of 11 kHz, the DC bias ranging from 0 V to –0.5 V, and the temperature at 300 K.

The effect from synthetic protocol and Na amount are further investigated, accordingly. First, we explored the effects of reaction time and the reaction temperature during the introduction of Na source. Because the decomposition temperature of Na precursor, CF_3COONa, is in the range of 220–270 °C, (Figure S4.3), we selected the reaction conditions at 225 °C for 15 min or 250 °C for 20 min for the second step reaction, while keeping the synthesis condition for CZTS nanocrystals unchanged. Device performances

for CZTS:Na nanocrystals prepared at different conditions were shown in Figure 4.6. All the electrical parameters for the devices were similar, with the V_{OC} ranging from 0.32 to 0.35, and FF from 54% to 58%. This suggested the effectiveness of sodium incorporation on both nanoparticle and film states based on thermolysis synthesis.

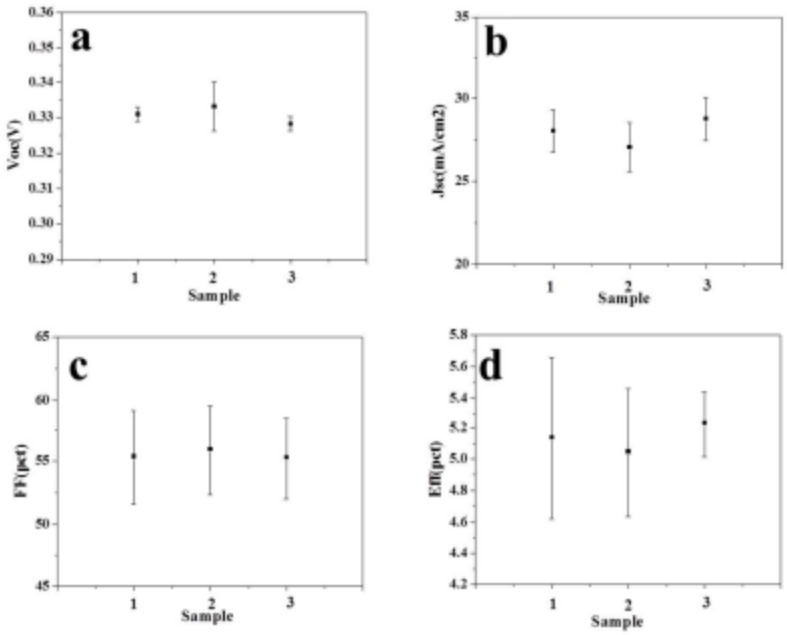

Figure 4.5 Plots of the electric property comparison between the different synthetic methods based devices, (a) V_{OC}; (b) J_{SC}; (c) FF; (d) Efficiency. The synthetic methods for sample 1, 2, and 3 are 225 °C for 15 min, 250 °C for 20 min, and 225 °C for 30 min after the injection of CF_3COONa, respectively

Different Na amount affected the CZTS:Na based devices performance significantly. Figure 4.7 showed the device performance at Na/(Cu+Zn+Sn) reactant stoichiometry of 0.5%, 1%, 1.5% and 2%, respectively. The performance, Voc and FF, reached its maximum at 1% Na/(Cu+Zn+Sn), and dropped 30% when Na content kept further rising to 2%. At

2% stoichiometry, the formation of sodium-containing impurities in the annealed CZTS film may act as charge trap centers, rather than the effective passivation layer at defects.

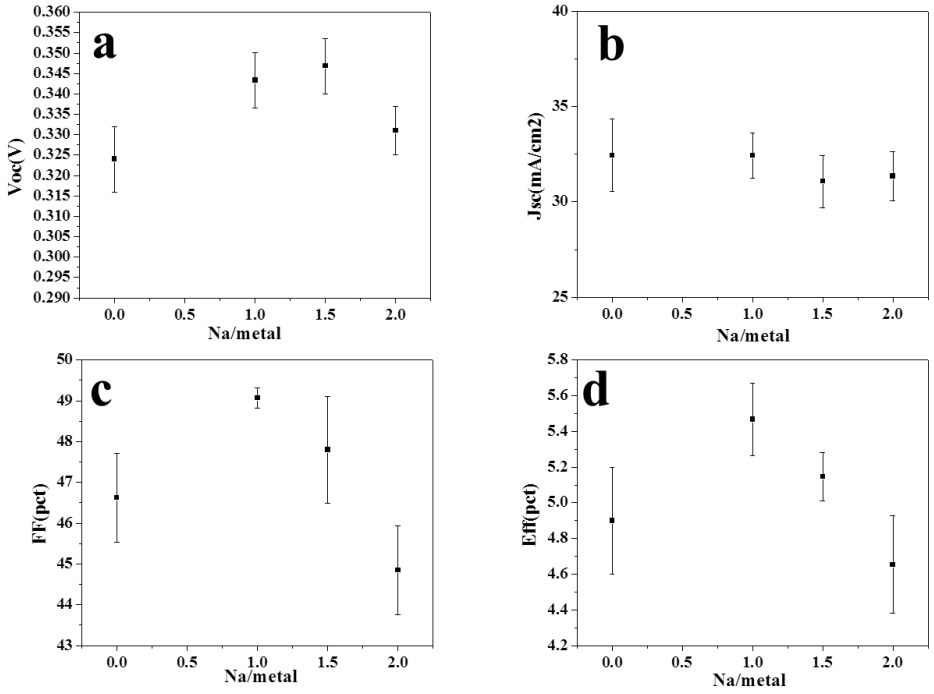

Figure 4.6 Plots of the electric property comparison between the devices made from the CZTS:Na with different Na amount, (a) V_{OC}; (b) J_{SC}; (c) FF; (d) Efficiency.

To get into the insight of the Na effect on CZTS devices, we used TRPL and CV measurement to characterize the minority carrier life-time and carrier concentration, respectively.[122, 123] In the present work, the minority carrier lifetime was obtained from TRPL profiles at low-injection levels (Figure 4.5d). 3.6 ns and 1.5 ns minority carrier lifetime were recorded for the CZTS:Na and CZTS based devices, respectively. The CV

measurements for spatial carrier density were also performed with DC bias from 0 V to –0.5 at room temperature, AC level of 5 mV, and measurement frequency of 11 kHz. The carrier densities for the CZTS:Na and CZTS devices were fitted to be 9-10×10^{15} cm^{-3}, and 8-9×10^{15} cm^{-3}, respectively, as shown in Figure 4.5e. Higher carrier concentration and longer minority carrier lifetime were both observed in current solution-passivated CZTS device. In contrast, evaporation incorporation of Na before the domain growth only raises the carrier concentration on the cost of decreased the minority carrier lifetime.[124] This difference may originate from distinct diffusion length of sodium in the devices. To achieve uniform defect passivation, evaporation passivation requires longer global ion diffusion from interface through the absorber film; whereas solution passivation only requires local diffusion to cover all interfaces within the film. It is possible that the homogeneous Na incorporation adopted in this work initiates a distinguishable mechanism to change the defect chemistry, probably extended from grain boundary to bulk.

4.4 Conclusions

In this chapter, the rational solution passivation of CZTS absorber film by the use of solution-processed CZTS:Na nanoparticle precursors and strategy of vacuum evaporation for sodium doping to CZTS are demonstrated. During the chemical incorporation method,

structure and composition characterizations, including HRTEM, EDX, and XPS, confirm the exclusive presence of sodium species around a kesterite-phase core of CZTS. Specific to solution passivation, both charge carrier concentration and minority lifetime are increased, contributing 50% increment of PCE than that of un-passivated CZTS. Current solution passivation demonstrated by the simultaneous surface passivation during precursor fabrication, presents a simple, quantitative, and versatile approach towards the pursuit for high performance photovoltaics. Quantitative introduction of sodium specifies within the absorber layer can be preciously controlled by the reactant stoichiometry; whereas for evaporation, sodium ions are difficult to diffuse into small cavities those are surrounded by grains. Besides current sodium, other metals ions those can be nucleated onto the core semiconductor materials, including Li, K, and even non-alkali metal or the combinations, may also be explored by simply switching the reactants. Additionally, other photovoltaics, such as CIGS and CdTe thin film technique, may also be benefit from the solution passivation.

During physical incorporation method, it is found that sodium incorporation plays an important role in determining the crystallinity and electrical properties of CZTS solar cells. With the introduction of sodium into the CZTS films, an enhancement of the (220/204) orientation was observed after selenization. In addition, deposition of the NaF layer can

suppress the $Mo(S,Se)_2$ formation, which is beneficial for further improving the performance of CZTS solar cells. A highest PCE of 6.2% was achieved with 5 nm NaF deposited at the Mo/CZTS interface prepared on non-SLG, superior to that of SLG (5.48%). The amount of sodium and the incorporation strategy were found to influence the device performance significantly. Proper amount of sodium incorporation could enhance the V_{OC} and FF, although a slight decrease in J_{SC} was also observed. Moreover, the temperature dependent CF, CV and DLCP measurements showed that introducing sodium could increase the free carrier density as well as interface states, and that lower acceptor defect energy, instead of lower deep defect density, can also be expected. These measurements agree with the device performance (V_{OC} and FF improvement and J_{SC} reduction) with and without sodium. We anticipate that the present approach of sodium incorporation and the characterization results can be used to further examine the orientation properties and growth mechanism, and facilitate the development of high performance devices on alternative substrates.

Supplemental Information

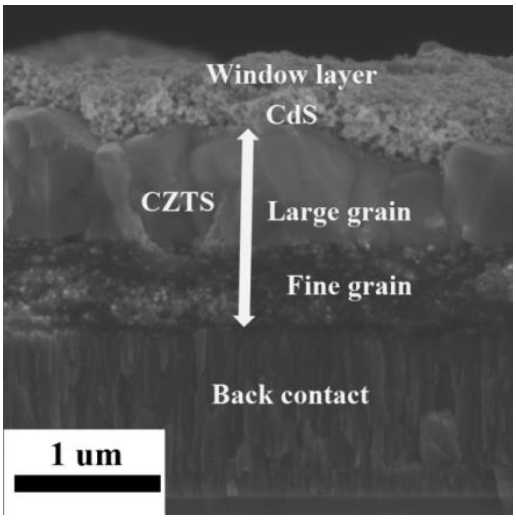

Figure S4.1 SEM image of CZTS solar cells based on CZTS nanocrystals

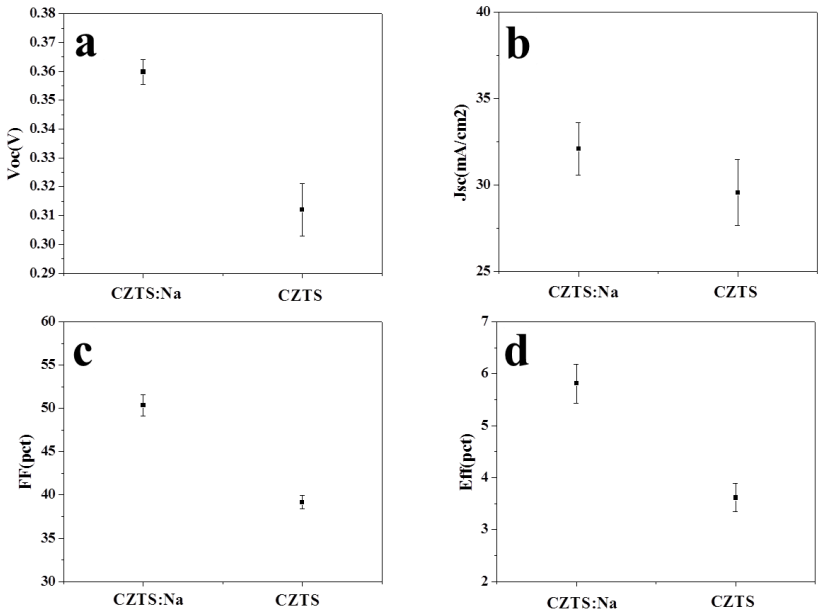

Figure S4.2 Plots of the electric property comparison between CZTS:Na and CZTS based devices, (a) V_{OC}; (b) J_{SC}; (c) FF; (d) Efficiency.

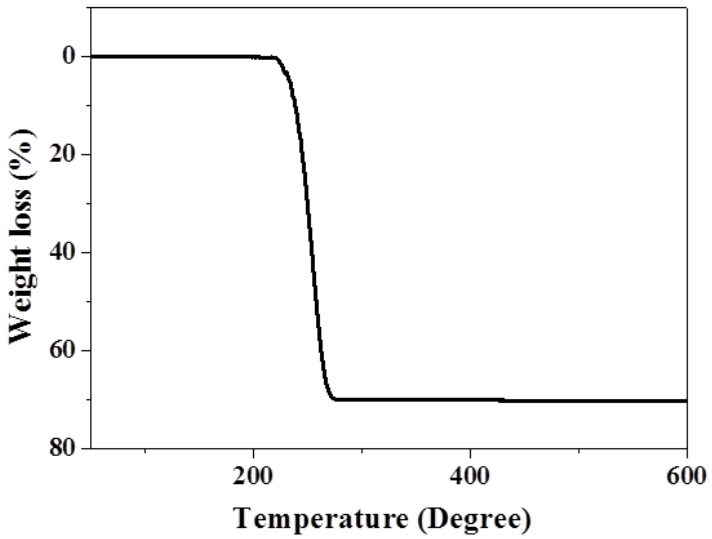

Figure S4.3 TG run of CF3COONa precursor.

Chapter 5 Unraveling Film Transformations and Device Performance of Planar Perovskite Solar Cells

5.1 Introduction

Thin film solar cells, such as CIGS, CdTe and a-Si have been developed as promising alternatives to crystalline silicon solar cells as more cost-effective technologies.[17, 114, 125-128] As a result of the efficient direct band gap absorption, the thickness of thin film solar cells could be effectively reduced to sub-micrometer or even hundreds of nanometers. The potential low cost (cents/watt) of solar cells can be achieved through the combination ofreduced material cost and high device performances. [129] The high performance of CIGS and other compound absorbers, however, relies on vacuum based and/or high temperature processes which would lead to high manufacturing costs and limit the choice of substrates. As discussed in the Chapter 1, hybrid organic/inorganic perovskite absorbers, especially methylammonium lead halide $CH_3NH_3PbX_3$ (X =Cl, Br and I)-based, have attracted significant attention as promising materials for thin film solar cells. Extraordinary power conversion efficiencies (PCEs) of over 17% were achieved during the past five years and the materials have been demonstrated as capable of being prepared using a number of low temperature processes, making these materials especially attractive for low cost and

scalable manufacturing of next generation thin film photovoltaic devices. [42, 55, 130, 131] Perovskite $CH_3NH_3PbX_3$-based solar cells have shown to possess desirable properties such as an extremely high absorption coefficient, efficient ambipolar transport, and a tunable direct band gap, allowing them to be excellent solar absorbers and carrier transporters.[43, 52, 132-136] However, how to effectively control the material growth, film formation, and film qualityis still under investigation. In previous works, the morphology, stoichiometry and crystallinity of these materials were found to affect the device performance significantly.[137-140] Deposition techniques, treatments and film formation conditions are critical to achieve high efficiency solar cells.[45, 46, 141] Dualeh et al. showed that the depositing a $CH_3NH_3PbI_{3-x}Cl_x$ precursor onto mesoporous titanium dioxide (TiO_2) structure under proper annealing temperature can lead to formation of $CH_3NH_3PbI_3$ perovskite material resulting in reduced pin holes within the film.[137] Eperson et al. demonstrated that the annealing temperature, film thickness and thickness of compact TiO_2 layer can influence the coverage of $CH_3NH_3PbI_{3-x}Cl_x$ which would further impact the device performance.[138] These studies furthered our understanding on the correlation between film formation and device performance. However, to further improve the device performance, it is crucial to understand the film's properties and the quality of the films from the perspective of phase formation. During the formation of $CH_3NH_3PbX_3$ perovskite

film from the molecular solution, different phases are observed and those phases coexisting with the $CH_3NH_3PbI_3$ phase in the films are considered secondary phases. Secondary phases play a crucial role in the semiconductor materials and could significantly alter the device performance. For example, the order vacancy compound (OVC) $CuIn_3Se_5$ phase in CIGS improves electrical transport within the n-type CdS layer.[142-144] On the other hand, the semimetallic phase Cu_2Se in CZTS could lead to the formation of shunt paths and recombination centers and thus deteriorating the device performance.[145] In this paper, the phase transition during the $CH_3NH_3PbI_{3-x}Cl_x$ film formation was observed and the secondary phases' effects on the film formation, film properties and device performance were investigated.

5.2 Experimental Details

5.2.1 Preparation of Precursor, Thin Films and Devices

The CH_3NH_3I (MAI) was synthesized by reacting 24 mL of methylamine (33 wt.% in absolute ethanol, Sigma) with 10 mL of hydroiodic acid (HI) (57 wt% in water, Aldrich) in a round-bottom flask at 0 °C for 2 h with stirring. The precipitation was extracted by putting the solution on a rotary evaporator and carefully removing the solvent at 50 °C. The raw product CH_3NH_3I was re-dissolved in absolute ethanol and precipitated upon the

addition of diethyl ether. After filtration, the step was subsequently repeated. The solid was collected and dried at 60 °C in a vacuum oven for 24 h. The $PbCl_2$, Li-bis(trifluoromethanesulfonyl) imide (Li-TFSI) and tert-butylpyridine (tBP) were purchased from Aldrich. Spiro-OMeTAD was purchased from Lumtec. Low temperature TiO_2 solution was prepared as previous report.[146] The TiO_2 solution (3mg/ml) was spin-coated on pre-cleaned ITO substrates at 3000 r.p.m. and then baked 150 °C for 30 mins. A 0.73 M perovskite solution was prepared from $PbCl_2$ and MAI with (1:3 mole ratio) in DMF and spin-coated onto the ITO/TiO_2 substrate at 2000 r.p.m. and then baked at 100 °C for different time inside a dry air glovebox under 25 ppm H_2O. The Spiro-OMeTAD was used as a hole transporting layer and dissolved in chlorobenzene (180 mg/ml). The Li-TFSI was dissolved in acetonitrile (170 mg/ml) and 20 μl tBP. The Li-TFSI solution was added to the Spiro-OMeTAD solution at a ratio of 1:40. Then, Li salt doped Spiro-OMeTAD solution was spin-coated at 2000 r.p.m. onto the perovskite layer. Finally, a gold electrode was evaporated onto the hole transport layer. The device area was defined withshadow mask with an area of 0.114 cm^2 for measurement.

5.2.2 Characterization of Thin Films and Devices

XRD data were collected on Panalytical X'Pert Pro X-ray Powder Diffractometer with Cu

Kα radiation (λ = 1.54056 Å). The SEM were performed with field-emission electrons using Nova 230 Nano SEM. The TRPL using Picoharp single counting system using 632.8 nm semiconductor laser with a pulse width less than 0.2 ns and with repetition rate of 1 MHz as excitation source was used for carrier lifetime measurement. The photovoltaic performance was characterized without any encapsulation under an AM1.5G filter at 100 mW/cm^2 in air using Newport Oriel 92192 Solar Simulator and the intensity was calibrated using a certified silicon photodiode.

5.3 Result and Discussion

5.3.1 Phase Identification and Proposed Reaction Pathway

The $CH_3NH_3PbI_{3-x}Cl_x$ perovskite absorber was deposited using a one-step method onto the ITO/TiO_2 substrates by spin coating from a 1:3 molar ratio solution of $PbCl_2$ and MAI in dimethyl foramide (DMF) and annealed at 100 ˚C, which is reported to promote good film coverage and can provide sufficient energy for the perovskite phase formation (Details of the film preparation are shown in experimental section).[137] The $CH_3NH_3PbI_3$ is most commonly prepared by thermal annealing at 80~100 ˚C. Annealing temperatures below this range (between 60~80 ˚C) would result in slow transformation rates, while temperatures lower than 60 ˚C could be too low to drive the transformation. Higher

annealing temperatures (>120 ˚C) would accelerate the decomposition of $CH_3NH_3PbI_3$ and induce a poor film coverage.[137, 138] Thus, the temperature was fixed at 100 ˚C to investigate the phase transformation at different annealing times. The phase transformation was characterized by XRD with results shown in Figure 5.1. The peak at 2θ = 7.4 degrees arises from the precursor complex and those of 2θ = 12.7, 14.2 and 15.6 degrees corresponds to PbI_2 (001), $CH_3NH_3PbI_3$ (110) and $CH_3NH_3PbCl_3$ (100) orientation respectively (used as signature peaks for tracking phase transformation and indicated by circle, triangle, diamond and square in Figure 5.1).

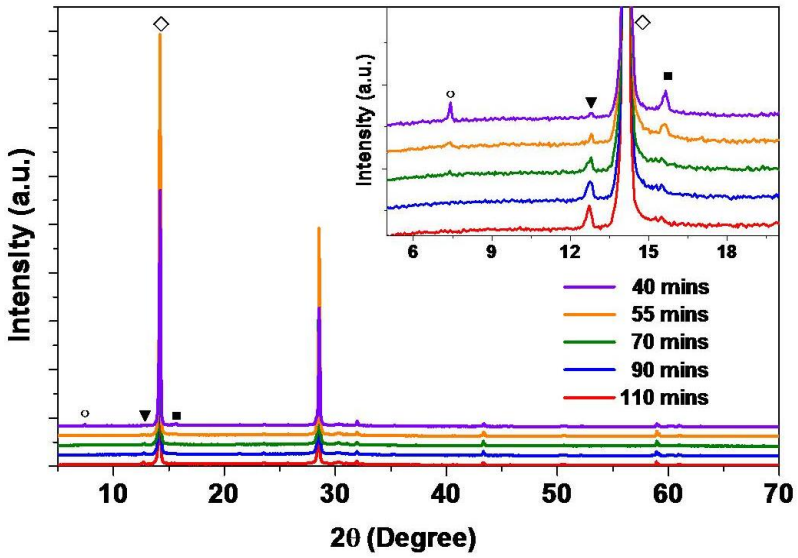

Figure 5.1 X-ray diffraction (XRD) patterns of $CH_3NH_3PbI_{3-x}Cl_x$ film formation. The phase transformation was observed from annealing times of 40 mins to 110 mins. The inset is the enlarged XRD result within 5 to 20 degrees.

All observed peaks came from the aforementioned four phases and no extra phases were

present according to the observation of the diffraction patterns. As seen in the XRD measurement, the precursor complex phase almost disappeared at 70 mins annealing time which indicated the nearly complete transformation from precursor to solid phases. Surprisingly a certain amount of PbI_2 phase was observed even at 40 mins annealing, which is before the complete transformation as identified by the disappearance of the precursor complex peak at 2θ = 7.4 degrees. This indicated that PbI_2 phase formed under this annealing temperature easily even for less than 40 mins (XRD pattern at 25 mins annealing time shown in the Figure S5.1) and it was deduced to come from the ion exchange between $PbCl_2$ and MAI. The generated PbI_2 reacted meanwhile with MAI to form $CH_3NH_3PbI_3$, and $PbCl_2$ reacted with CH_3NH_3Cl (MACl), which was generated from $PbCl_2$ and MAI, to form the $CH_3NH_3PbCl_3$ phase. The PbI_2 peaks are still present even with the incorporation of excess MAI into the precursor solution, as shown in Figure S5.2. The result indicated that the PbI_2formed at nearly stage and was later transformed into $CH_3NH_3PbI_3$ perovskite phase by reacting with MAI. Except for $CH_3NH_3PbI_3$, other phases are hardly seen from full XRD spectrum because of the extremely small amounts of those phases. In order to evaluate the relative amount of the precursor complex, PbI_2 and $CH_3NH_3PbCl_3$ phase present during the phase change, the area ratio of the precursor complex peak at 2θ=7.4 degrees, PbI_2 (001) and $CH_3NH_3PbCl_3$ (100), as relative to the $CH_3NH_3PbI_3$ (110) peak

were calculated using Gaussian fitting. At 55 mins annealing time, the ratio of precursor complex, $CH_3NH_3PbCl_3$ and PbI_2 to $CH_3NH_3PbI_3$ were 0.21%, 1.79% and 0.16% respectively. When the annealing time was increased to 70 mins, the amount of the precursor complex and $CH_3NH_3PbCl_3$ phase reduced to 0.05% and 1.25% and the PbI_2 phase increased to 0.53%. It can be assumed that the $CH_3NH_3PbI_3$ phase formation was nearly complete and the increase in the relative amount of PbI_2 phase mainly came from the $CH_3NH_3PbI_3$ phase decomposition and precursor reaction. Moreover, the reaction of $PbCl_2$ with MAI to generate PbI_2 caused the depletion of $PbCl_2$ which in turn would facilitate the decomposition of $CH_3NH_3PbCl_3$ phase reflected by the deceasing $CH_3NH_3PbCl_3$ peak ratio. After 90 mins annealing, the area ratio of the PbI_2 (001) peak relative to the $CH_3NH_3PbI_3$ (110) peak increased up to 1.70%. The films with longer annealing time, for example 110 mins, generated more PbI_2 phase and less $CH_3NH_3PbCl_3$ phase. It is noted that the secondary phases will coexist in the solution processed $CH_3NH_3PbI_{3-x}Cl_x$ film and it would be a challenge to obtain a pure $CH_3NH_3PbI_3$ phase. Summarizing the information obtained from XRD characterization on the solution processed $CH_3NH_3PbI_{3-x}Cl_x$ phase transformation, possible transformation pathways are proposed in Figure 5.2.

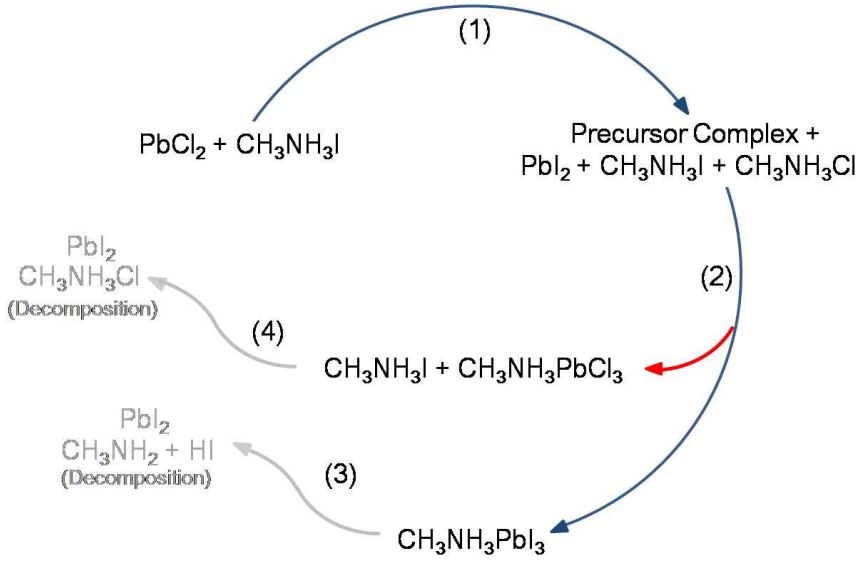

Figure 5.2 Possible transformation pathway of solution processed CH3NH3PbI3-xClx film: (1) $PbCl_2 + 3CH_3NH_3I \rightarrow PbI_2 + CH_3NH_3I + 2CH_3NH_3Cl$; (2) $PbI_2 + CH_3NH_3I \rightarrow CH_3NH_3PbI_3$; $PbCl_2 + CH_3NH_3Cl \rightarrow CH_3NH_3PbCl_3$; (3) $CH_3NH_3PbI_3 \rightarrow PbI_2 + CH_3NH_2 + HI$; (4) $CH_3NH_3PbCl_3 + 3CH_3NH_3I \rightarrow$ (1) + CH_3NH_3Cl.

At path (1), $PbCl_2$ and MAI in the DMF reacted to form PbI_2 and MACl while coexisting with MAI and a possible precursor complex. During annealing at path (2), PbI_2 reacts with MAI and $PbCl_2$ reacts with MACl to form $CH_3NH_3PbI_3$ and $CH_3NH_3PbCl_3$. The $CH_3NH_3PbI_3$ phase formed from path (2) can decompose under thermal annealing at 100 ° C to generate PbI_2 phase, CH_3NH_2 and HI at path (3). The excess MAI can continue to react with $PbCl_2$ to generate PbI_2, facilitating the decomposition of the $CH_3NH_3PbCl_3$ phase (4). When the excess MAI depleted, the decomposition mechanism of $CH_3NH_3PbI_3$ and $CH_3NH_3PbCl_3$ phases dominates, and the relative amount of PbI_2 phase rose gradually. This proposed pathway takes into account both results from the XRD characterization here

and previous reports.[137, 147-149]

5.3.2 Device Performance

$CH_3NH_3PbI_3$ films with different annealing conditions were prepared, while lithium slat doped Spiro-OMeTAD was employed as the hole transport layer and finally gold (Au) was evaporated as the back electrode. Current density-voltage (J-V) curves were measured by reverse bias scan under 1 sun AM 1.5G illumination and device parameters are shown in Figure 5.3a. Typical J-V curves for the three conditions were shown in Figure 5.3b, where the perovskite film were obtained from 40, 70 and 110 mins annealing, corresponding to the early formation, near completed and the over-annealing stages. The highest averaged PCE was achieved for the perovskite film annealed for 70 mins and it corresponds to the near completed stage where the smallest amount of secondary phases is present (less than 2% for the sum of the four specific peak areas corresponding to the four phases). At annealing times shorter or longer than 70 mins, the device performances were reduced. From the summarized device parameters chart in Figure 5.3a, perovskite films with 40 mins annealing time exhibited poor V_{OC} and slightly lower FF. When increasing the annealing time to 55 mins, the V_{OC} and FF were improved by 4% and 1.5% respectively. During this period, the total amount of the secondary phases was reduced from 4.3% to

2.1%. In addition to the decrease in the amount of the precursor complex and $CH_3NH_3PbCl_3$ phase, the gradual increase of PbI_2 phase in the film at 70 mins annealing together attributed to an improved V_{OC} and FF, but a slightly lower J_{SC}. The PbI_2 phase was reported to improve the device performance by passivating the grain boundaries which generally worked as recombination centers.[148, 150] However, excessive PbI_2 phase will reduce the light absorption efficiency in the film due to the larger band gap of PbI_2 (2.4 eV) which contributed to the lower J_{SC}.[137] After 90 mins of annealing, the percentage of the secondary phases present in the film rose to 4.0% mainly due to an increase of PbI_2 phase. The V_{OC} of the devices were higher in comparison to that of annealing for 40 mins where a similar amount of secondary phases was present, although with different compositions (more precursor phase and less PbI_2). Thus the precursor phase could be the main reason behind the lower V_{OC} of the device at 40 mins annealing time. The PCEs of those devices with over 90 mins annealing are still low, however, mainly limited by the low J_{SC} value (Device performance after 190 mins of annealing is shown in Table 5.1). While the devices obtained from perovskite film with 70 mins of annealing exhibited high average PCEs, those with 55 mins of annealing exhibited the highest averaged J_{SC} among all the conditions. Therefore controlling the PbI_2 phase within 0.5% the amount of $CH_3NH_3PbI_3$ and tuning the amounts of precursor and $CH_3NH_3PbCl_3$ phases in the perovskite films are important

to simultaneously achieve efficient light absorption, effective grain boundary passivation and reduced recombination centers.

Table 5.1 The averaged four device parameters of V_{OC}, J_{SC}, FF, and Eff with varying annealing time.

	V_{OC}(V)	J_{SC} (mA/cm^2)	FF (%)	Eff (%)
40 mins	0.978	19.35	68.94	13.04
55 mins	1.018	19.64	70.04	14.00
70 mins	1.033	19.37	70.37	14.08
90 mins	1.038	18.82	71.15	13.89
110 mins	1.024	18.15	69.15	12.85
190 mins	1.015	16.54	69.58	11.69

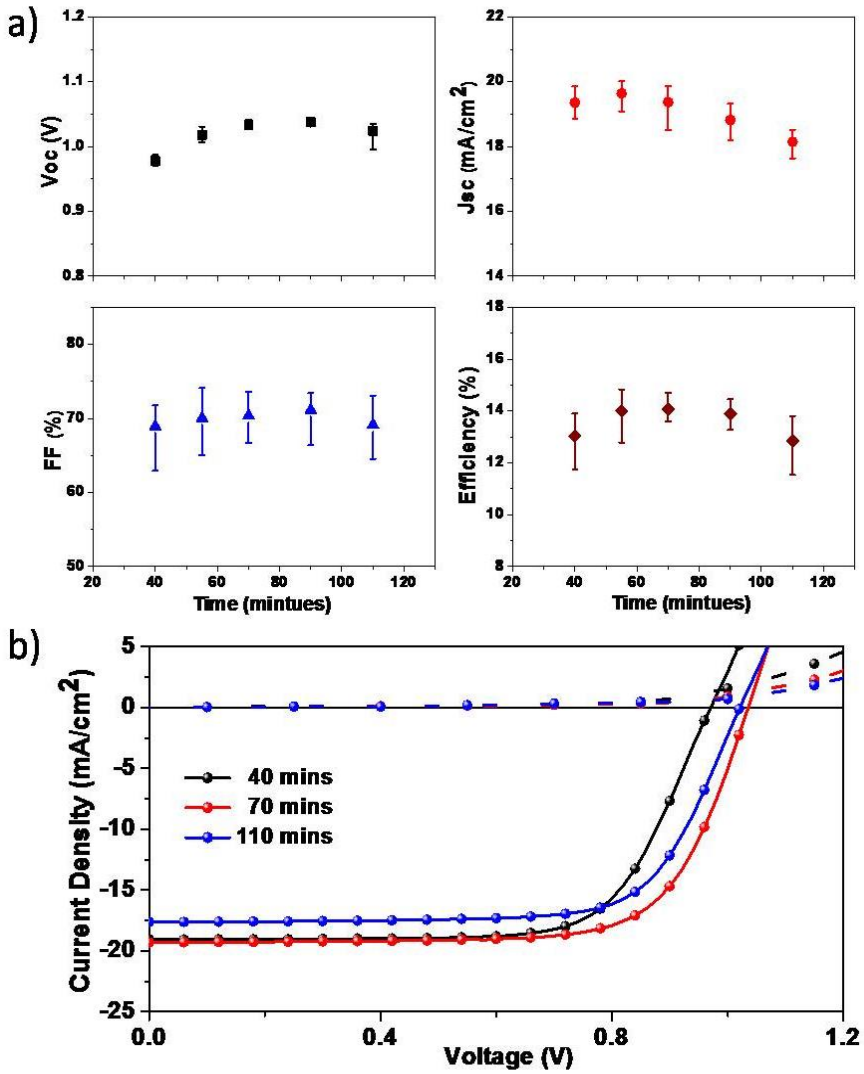

Figure 5.3 Device performance of the $CH_3NH_3PbI_{3-x}Cl_x$ films with varying annealing times (a) the summarized device parameters. (b) Typical current density-voltage characteristics for 40 mins, 70 mins and 110 mins annealing time.

5.3.3 Characterization

Furthermore, the $CH_3NH_3PbI_{3-x}Cl_x$ film morphologies during the transformation were characterized by SEM as shown in Figure 5.4. A high surface coverage (>95%) of $CH_3NH_3PbI_{3-x}Cl_x$ films were achieved with thermal annealing at 100 ˚C within 70 mins of

annealing which reduced the possibility of shunt paths formation thereby reducing leakage current in the solar cells. The high surface coverage obtained within 70 mins of annealing in this study indicates that surface coverage was not a major factor for the changes in device performance instead the evolution of the secondary phases played a vital role in device performance. When the annealing time exceeds 70 mins, bright spots and voids between grain boundaries appeared, which were deduced to be coming from the decomposition of $CH_3NH_3PbI_3$ phase into PbI_2 phase and the loss of $CH_3NH_3PbCl_3$ phase. At annealing times of 110 mins or longer, the surface coverage gradually decreased and the original conformal films were broken into small grains and branches (SEM images with different scales shown in Figure S5.3) and more pronounced void formation was observed between the crystal grains. Such changes in the microstructure may lead to direct contact between the electron and hole transporting layers, leading to an increase in the leakage current of the devices was increased due to these shunt paths formation. In addition, an increase in voids indicates a less effective absorption area within the absorber. Thus, a decrease in device performance was attributed to the combined effects of changes in the amount of PbI_2 phase and changes in the thin film morphology at longer annealing times.

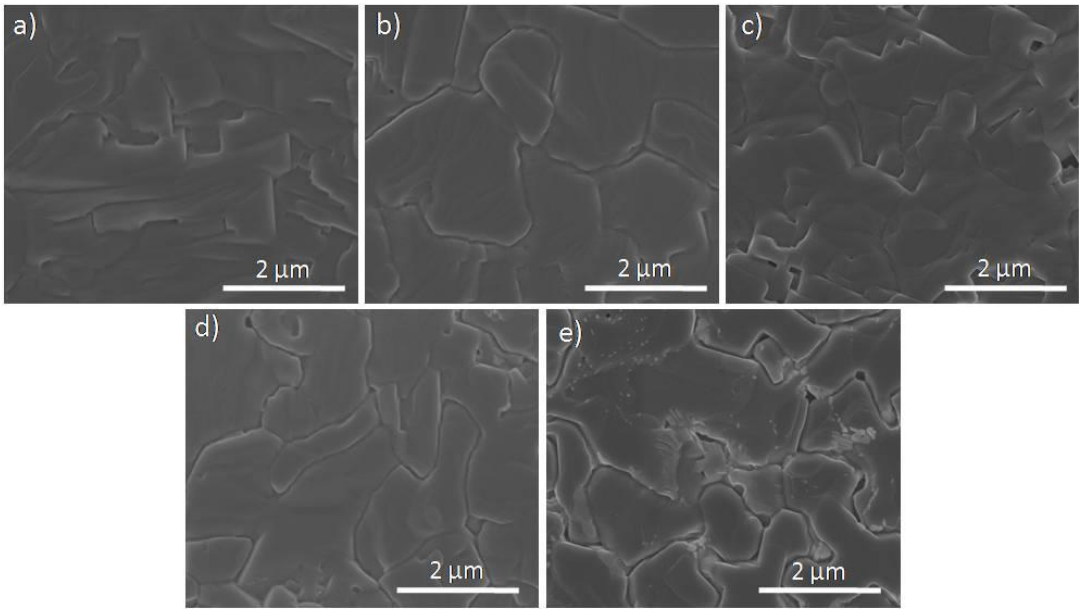

Figure 5.4 SEM images of perovskite film morphologies annealing at 100 °C for (a) 40 mins (b) 55mins (c) 70mins (d) 90 mins and (e) 110 mins.

The TRPL measurements with a 632 nm wavelength and 1 MHz frequency pulsed laser were performed on TiO_2/ $CH_3NH_3PbI_{3-x}Cl_x$ films to best simulate the device structure at room temperature and the results were shown in Figure 5.5 measuring the peak emission at 775 nm. The TRPL data was fitted by two exponential decay curves and the minority carrier lifetime (τ) of the films obtained at different conditions were 0.44 µs, 0.89µs and 0.53 µs corresponding to annealing times of 40 mins, 70 mins and 110 mins respectively. Longer minority carrier lifetime is associated with longer diffusion length ($L_D = \sqrt{D\tau}$, D is the diffusion coefficient of carriers) and reduced carrier recombination rates. For films annealed for less than 70 mins, the precursor phase and other secondary phases can act as

recombination centers in the material or induce stronger interface recombination with the hole transport layer or electron transport layer which would cause the V_{OC} to drop significantly. It is interesting to note that the shorter carrier lifetime did not influence the J_{SC} in the device performance, e.g. the absorber obtained at 40 mins. This is the first time to our knowledge that this effect is observed in the $CH_3NH_3PbI_{3-x}Cl_x$ perovskite solar cells. The J_{SC} reflects the collection efficiency of the p-i-n junction relative to the total number of carriers generated by light absorption. Comparing the 40 mins and 70 mins annealed films, the total amount of generated charges does not vary significantly possibly because most of the $CH_3NH_3PbI_3$ phase was formed by 40 mins and the electrical field across the perovskite layer can sweep the photogenerated carriers rapidly even with the presence of secondary phases. When the films were annealed at longer times (>110 mins), the PbI_2 phase became the dominant secondary phase in the films and the perovskite gains were segmented according to SEM characterization. The shorter τ can be directly correlated with the decrease in V_{OC} of the device performance which in turn is due to the increase of secondary phases and extent of carrier recombination. Compared with the previous studies based on vapor-assisted solution process (VASP) of $CH_3NH_3PbI_3$ perovskite solar cells, Chen *et al*. showed that over a certain amount of PbI_2 formation caused the minority carrier lifetime slightly decreased. Moreover, it did not change the film morphologies

significantly.[150] However, in the one-step solution processed $CH_3NH_3PbI_{3-x}Cl_x$, the phase transformation resulted in different film morphologies and the consequently varying device performances. Moreover, the TRPL results correspond with previous reports using impedance spectroscopic measurement that showed short electron lifetime resulted from incomplete reaction between PbI_2 and MAX, and from excessive PbI_2 formation in mesoporous structured $CH_3NH_3PbI_{3-x}Cl_x$ solar cells.[137] The effects on minority carrier lifetime and morphologies are in good agreement with the current-voltage characteristic of the devices and those films with proper annealing time (55~70 mins) exhibited decent minority carrier lifetime (>0.8 μs) and film coverage.

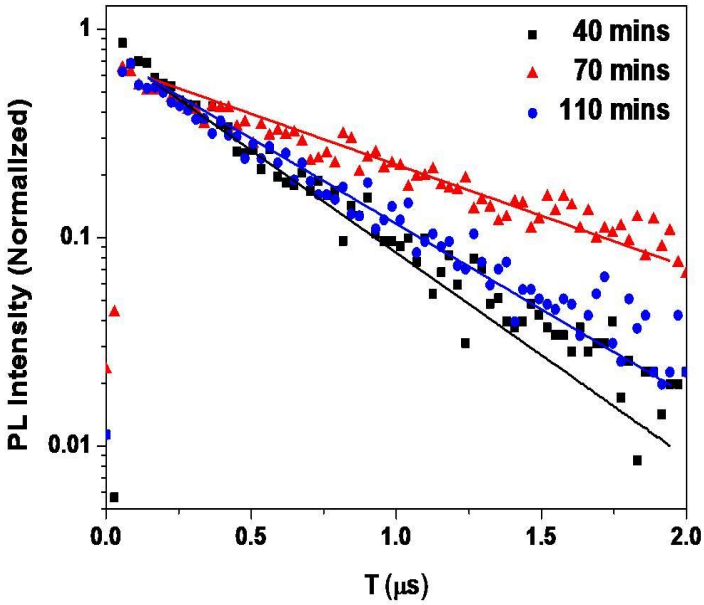

Figure 5.5 Time-resolved photoluminescence of perovskite film with (a) 40 mins (b) 70 mins (c) 110 mins on TiO_2 substrates at room temperature.

5.4 Conclusions

In this chapter, the evolution of various phases was shown through a series of characterizations for the phase transformation of perovskite thin films based on solution processed $CH_3NH_3PbI_{3-x}Cl_x$. The XRD results indicated that multiple secondary phases, including a precursor complex, PbI_2, and $CH_3NH_3PbCl_3$ formed during the perovskite formation. The device performance showed that less secondary phases will result in better PCEs, while it is a challenge to achieve pure $CH_3NH_3PbI_3$ phase from the single step co-deposition process from $PbCl_2$ and MAI precursors. The SEM and TRPL results were consistent with the device performance measurements and further elucidated the relation between phase transformation and device performance. Based on these results, possible reaction pathways were proposed to unravel the evolution of phases as the film formation occurred during the annealing process. The phase transformation based on different film preparation processes, e.g. two step solution process, vacuum deposition, and co-deposition solution process from PbI_2 precursor instead of $PbCl_2$ should be further studied to address the Cl species effect and to improve device performance. We believe that the present understanding of the phases' effects will facilitate the rational design of perovskite materials and expedite the development of this emerging photovoltaic technology.[151]

Supplemental Information

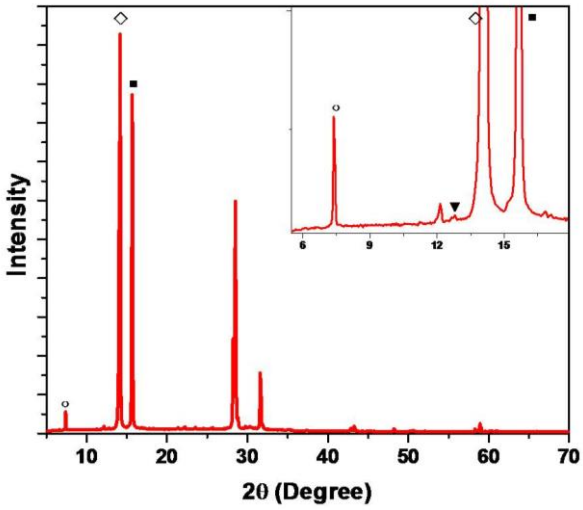

Figure S5.1 X-ray diffraction pattern of the film with 25 mins annealing time at 100 °C.

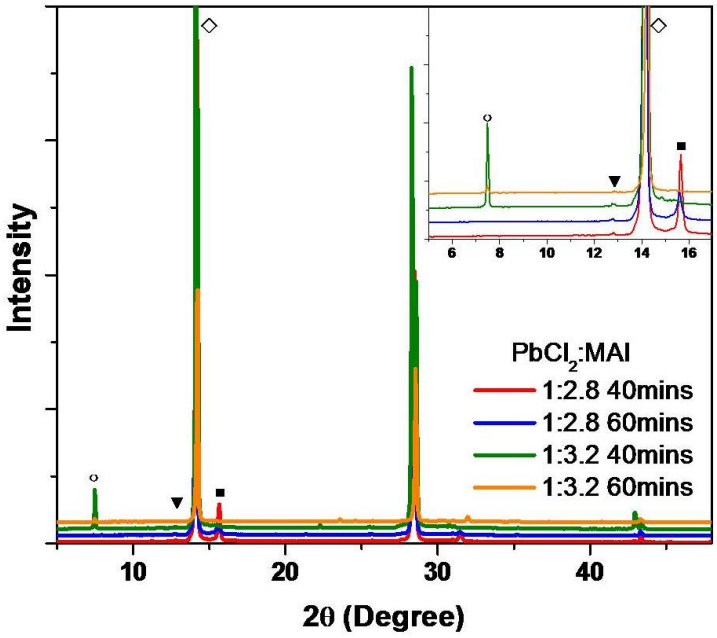

Figure S5.2 X-ray diffraction pattern of the films prepared from varying $PbCl_2$ to MAI ratios in DMF at varying annealing times.

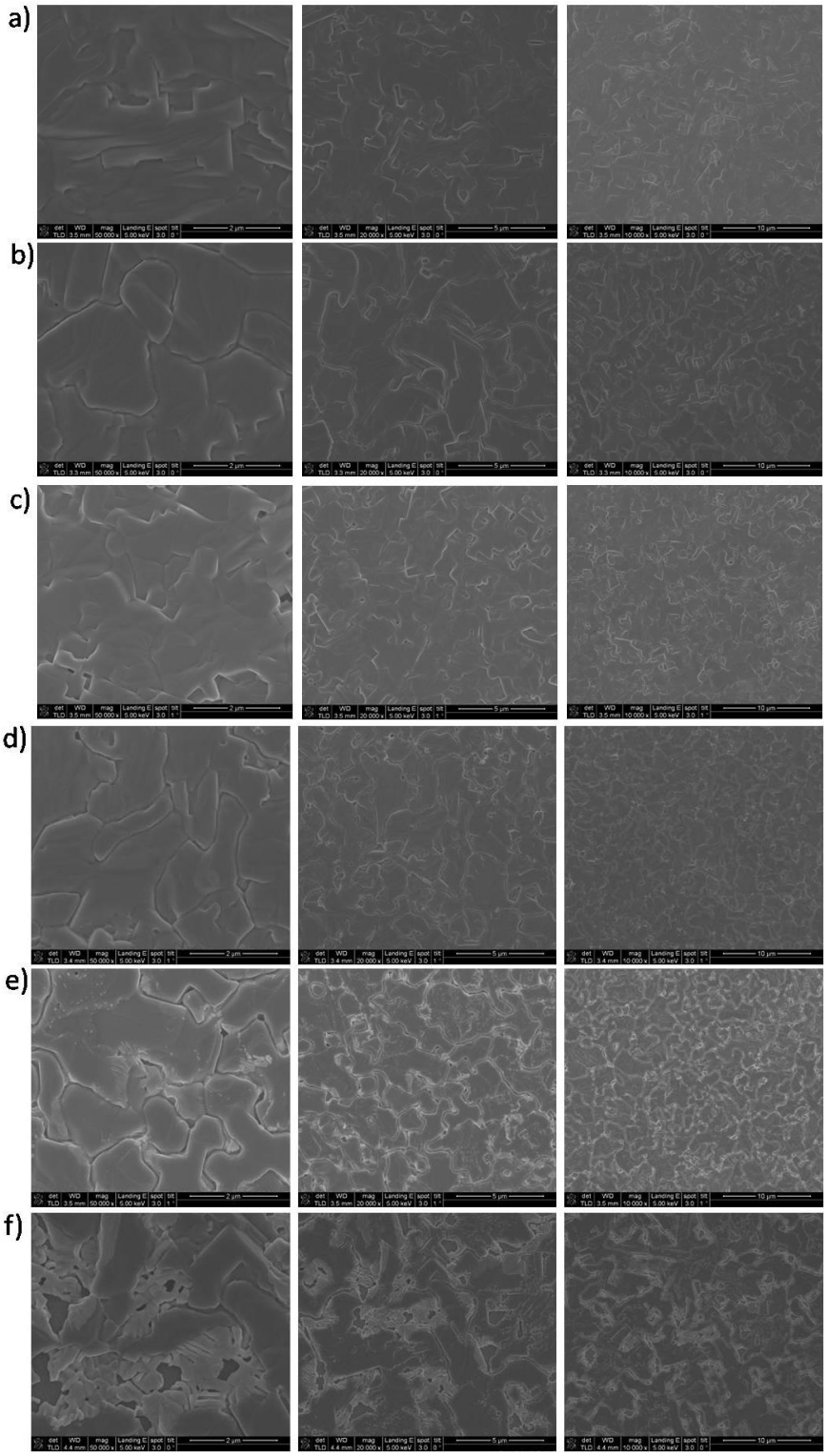

Figure S5.3 Film morphology characterization from SEM images at different annealing times. (a) 40 mins (b) 55 mins (c) 70 mins (d) 90 mins (e) 110 mins and (f) 190 mins at 100 °C.

Chapter 6 Conclusion and Outlook

Next generation materials for solar cell applications provide a promising route to dramatically enhance PV technologies' competitiveness in the energy market by improving both the performance and the cost-effectiveness of the fabrication process. In this thesis, silver nanowire electrodes show remarkable transmission and sheet resistance values, ease of fabrication and incur little damage to the underlying device layers, due to the low processing temperatures and benign chemical solvent. Versatile nanocomposite structures, including nanowire/NPs and nanowire/sol-gel, as demonstrated in this thesis can maintain excellent electrode performance while improving the coating properties, contact formation, chemical stability and film adhesion. The flexibility and stretchability of silver nanowire electrodes also make them suitable for numerous next generation device structures, especially for producing useful wearable electronics.

The greatest issue the silver nanowire electrodes face to date is their susceptibility to degradation due to continued electrical damage. Even though it has been demonstrated that improved stability can be obtained by adding a protecting layer, the electromigration of the Ag atoms under continuous applied electrical field would cause the nanowire to break in practical applications. Future development of nanowire electrodes should be weighted in

this direction in order to ensure their stability and compatibility in device applications.

Thin film solar cells have their own array of advantages and disadvantages which separate them from conventional devices. The wide availability and non-toxicity of raw materials for CZTS fabrication has attracted a substantial amount of research attention, but controlling junction formation and defective surface layers in CZTS system remain challenging. Extrinsic doping might be a possible way to push the limits of intrinsic effects; meanwhile more efforts should be focused in the direction of growing high quality film and developing more effective way to passivate defects.

Hybrid perovskite solar cells show an excellent power conversion efficiency and outstanding material properties but the usage of Pb element is not environmental-friendly and is also harmful to human body. The substitution of Pb element results in deteriorated optical and electrical properties. Moreover, the instability of the hybrid structure due to the organic species is also a challenge in practical applications. The next stages in these low cost and high performance solar cells should center on Pb replacement and molecular design of organic species.

The next handful of years will likely be an important time in the development of CZTS and perovskite solar cell devices, during which it will be determined whether or not the various difficulties associated with CZTS and perovskite materials can be resolved to a sufficient

degree and meet the requirement of solar markets. This will undoubtedly take time, but the understanding and techniques gained along the way will benefit the development of future material systems.

References

1. F. Dross, K. Baert, T. Bearda, J. Deckers, V. Depauw, O. El Daif, I. Gordon, A. Gougam, J. Govaerts, S. Granata, R. Labie, X. Loozen, R. Martini, A. Masolin, B. O'Sullivan, Y. Qiu, J. Vaes, D. Van Gestel, J. Van Hoeymissen, A. Vanleenhove, K. Van Nieuwenhuysen, S. Venkatachalam, M. Meuris, and J. Poortmans, "Crystalline thin-foil silicon solar cells: where crystalline quality meets thin-film processing." Progress in Photovoltaics: Research and Applications, 2012. **20**, pp. 770-784.
2. http://en.wikipedia.org/wiki/Theory_of_solar_cells.
3. K. Ellmer, "Past achievements and future challenges in the development of optically transparent electrodes." Nature Photon, 2012. **6**, pp. 809-817.
4. T.-B. Song and N. Li, "Emerging Transparent Conducting Electrodes for Organic Light Emitting Diodes." Electronics, 2014. **3**, pp. 190-204.
5. J.H. Heo, S.H. Im, J.H. Noh, T.N. Mandal, C.-S. Lim, J.A. Chang, Y.H. Lee, H.-j. Kim, A. Sarkar, K. NazeeruddinMd, M. Gratzel, and S.I. Seok, "Efficient inorganic-organic hybrid heterojunction solar cells containing perovskite compound and polymeric hole conductors." Nature Photonics, 2013. **7**, pp. 486-491.
6. J. Wu, M. Agrawal, H.A. Becerril, Z. Bao, Z. Liu, Y. Chen, and P. Peumans, "Organic light-emitting diodes on solution-processed graphene transparent electrodes. ACS Nano, 2009. **4**, pp. 43-48.
7. L. Hu, D.S. Hecht, and G. Grüner, "Carbon nanotube thin films: fabrication, properties, and applications." Chemical Reviews, 2010. **110**, pp. 5790-5844.
8. S. Bae, H. Kim, Y. Lee, X. Xu, J.-S. Park, Y. Zheng, J. Balakrishnan, T. Lei, H. Ri Kim, Y. I. Song, Y.-J. Kim, K.S. Kim, B. Ozyilmaz, J.-H. Ahn, B.H. Hong, and S. Iijima, "Roll-to-roll production of 30-inch graphene films for transparent electrodes." Nature Nanotechnology, 2010. **5**, pp. 574-578.
9. L. Hu, H. Wu, and Y. Cui, "Metal nanogrids, nanowires, and nanofibers for transparent electrodes." MRS Bulletin, 2011. **36**, pp. 760-765.
10. M.A. Green, K. Emery, Y. Hishikawa, W. Warta, and E.D. Dunlop, "Solar cell efficiency tables (version 45)." Progress in Photovoltaics: Research and Applications, 2015. **23**, pp. 1-9.
11. A. Lafond, L. Choubrac, C. Guillot-Deudon, P. Deniard, and S. Jobic, "Crystal structures of photovoltaic chalcogenides, an intricate puzzle to solve: the cases of CIGSe and CZTS materials." Zeitschrift für anorganische und allgemeine Chemie, 2012. **638**, pp. 2571-2577.

12. H. Zhou, W.-C. Hsu, H.-S. Duan, B. Bob, W. Yang, T.-B. Song, C.-J. Hsu, and Y. Yang, "CZTS nanocrystals: a promising approach for next generation thin film photovoltaics." Energy & Environmental Science, 2013. **6**, pp. 2822-2838.
13. D.B. Mitzi, O. Gunawan, T.K. Todorov, K. Wang, and S. Guha, "The path towards a high-performance solution-processed kesterite solar cell." Solar Energy Materials and Solar Cells, 2011. **95**, pp. 1421-1436.
14. H. Katagiri, K. Jimbo, W.S. Maw, K. Oishi, M. Yamazaki, H. Araki, and A. Takeuchi, "Development of CZTS-based thin film solar cells." Thin Solid Films, 2009. **517**, pp. 2455-2460.
15. K. Wang, B. Shin, K.B. Reuter, T. Todorov, D.B. Mitzi, and S. Guha, "Structural and elemental characterization of high efficiency Cu_2ZnSnS_4 solar cells." Applied Physics Letters, 2011. **98**, pp. 051912.
16. C.-H. Chung, T.-B. Song, B. Bob, R. Zhu, H.-S. Duan, and Y. Yang, "Silver nanowire composite window layers for fully solution-deposited thin-film photovoltaic devices." Advanced Materials, 2012. **24**, pp. 5499-5504.
17. W. Wang, M.T. Winkler, O. Gunawan, T. Gokmen, T.K. Todorov, Y. Zhu, and D.B. Mitzi, "Device characteristics of CZTSSe thin-film solar cells with 12.6% efficiency." Advanced Energy Materials, 2014. **4**, pp. 13014654.
18. J. Kim, H. Hiroi, T.K. Todorov, O. Gunawan, M. Kuwahara, T. Gokmen, D. Nair, M. Hopstaken, B. Shin, Y.S. Lee, W. Wang, H. Sugimoto, and D.B. Mitzi, "High efficiency $Cu_2ZnSn(S,Se)_4$ solar cells by applying a double In_2S_3/CdS emitter." Advanced Materials, 2014. **26**, pp. 7427-7431.
19. L. Craig, H. Charlie, B. Alison, S. Chris, K. Wooseok, and Z. Don, "Final report: sintered CZTS nanoparticle solar cells on metal foil." NREL/SR-5200-56501," 2012. [Online]. Available: http://www.osti.gov/bridge Available 2012.
20. H. Xin, J.K. Katahara, I.L. Braly, and H.W. Hillhouse, "8% efficient $Cu_2ZnSn(S,Se)_4$ solar cells from redox equilibrated simple precursors in DMSO." Advanced Energy Materials, 2014. **4**, pp. 1301823.
21. Y. S. Lee, T. Gershon, O. Gunawan, T.K. Todorov, T. Gokmen, Y. Virgus, and S. Guha, "$Cu_2ZnSnSe_4$ thin-film solar cells by thermal co-evaporation with 11.6% efficiency and improved minority carrier diffusion length." Advanced Energy Materials, 2014. pp. 1401372.
22. Z. Su, K. Sun, Z. Han, H. Cui, F. Liu, Y. Lai, J. Li, X. Hao, Y. Liu, and M.A. Green, "Fabrication of Cu_2ZnSnS_4 solar cells with 5.1% efficiency via thermal decomposition and reaction using a non-toxic sol-gel route." Journal of Materials

Chemistry A, 2014. **2**, pp. 500-509.
23. Z. Ku, Y. Rong, M. Xu, T. Liu, and H. Han, "Full printable processed mesoscopic $CH_3NH_3PbI_3/TiO_2$ heterojunction solar cells with carbon counter electrode." Scientific Report, 2013. **3**, pp. 3132.
24. J. Mats and L. Peter, "Perovskites and thin films—crystallography and chemistry." Journal of Physics: Condensed Matter, 2008. **20**, pp. 264001.
25. D. V. Taylor and D. Damjanovic, "Piezoelectric properties of rhombohedral $Pb(Zr,Ti)O_3$ thin films with (100), (111), and "random" crystallographic orientation." Applied Physics Letters, 2000. **76**, pp. 1615-1617.
26. J. Hejtmánek, Z. Jirák, M. Maryško, C. Martin, A. Maignan, M. Hervieu, and B. Raveau, "Interplay between transport, magnetic, and ordering phenomena in $Sm_{1-x}Ca_XMnO_3$." Physical Review B, 1999. **60**, pp. 14057-14065.
27. D.B. Mitzi, K. Chondroudis, and C.R. Kagan, "Organic-inorganic electronics." IBM Journal of Research and Development, 2001. **45**, pp. 29-45.
28. D.B. Mitzi, "Synthesis, structure, and properties of organic-inorganic perovskites and related materials." Progress in Inorganic Chemistry, 2007. **48**, pp. 1-121.
29. D.B. Mitzi, C.D. Dimitrakopoulos, and L.L. Kosbar, "Structurally tailored organic−inorganic perovskites: optical properties and solution-processed channel materials for thin-film transistors." Chemistry of Materials, 2001. **13**, pp. 3728-3740.
30. D.B. Mitzi, "Templating and structural engineering in organic-inorganic perovskites." Journal of the Chemical Society, Dalton Transactions, 2001. pp. 1-12.
31. H.J. Snaith, "Perovskites: the emergence of a new era for low-cost, high-efficiency solar cells." The Journal of Physical Chemistry Letters, 2013. **4**, pp. 3623-3630.
32. M.A. Green, A. Ho-Baillie, and H.J. Snaith, "The emergence of perovskite solar cells." Nature Photonics, 2014. **8**, pp. 506-514.
33. N.-G. Park, "Organometal perovskite light absorbers toward a 20% efficiency low-cost solid-state mesoscopic solar cell." The Journal of Physical Chemistry Letters, 2013. **4**, pp. 2423-2429.
34. W.-J. Yin, T. Shi, and Y. Yan, "Unique properties of halide perovskites as possible origins of the superior solar cell performance." Advanced Materials, 2014. **26**, pp. 4653-4658.
35. H.J. Snaith and M. Gratzel, "Electron and hole transport through mesoporous TiO_2 infiltrated with spiro-MeOTAD." Advanced Materials, 2007. **19**, pp. 3643-3647.
36. J. Kim, S.-H. Lee, J.H. Lee, and K.-H. Hong, "The role of intrinsic defects in

methylammonium lead iodide perovskite." The Journal of Physical Chemistry Letters, 2014. **5**, pp. 1312-1317.

37. J. Even, L. Pedesseau, and C. Katan. "Theoretical insights into multibandgap hybrid perovskites for photovoltaic applications." Proc. SPIE 9140, Photonics for Solar Energy Systems V, 91400Y. May 15, 2014.
38. M. Liu, M.B. Johnston, and H.J. Snaith, "Efficient planar heterojunction perovskite solar cells by vapour deposition." Nature, 2013. **501**, pp. 395-398.
39. C.C. Stoumpos, C.D. Malliakas, and M.G. Kanatzidis, "Semiconducting tin and lead iodide perovskites with organic cations: phase transitions, high mobilities, and near-infrared photoluminescent properties." Inorganic Chemistry, 2013. **52**, pp. 9019-9038.
40. W.-J. Yin, J.-H. Yang, J. Kang, Y. Yan, and S.-H. Wei, "Halide perovskite materials for solar cells: a theoretical review." Journal of Materials Chemistry A, 2015 **DOI:** 10.1039/C4TA05033A
41. S.D. Stranks, G.E. Eperon, G. Grancini, C. Menelaou, M.J.P. Alcocer, T. Leijtens, L.M. Herz, A. Petrozza, and H.J. Snaith, "Electron-hole diffusion lengths exceeding 1 micrometer in an organometal trihalide perovskite absorber." Science, 2013. **342**, pp. 341-344.
42. J. You, Z. Hong, Y. Yang, Q. Chen, M. Cai, T.-B. Song, C.-C. Chen, S. Lu, Y. Liu, H. Zhou, and Y. Yang, "Low-temperature solution-processed perovskite solar cells with high efficiency and flexibility." ACS Nano, 2014. **8**, pp. 1674-1680.
43. S.A. Kulkarni, T. Baikie, P.P. Boix, N. Yantara, N. Mathews, and S.G. Mhaisalkar, "Band gap tuning of lead halide perovskites using a sequential deposition process." Journal of Materials Chemistry A, 2014. **2**, pp. 9221-9225.
44. S.P. Singh and P. Nagarjuna, "Organometal halide perovskites as useful materials in sensitized solar cells." Dalton Transactions, 2014. **43**, pp. 5247-5251.
45. Z. Xiao, C. Bi, Y. Shao, Q. Dong, Q. Wang, Y. Yuan, C. Wang, Y. Gao, and J. Huang, "Efficient, high yield perovskite photovoltaic devices grown by interdiffusion of solution-processed precursor stacking layers." Energy & Environmental Science, 2014. **7**, pp. 2619-2623.
46. Q. Chen, H. Zhou, Z. Hong, S. Luo, H.-S. Duan, H.-H. Wang, Y. Liu, G. Li, and Y. Yang, "Planar heterojunction perovskite solar cells via vapor assisted solution process." Journal of the American Chemical Society, 2013. **136**, pp. 622-625.
47. J.-H. Im, H.-S. Kim, and N.-G. Park, "Morphology-photovoltaic property correlation in perovskite solar cells: one-step versus two-step deposition of

$CH_3NH_3PbI_3$." APL Materials, 2014. **2**, pp. 081510.

48. S. Pang, H. Hu, J. Zhang, S. Lv, Y. Yu, F. Wei, T. Qin, H. Xu, Z. Liu, and G. Cui, "$NH_2CH{=}NH_2PbI_3$: an Alternative organolead iodide perovskite sensitizer for mesoscopic solar cells." Chemistry of Materials, 2014. **26**, pp. 1485-1491.
49. A. Kojima, K. Teshima, Y. Shirai, and T. Miyasaka, "Organometal halide perovskites as visible-light sensitizers for photovoltaic cells." Journal of the American Chemical Society, 2009. **131**, pp. 6050-6051.
50. J.-H. Im, C.-R. Lee, J.-W. Lee, S.-W. Park, and N.-G. Park, "6.5% efficient perovskite quantum-dot-sensitized solar cell." Nanoscale, 2011. **3**, pp. 4088-4093.
51. H.S. Kim, C.R. Lee, J.H. Im, K.B. Lee, T. Moehl, A. Marchioro, S.J. Moon, R. Humphry-Baker, J.H. Yum, J.E. Moser, M. Gratzel, and N.G. Park, "Lead iodide perovskite sensitized all-solid-state submicron thin film mesoscopic solar cell with efficiency exceeding 9%." Scientific Reports, 2012. **2**, pp. 591.
52. M.M. Lee, J. Teuscher, T. Miyasaka, T.N. Murakami, and H.J. Snaith, "Efficient hybrid solar cells based on meso-superstructured organometal halide perovskites." Science, 2012. **338**, pp. 643-647.
53. J. Burschka, N. Pellet, S.-J. Moon, R. Humphry-Baker, P. Gao, M.K. Nazeeruddin, and M. Gratzel, "Sequential deposition as a route to high-performance perovskite-sensitized solar cells." Nature, 2013. **499**, pp. 316-319.
54. http://www.nrel.gov/ncpv/images/efficiency_chart.jpg.
55. H. Zhou, Q. Chen, G. Li, S. Luo, T.-B. Song, H.-S. Duan, Z. Hong, J. You, Y. Liu, and Y. Yang, "Interface engineering of highly efficient perovskite solar cells." Science, 2014. **345**, pp. 542-546.
56. Z. Wu, Z. Chen, X. Du, J.M. Logan, J. Sippel, M. Nikolou, K. Kamaras, J.R. Reynolds, D.B. Tanner, A.F. Hebard, and A.G. Rinzler, "Transparent, conductive carbon nanotube films." Science, 2004. **305**, pp. 1273-1276.
57. L. Hu, D.S. Hecht, and G. Grüner, "Percolation in transparent and conducting carbon nanotube networks." Nano Letters, 2004. **4**, pp. 2513-2517.
58. I. Khrapach, F. Withers, T.H. Bointon, D.K. Polyushkin, W.L. Barnes, S. Russo, and M.F. Craciun, "Novel highly conductive and transparent graphene-based conductors." Advanced Materials, 2012. **24**, pp. 2844-2849.
59. J.-Y. Lee, S.T. Connor, Y. Cui, and P. Peumans, "Solution-processed metal nanowire mesh transparent electrodes." Nano Letters, 2008. **8**, pp. 689-692.
60. A.R. Rathmell and B.J. Wiley, "The synthesis and coating of long, thin copper nanowires to make flexible, transparent conducting films on plastic substrates."

Advanced Materials, 2011. **23**, pp. 4798-4803.

61. W. Yang, H.-S. Duan, B. Bob, H. Zhou, B. Lei, C.-H. Chung, S.-H. Li, W.W. Hou, and Y. Yang, "Novel solution processing of high-efficiency earth-abundant $Cu_2ZnSn(S,Se)_4$ solar cells." Advanced Materials, 2012. **24**, pp. 6323-6329.
62. T.M. Barnes, M.O. Reese, J.D. Bergeson, B.A. Larsen, J.L. Blackburn, M.C. Beard, J. Bult, and J. van de Lagemaat, "Comparing the fundamental physics and device performance of transparent, conductive nanostructured networks with conventional transparent conducting oxides." Advanced Energy Materials, 2012. **2**, pp. 353-360.
63. D.S. Hecht, L. Hu, and G. Irvin, "Emerging transparent electrodes based on thin films of carbon nanotubes, graphene, and metallic nanostructures." Advanced Materials, 2011. **23**, pp. 1482-1513.
64. W. Gaynor, J.-Y. Lee, and P. Peumans, "Fully solution-processed inverted polymer solar cells with laminated nanowire electrodes." ACS Nano, 2009. **4**, pp. 30-34.
65. T. Tokuno, M. Nogi, M. Karakawa, J. Jiu, T. Nge, Y. Aso, and K. Suganuma, "Fabrication of silver nanowire transparent electrodes at room temperature." Nano Research, 2011. **4**, pp. 1215-1222.
66. L. Hu, H.S. Kim, J.-Y. Lee, P. Peumans, and Y. Cui, "Scalable coating and properties of transparent, flexible, silver nanowire electrodes." ACS Nano, 2010. **4**, pp. 2955-2963.
67. A. Madaria, A. Kumar, F. Ishikawa, and C. Zhou, "Uniform, highly conductive, and patterned transparent films of a percolating silver nanowire network on rigid and flexible substrates using a dry transfer technique." Nano Research, 2010. **3**, pp. 564-573.
68. C.-H. Chung, T.-B. Song, B. Bob, R. Zhu, and Y. Yang, "Solution-processed flexible transparent conductors composed of silver nanowire networks embedded in indium tin oxide nanoparticle matrices." Nano Research, 2012. **5**, pp. 805-814.
69. R. Zhu, C.-H. Chung, K.C. Cha, W. Yang, Y.B. Zheng, H. Zhou, T.-B. Song, C.-C. Chen, P.S. Weiss, G. Li, and Y. Yang, "Fused silver nanowires with metal oxide nanoparticles and organic polymers for highly transparent conductors." ACS Nano, 2011. **5**, pp. 9877-9882.
70. E.C. Garnett, W. Cai, J.J. Cha, F. Mahmood, S.T. Connor, M. Greyson Christoforo, Y. Cui, M.D. McGehee, and M.L. Brongersma, "Self-limited plasmonic welding of silver nanowire junctions." Nature Materials, 2012. **11**, pp. 241-249.
71. H. Tohmyoh and S. Fukui, "Self-completed Joule heat welding of ultrathin Pt wires." Physical Review B, 2009. **80**, pp. 155403.

72. C. Jin, K. Suenaga, and S. Iijima, "Plumbing carbon nanotubes.: Nature Nanotechnology, 2008. **3**, pp. 17-21.
73. K.N. Tu, "Recent advances on electromigration in very-large-scale-integration of interconnects." Journal of Applied Physics, 2003. **94**, pp. 5451-5473.
74. D. Wakuda, K. Keun-Soo, and K. Suganuma, "Room-temperature sintering process of Ag nanoparticle paste." Components and Packaging Technologies, IEEE Transactions, 2009. **32**, pp. 627-632.
75. M.L. Allen, M. Aronniemi, T. Mattila, A. Alastalo, K. Ojanperä, M. Suhonen, and H. Seppä, "Electrical sintering of nanoparticle structures." Nanotechnology, 2008. **19**, pp. 175201.
76. A.T. Alastalo, H. Seppä, J.H. Leppäniemi, M.J. Aronniemi, M.L. Allen, and T. Mattila, "Modelling of nanoparticle sintering under electrical boundary conditions." Journal of Physics D: Applied Physics, 2010. **43**, pp. 485501.
77. S. Iwama and K. Hayakawa, "Sintering of ultrafine metal powders. II. neck growth stage of Au, Ag, Al and Cu." Japanese Journal of Applied Physics, 1981. **20**, pp. 335.
78. D.E. Sanders and A.E. DePristo, "Predicted diffusion rates on fcc (001) metal surfaces for adsorbate/substrate combinations of Ni, Cu, Rh, Pd, Ag, Pt, Au." Surface Science, 1992. **260**, pp. 116-128.
79. S.M. Bergin, Y.-H. Chen, A.R. Rathmell, P. Charbonneau, Z.-Y. Li, and B.J. Wiley, "The effect of nanowire length and diameter on the properties of transparent, conducting nanowire films." Nanoscale, 2012. **4**, pp. 1996-2004.
80. Z. Yu, L. Li, Q. Zhang, W. Hu, and Q. Pei, "Silver nanowire-polymer composite electrodes for efficient polymer solar cells." Advanced Materials, 2011. **23**, pp. 4453-4457.
81. S. Sorel, P.E. Lyons, S. De, J.C. Dickerson, and J.N. Coleman, "The dependence of the optoelectrical properties of silver nanowire networks on nanowire length and diameter." Nanotechnology, 2012. **23**, pp. 185201.
82. J.L. Elechiguerra, L. Larios-Lopez, C. Liu, D. Garcia-Gutierrez, A. Camacho-Bragado, and M.J. Yacaman, "Corrosion at the nanoscale: the case of silver nanowires and nanoparticles." Chemistry of Materials, 2005. **17**, pp. 6042-6052.
83. S. Karim, M.E. Toimil-Molares, W. Ensinger, A.G. Balogh, T.W. Cornelius, E.U. Khan, and R. Neumann, "Influence of crystallinity on the Rayleigh instability of gold nanowires." Journal of Physics D: Applied Physics, 2007. **40**, pp. 3767.
84. T.-B. Song, Y. Chen, C.-H. Chung, Y. Yang, B. Bob, H.-S. Duan, G. Li, K.-N. Tu,

and Y. Huang, "Nanoscale joule heating and electromigration enhanced ripening of silver nanowire contacts." ACS Nano, 2014. **8**, pp. 2804-2811.

85. P.-C. Hsu, H. Wu, T.J. Carney, M.T. McDowell, Y. Yang, E.C. Garnett, M. Li, L. Hu, and Y. Cui, "Passivation coating on electrospun copper nanofibers for stable transparent electrodes." ACS Nano, 2012. **6**, pp. 5150-5156.
86. P. Ramasamy, D.-M. Seo, S.-H. Kim, and J. Kim, "Effects of TiO_2 shells on optical and thermal properties of silver nanowires." Journal of Materials Chemistry, 2012. **22**, pp. 11651-11657.
87. K. Zilberberg, F. Gasse, R. Pagui, A. Polywka, A. Behrendt, S. Trost, R. Heiderhoff, P. Görrn, and T. Riedl, "Highly robust indium-free transparent conductive electrodes based on composites of silver nanowires and conductive metal oxides." Advanced Functional Materials, 2014. **24**, pp. 1671-1678.
88. M. Langlet, M. Burgos, C. Coutier, C. Jimenez, C. Morant, and M. Manso, "Low temperature preparation of high refractive index and mechanically resistant sol-gel TiO_2 films for multilayer antireflective coating applications." Journal of Sol-Gel Science and Technology, 2001. **22**, pp. 139-150.
89. E. Szalkowska, J. Gluszek, J. Masalski, and W. Tylus, "Structure and protective properties of TiO_2 coatings obtained using the sol-gel technique." Journal of Materials Science Letters, 2001. **20**, pp. 495-497.
90. N. Lima, P., M. Atik, L. Avaca, and M. Aegerter, "Sol-gel coatings for chemical protection of stainless steel." Journal of Sol-Gel Science and Technology, 1994. **2**, pp. 529-534.
91. S. De, T.M. Higgins, P.E. Lyons, E.M. Doherty, P.N. Nirmalraj, W.J. Blau, J.J. Boland, and J.N. Coleman, "Silver nanowire networks as flexible, transparent, conducting films: extremely high DC to optical conductivity ratios." ACS Nano, 2009. **3**, pp. 1767-1774.
92. A.R. Madaria, A. Kumar, and C. Zhou," Large scale, highly conductive and patterned transparent films of silver nanowires on arbitrary substrates and their application in touch screens." Nanotechnology, 2011. **22**, pp. 245201.
93. D.-S. Leem, A. Edwards, M. Faist, J. Nelson, D.D.C. Bradley, and J.C. de Mello, "Efficient organic solar cells with solution-processed silver nanowire electrodes." Advanced Materials, 2011. **23**, pp. 4371-4375.
94. N. La, L., L. Salamandra, A. Zampetti, F. Brunetti, T.M. Brown, A. Di Carlo, and A. Reale, "Airbrush spray coating of amorphous titanium dioxide for inverted polymer solar cells." International Journal of Photoenergy, 2012. **2012**. pp. 5.

95. L.L. Hench and J.K. West, "The sol-gel process." Chemical Reviews, 1990. **90**, pp. 33-72.
96. A. Kim, Y. Won, K. Woo, S. Jeong, and J. Moon, "All-solution-processed indium-free transparent composite electrodes based on Ag nanowire and metal oxide for thin-film solar cells." Advanced Functional Materials, 2014. **24**, pp. 2462-2471.
97. F.S.F. Morgenstern, D. Kabra, S. Massip, T.J.K. Brenner, P.E. Lyons, J.N. Coleman, and R.H. Friend, "Ag-nanowire films coated with ZnO nanoparticles as a transparent electrode for solar cells." Applied Physics Letters, 2011. **99**, pp. 183307.
98. G.-H. Shen and F.C.-N. Hong, "Ultraviolet photosensors fabricated with Ag nanowires coated with ZnO nanoparticles." Thin Solid Films, 2014. **570**, pp. 363-370.
99. S. Karim, M.E. Toimil-Molares, A.G. Balogh, W. Ensinger, T.W. Cornelius, E.U. Khan, and R. Neumann, "Morphological evolution of Au nanowires controlled by Rayleigh instability." Nanotechnology, 2006. **17**, pp. 5954.
100. C. Peng, Z. Jia, H. Neilson, T. Li, and J. Lou, "In situ electro-mechanical experiments and mechanics modeling of fracture in indium tin oxide-based multilayer electrodes." Advanced Energy Materials, 2012. **15**, pp. 250-256.
101. R. Hattori and J. Kanicki, "Contact resistance in schottky contact gated-four-probe a-Si thin-film transistor." Japanese Journal of Applied Physics, 2003. **42**, pp. L907.
102. M. Nakata, K. Takechi, T. Eguchi, E. Tokumitsu, H. Yamaguchi, and S. Kaneko, "Effects of thermal annealing on ZnO thin-film transistor characteristics and the application of excimer laser annealing in plastic-based ZnO thin-film transistors." Japanese Journal of Applied Physics, 2009. **48**, pp. 081608.
103. W.M. Hlaing Oo, J.L. Johnson, A. Bhatia, E.A. Lund, M.M. Nowell, and M.A. Scarpulla, "Grain size and texture of Cu_2ZnSnS_4 thin films synthesized by cosputtering binary sulfides and annealing: effects of processing conditions and sodium." Journal of Electronic Materials, 2011. **40**, pp. 2214-2221.
104. M. Johnson, S.V. Baryshev, E. Thimsen, M. Manno, X. Zhang, I.V. Veryovkin, C. Leighton, and E.S. Aydil, "Alkali-metal-enhanced grain growth in Cu2ZnSnS4 thin films." Energy & Environmental Science, 2014. **7**, pp. 1931-1938.
105. H. Zhou, T.-B. Song, W.-C. Hsu, S. Luo, S. Ye, H.-S. Duan, C.-J. Hsu, W. Yang, and Y. Yang, "Rational defect passivation of $Cu_2ZnSn(S,Se)_4$ photovoltaics with solution-processed Cu_2ZnSnS_4:Na nanocrystals." Journal of the American Chemical Society, 2013. **135**, pp. 15998-16001.
106. N. Tokio, I. Daisuke, O. Hiroki, and K. Akio, "Effects of sodium on $Cu(In,Ga)Se_2$-

based thin films and solar cells." Japanese Journal of Applied Physics, 1997. **36**, pp. 732.

107. R. Kaigawa, Y. Satake, K. Ban, S. Merdes, and R. Klenk, "Effects of Na on the properties of Cu(In,Ga)S_2 solar cells." Thin Solid Films, 2011. **519**, pp. 5535-5538.
108. T. Gershon, B. Shin, N. Bojarczuk, M. Hopstaken, D.B. Mitzi, and S. Guha, "The role of sodium as a surfactant and suppressor of non-radiative recombination at internal surfaces in Cu_2ZnSnS_4." Advanced Energy Materials, 2014. pp. 1400849.
109. J.V. Li, D. Kuciauskas, M.R. Young, and I.L. Repins, "Effects of sodium incorporation in co-evaporated $Cu_2ZnSnSe_4$ thin-film solar cells." Applied Physics Letters, 2013. **102**, pp. 163905.
110. G. Kim, J. Kim, W. Jo, D.-H. Son, D.-H. Kim, and J.-K. Kang, "Nanoscale investigation of surface potential distribution of $Cu_2ZnSn(S,Se)_4$ thin films grown with additional NaF layers." Nano Convergence, 2014. **1**, p. 27.
111. K. Granath, M. Bodegård, and L. Stolt, "The effect of NaF on Cu(In,Ga)Se_2 thin film solar cells." Solar Energy Materials and Solar Cells, 2000. **60**, pp. 279-293.
112. J.-H. Yoon, T.-Y. Seong, and J.-H. Jeong, "Effect of a Mo back contact on Na diffusion in CIGS thin film solar cells." Progress in Photovoltaics: Research and Applications, 2013. **21**, pp. 58-63.
113. A. Romeo, M. Terheggen, D. Abou-Ras, D.L. Bätzner, F.J. Haug, M. Kälin, D. Rudmann, and A.N. Tiwari, "Development of thin-film Cu(In,Ga)Se_2 and CdTe solar cells." Progress in Photovoltaics: Research and Applications, 2004. **12**, pp. 93-111.
114. A. Chirilă, S. Buecheler, F. Pianezzi, P. Bloesch, C. Gretener, A.R. Uhl, C. Fella, L. Kranz, J. Perrenoud, S. Seyrling, R. Verma, S. Nishiwaki, Y.E. Romanyuk, G. Bilger, and A.N. Tiwari, "Highly efficient Cu(In,Ga)Se_2 solar cells grown on flexible polymer films." Nature Materials, 2011. **10**, pp. 857-861.
115. W.-C. Hsu, H. Zhou, S. Luo, T.-B. Song, Y.-T. Hsieh, H.-S. Duan, S. Ye, W. Yang, C.-J. Hsu, C. Jiang, B. Bob, and Y. Yang, "Spatial element distribution control in a fully solution-processed nanocrystals-based 8.6% $Cu_2ZnSn(S,Se)_4$ device." ACS Nano, 2014. **8**, pp. 9164-9172.
116. J.V. Li, D. Kuciauskas, M.R. Young, and I.L. Repins, "Effects of sodium incorporation in co-evaporated $Cu_2ZnSnSe_4$ thin-film solar cells." Applied Physics Letters, 2013. **102**, pp. 163905.
117. T. Prabhakar and N. Jampana, "Effect of sodium diffusion on the structural and electrical properties of Cu_2ZnSnS_4 thin films." Solar Energy Materials and Solar

Cells, 2011. **95**, pp. 1001-1004.

118. Q. Guo, G.M. Ford, R. Agrawal and H.W. Hillhouse, "Ink formulation and low-temperature incorporation of sodium to yield 12% efficient Cu(In,Ga)($S,Se)_2$ solar cells from sulfide nanocrystal inks" Progress in Photovoltaics: Research and Applications, 2013. **21**, pp. 64-71
119. Q. Guo, G.M. Ford, W.-C. Yang, B.C. Walker, E.A. Stach, H.W. Hillhouse, and R. Agrawal, "Fabrication of 7.2% efficient CZTSSe solar cells using CZTS nanocrystals." Journal of the American Chemical Society, 2010. **132**, pp. 17384-17386.
120. Y. Cao, M.S. Denny, J.V. Caspar, W.E. Farneth, Q. Guo, A.S. Ionkin, L.K. Johnson, M. Lu, I. Malajovich, D. Radu, H.D. Rosenfeld, K.R. Choudhury, and W. Wu, "High-efficiency solution-processed $Cu_2ZnSn(S,Se)_4$ thin-film solar cells prepared from binary and ternary nanoparticles." Journal of the American Chemical Society, 2012. **134**, pp. 15644-15647.
121. M. Edoff, P.M.P. Salomé, A. Hultqvist, and V. Fjällström, "Analysis of NaF precursor layers during the different stages of the Cu(In,Ga)Se_2 coevaporation process." MRS Online Proceedings Library, 2013. **1538**, pp. 9-14.
122. O. Gunawan, T.K. Todorov, and D.B. Mitzi, "Loss mechanisms in hydrazine-processed $Cu_2ZnSn(Se,S)_4$ solar cells." Applied Physics Letters, 2010. **97**, pp. 233506.
123. H.-S. Duan, W. Yang, B. Bob, C.-J. Hsu, B. Lei, and Y. Yang, "The role of sulfur in solution-processed $Cu_2ZnSn(S,Se)_4$ and its effect on defect properties." Advanced Functional Materials, 2013. **23**, pp. 1466-1471.
124. A. Rockett, "The effect of Na in polycrystalline and epitaxial single-crystal $CuIn_{1-X}Ga_XSe_2$." Thin Solid Films, 2005. **480–481**, pp. 2-7.
125. A.G. Aberle, "Thin-film solar cells." Thin Solid Films, 2009. **517**, pp. 4706-4710.
126. T.T. Chow, "A review on photovoltaic/thermal hybrid solar technology." Applied Energy, 2010. **87**, pp. 365-379.
127. M. Gloeckler, I. Sankin, and Z. Zhao, "CdTe solar cells at the threshold to 20% efficiency." Photovoltaics, IEEE Journal of, 2013. **3**, pp. 1389-1393.
128. A. Polizzotti, I.L. Repins, R. Noufi, S.-H. Wei, and D.B. Mitzi, "The state and future prospects of kesterite photovoltaics." Energy & Environmental Science, 2013. **6**, pp. 3171-3182.
129. J. Peng, L. Lu, and H. Yang, "Review on life cycle assessment of energy payback and greenhouse gas emission of solar photovoltaic systems." Renewable and

Sustainable Energy Reviews, 2013. **19**, pp. 255-274.

130. N.J. Jeon, J.H. Noh, Y.C. Kim, W.S. Yang, S. Ryu, and S.I. Seok, "Solvent engineering for high-performance inorganic–organic hybrid perovskite solar cells." Nature Materials, 2014. **13**, pp. 897-903.
131. P. Docampo, J.M. Ball, M. Darwich, G.E. Eperon, and H.J. Snaith, "Efficient organometal trihalide perovskite planar-heterojunction solar cells on flexible polymer substrates." Nature Communication, 2013. **4**, pp. 2761.
132. J. Even, L. Pedesseau, and C. Katan, "Analysis of multi-valley and multi-bandgap absorption and enhancement of free carriers related to exciton screening in hybrid perovskites." The Journal of Physical Chemistry C, 2014. **118**, pp. 11566-11572.
133. L. Li, J.-H.Y., H.-R. Liu, H. J. Xiang, X. G. Gong, "First-principles study on the electronic and optical properties of cubic ABX_3 halide perovskites." Physics Letters A, 2014. **378**, pp. 290-293.
134. G. Xing, N. Mathews, S. Sun, S.S. Lim, Y.M. Lam, M. Grätzel, S. Mhaisalkar, and T.C. Sum, "Long-range balanced electron- and hole-transport lengths in organic-inorganic $CH_3NH_3PbI_3$." Science, 2013. **342**, pp. 344-347.
135. J.H. Noh, S.H. Im, J.H. Heo, T.N. Mandal, and S.I. Seok, "Chemical management for colorful, efficient, and stable inorganic–organic hybrid nanostructured solar cells." Nano Letters, 2013. **13**, pp. 1764-1769.
136. G.E. Eperon, S.D. Stranks, C. Menelaou, M.B. Johnston, L. Herz, and H. Snaith, "Formamidinium lead trihalide: a broadly tunable perovskite for efficient planar heterojunction solar cells." Energy & Environmental Science, 2014. **7**, pp. 982-988.
137. A. Dualeh, N. Tétreault, T. Moehl, P. Gao, M.K. Nazeeruddin, and M. Grätzel, "Effect of annealing temperature on film morphology of organic–inorganic hybrid pervoskite solid-state solar cells." Advanced Functional Materials, 2014. **24**, pp. 3250-3258.
138. G.E. Eperon, V.M. Burlakov, P. Docampo, A. Goriely, and H.J. Snaith, "Morphological control for high performance, solution-processed planar heterojunction perovskite solar cells." Advanced Functional Materials, 2013. **24**, pp. 151-157.
139. Q. Wang, Q. Dong, Z. Xiao, Y. Yuan, and J. Huang, "Large fill-factor bilayer iodine perovskite solar cells fabricated by low-temperature solution-process." Energy & Environmental Science, 2014. **7**, pp. 2359-2365.
140. B.-W. Park,, B. Philippe, T. Gustafsson, K. Sveinbjörnsson, A. Hagfeldt, E.M.J. Johansson, and G. Boschloo, "Enhanced crystallinity in organic–inorganic lead

halide perovskites on mesoporous TiO_2 via disorder–order phase transition." Chemistry of Materials, 2014. **26**, pp. 4466-4471.

141. P.-W. Liang, C.-Y. Liao, C.-C. Chueh, F. Zuo, S.T. Williams, X.-K. Xin, J. Lin, and A.K.Y. Jen, "Additive enhanced crystallization of solution-processed perovskite for highly efficient planar-heterojunction solar cells." Advanced Materials, 2014. **26**, pp. 3748-3754.
142. D. Schmid, M. Ruckh, F. Grunwald, and H.W. Schock, "Chalcopyrite/defect chalcopyrite heterojunctions on the basis of $CuInSe_2$." Journal of Applied Physics, 1993. **73**, pp. 2902-2909.
143. M. Bär, S. Nishiwaki, L. Weinhardt, S. Pookpanratana, O. Fuchs, M. Blum, W. Yang, J.D. Denlinger, W.N. Shafarman, and C. Heske, "Depth-resolved band gap in Cu(In,Ga)(S,Se)2 thin films." Applied Physics Letters, 2008. **93**, pp. 244103.
144. H. Peng, C. Xie, D.T. Schoen, K. McIlwrath, X.F. Zhang, and Y. Cui, "Ordered vacancy compounds and nanotube formation in $CuInSe_2$−CdS core−shell nanowires." Nano Letters, 2007. **7**, pp. 3734-3738.
145. A. Fairbrother, E. García-Hemme, V. Izquierdo-Roca, X. Fontané, F.A. Pulgarín-Agudelo, O. Vigil-Galán, A. Pérez-Rodríguez, and E. Saucedo, "Development of a selective chemical etch to improve the conversion efficiency of Zn-rich Cu_2ZnSnS_4 solar cells." Journal of the American Chemical Society, 2012. **134**, pp. 8018-8021.
146. K. Wojciechowski, M. Saliba, T. Leijtens, A. Abate, and H. Snaith, "Sub-150 °C processed meso-superstructured perovskite solar cells with enhanced efficiency." Energy & Environmental Science, 2014. **7**, pp. 1142-1147.
147. A. Dualeh, P. Gao, S.I. Seok, M.K. Nazeeruddin, and M. Grätzel, "Thermal behavior of methylammonium lead-trihalide perovskite photovoltaic light harvesters." Chemistry of Materials, 2014. **26**, pp. 6160-6164.
148. T. Supasai, N. Rujisamphan, K. Ullrich, A. Chemseddine, and T. Dittrich, "Formation of a passivating $CH_3NH_3PbI_3/PbI_2$ interface during moderate heating of $CH_3NH_3PbI_3$ layers." Applied Physics Letters, 2013. **103**, pp. 183906.
149. H. Yu, F. Wang, F. Xie, W. Li, J. Chen, and N. Zhao, "The role of chlorine in the formation process of "$CH_3NH_3PbI_{3-x}Cl_x$" perovskite." Advanced Functional Materials, 2014. **24**, pp. 7102-7108.
150. Q. Chen, H. Zhou, T.-B. Song, S. Luo, Z. Hong, H.-S. Duan, L. Dou, Y. Liu, and Y. Yang, "Controllable self-induced passivation of hybrid lead iodide perovskites toward high performance solar cells." Nano Letters, 2014. **14**, pp. 4158-4163.
151 T.-B. Song, Q. Chen, H. Zhou, S. Luo, Y. M. Yang, J. You, Y. Yang, "Unraveling

film transformation and device performance of planar perovksite solar cells" Nano Energy, 2015 DOI: 10.1016/j.nanoen.2015.01.025.